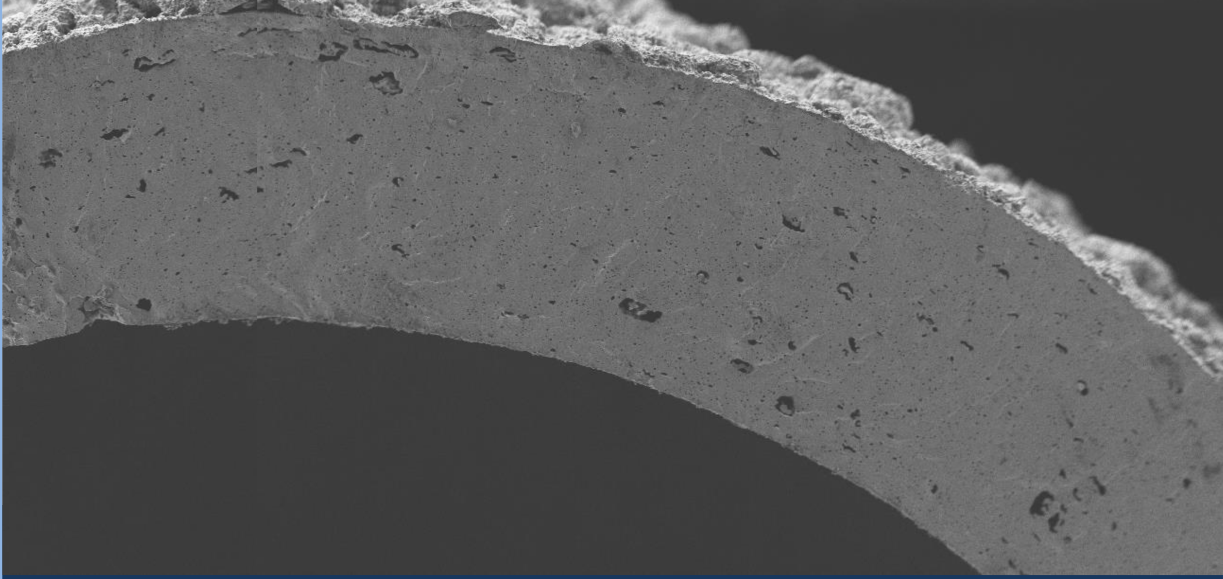

Development of high temperature MIEC catalytic reactors for energy conversion and storage applications

Thesis submitted by

Marwan Laqdiem Marín

To apply for the Degree of Doctor

Supervisor:

Prof. José Manuel Serra Alfaro

Dr. Julio Garcia Fayos

Valencia, March 2024

UNIVERSITAT POLITÈCNICA DE VALÈNCIA

INSTITUTO DE TECNOLOGÍA QUÍMICA

CSIC
Consejo Superior de Investigaciones Científicas

Acknowledgements

I would like to start by thanking all my colleagues in the lab, colleagues who are now family to me, who have seen me grow during this thesis. Many things have happened during this period, we have laughed, we have cried but above all you have helped me to grow, as a future researcher and as a person. Although the latter is still a little more difficult to see. Sonia Escolastico, Maria Balaguer and Maria Fabuel are by far the ones who have suffered the most, so I want to thank you especially for all the effort and all the help you have given me during these years. You welcomed me with great affection and I hope one day to be able to repay you for all that you have done for me. I can't forget David, Fidel, Alfonso, Alvaro, Maria V., Nora, Laura A., Laura N., Mateuz, Sonia R., Jorge, who have also put up with my theories, hints and crazy ideas (that never came to anything or yes…) always with a smile and willing to help. But this does not end here, during my PhD more people have been joining this family so disparate and yet so great. Thanks from the bottom of my heart to all my colleagues of debates and beers: Andres, Imanol, Aitor, Elena B, Luis, Aida, Sara, Candela, Anais, Andrea, Ana, Blanca, Cristian, Silvia, Elena C. and all the rest.

I would also like to thank all the people at ITQ who in one way or another have made this thesis a little lighter. Special thanks to my master classmate Agus and to the whole team of beers in the campus. I can't forget to thank the microscopy service of the UPV who have helped me whenever I needed it. I can't forget to thank also the ITQ workshop service and administration who have always been willing to help me in any problem I had.

Mom, Dad and Omar without you none of this would have happened. Thanks to you are who I am and I have finished my PhD. Thank you for having contributed in these years of thesis (the previous ones too but this is getting long). Of course to all my friends (also as family) who have put up with my comings and goings, celebrating my successes and failures, all these years of PhD, especially to: *Halmitjanes*, the Denia scout group *and gaticos y moneques*. I have to make a special mention to certain friends who have always been there when needed and especially during the course of this thesis (listening to my theories,

advances, arguments, etc.). Thanks Nahuel, Kiko, Just, Vicent, Pascu, Adri, Milan, Dani and Anna.

Also I would like to thank to the UPV the financial support for this thesis. Also the projects I was involved: Icareplast (European project), Isrulab, Almagreen and much more.

Finally I would like to thank the two pillars of this thesis: José M. Serra and Julio Garcia-Fayos. José, thank you very much for giving me the opportunity to work in your group. I will always be grateful for everything you have done for me. You have allowed me to be myself without having to fit into a typical work roll. You are like my father in science and I hope one day I can live up to you. Julio, you have been a like a big brother to me. You have always supported me and let me create, help, prove my point of view no matter how absurd it seemed. I am very proud that you have been my co-director and I can't imagine anyone better than you.

Amatxo xapelduna, ¡zugaiti!

Monty Python and the Holy Grail

***BEDEVERE**: Quiet, quiet. Quiet! There are ways of telling whether she is a witch.*

***CROWD**: Are there? What are they?*

***BEDEVERE**: Tell me, what do you do with witches?*

***CROWD**: Buuuurn them!*

***BEDEVERE:** And what do you burn apart from witches?*

***CROWD:** More witches!... Wood!*

***BEDEVERE:** So, why do witches burn?*

***CROWD:** B'cause they're made of wood…?*

***BEDEVERE:** Good!... So, how do we tell whether she is made of wood?*

***CROWD:** Build a bridge ou' of 'er!*

***BEDEVERE:** Aah, but can you not also build bridges out of stone?... Does wood sink in water?*

***CROWD:** No, no. It floats! It floats!*

***BEDEVERE:** What also floats in water?*

***CROWD**: Bread!... Apples!... Very small rocks.*

***ARTHUR**: A duck!*

***CROWD:** Oooh.*

***BEDEVERE:** Exactly! ... So?*

***CROWD**: If... she... weighs the same as a duck...she's made of wood.*

***BEDEVERE**: Who are you who are so wise in the ways of science?*

***ARTHUR:** I am Arthur, King of the Britons.*

Development of high temperature MIEC catalytic reactors for energy conversion and storage applications

0. Preamble

1. Introduction

2. Methodology

3. Optimization of dual-phase electrodes for high-temperature membrane reactors

4. Novel dual-phase MIEC membranes for catalytic membranes reactors

5. Lowering operation temperature in oxygen transport membrane reactors (OTMR) by membrane electrification

6. Effect of conductivity in chemical looping methane reforming using doped ceria as an oxygen-carrier catalyst

0.

PREAMBLE

0. Preamble

Summary

This thesis is focused on the combination of different technologies to improve emerging technologies for carbon capture and storage (CSS) and the revalorization of the CO_2 captured. The leading technology studied in this thesis was oxygen transport membranes (OTMs) that could produce pure oxygen more flexibly than the current oxygen production technologies like cryogenic air distillation. The production of pure oxygen is crucial for developing oxycombustion reactors that could be more efficient for carbon capture than traditional combustion reactors. The OTMs studies were divided into two main topics: dual-phase membranes with stable operation in CO_2 and BSCF-based membranes ($Ba_{1-x}Sr_xCo_{1-y}Fe_yO_{3-\delta}$). For the revalorization of the captured CO_2, the chemical looping technology based on a cerium oxide catalyst was studied, which takes advantage of the redox properties of the catalyst at different pO_2 and high temperatures (between 700-1400 °C).

In general, the principal limiting steps for OTMs were the bulk oxygen transfer and the surface exchange reactions. In this matter, the improvement in the behaviour of the catalytic layer could achieve better oxygen permeation. The first study for dual-phase membranes was focused on the role of the different dual-phase ratios in the behaviour as a catalytic layer in OTMs. For this study, NFO-CTO ($NiFe_2O_4/Ce_{0.8}Tb_{0.2}O_{2-\delta}$) was selected as dual-phase material. This material was previously studied and showed high stability under CO_2 environments but with poor oxygen flux compared with other dual-phase materials. The study considered for the present Thesis showed interesting results, and it was combined with electrochemical impedance spectroscopy (EIS) measurements, commonly used to study electrodes for solid oxide fuel cells (SOFC) and solid oxide electrolysis cells (SOEC). The second study in dual-phase materials for OTMs focused on the

increase in oxygen permeation for spinel-fluorite-based materials. In this matter, the bulk oxygen transports are controlled, apart from the temperature and the pO_2 gradient, by the ambipolar conductivity, where the electrical and the ionic conductivities are involved. So, the NFO phase was changed for the CMO phase (Co_2MnO_4), which has higher total conductivity than the NFO. The resultant dual-phase material (CMO-CTO) performed better than the predecessor NFO-CTO material.

As mentioned previously, the other study on OTMs focused on BSCF-based membranes. In this study, the BSCF capillary membrane was electrified in order to increase the membrane temperature via the Joule effect and, as a consequence, an increase in the oxygen permeation. In addition, this effect under oxidative dehydrogenation of ethane was studied, obtaining an essential improvement for electrified BSCF membranes compared with non-electrified BSCF membranes. These studies have opened new gates to operate these membranes at lower reactor temperatures.

Finally, the last study was focused on CO_2 upcycling via chemical looping methane reforming. Chemical looping is based on the redox properties of the catalyst in two principal steps, reduction and oxidation of the catalyst. The catalyst reduction is performed with temperature in inert conditions or with reducing streams like methane. We were focused on the reduction via methane that works at lower temperatures than inert streams and could provide syngas streams (a mixture of CO and H_2) that improve global efficiency. The revalorization of the CO_2 was performed in the other step, the oxidation part of the cycle. The oxidation of those catalysts could be formed with H_2O and/or CO_2 streams at high temperatures of 700-1000 °C. Our study was focused on 10% doped cerium oxide with trivalent elements. In this study, the CO_2 splitting on the oxidation step was correlated with the crystal structure parameters and the total conductivity of these materials.

Resumen

Esta tesis está centrada en la combinación de diferentes tecnologías para mejorar las tecnologías emergentes de captura y almacenamiento de carbono (CSS) y la revalorización del CO_2 capturado. La principal tecnología estudiada en esta tesis fueron las membranas de transporte de oxígeno (OTMs), las cuales pueden producir oxígeno puro de forma más flexible que las actuales tecnologías de producción de oxígeno, como la destilación criogénica de aire. La producción de oxígeno puro es crucial para desarrollar reactores de oxicombustión que podrían ser más eficientes para la captura de CO_2 que los reactores actuales de combustión con aire. Los estudios sobre OTMs se dividieron en dos temas principales: membranas de bifásicas estables en CO_2 y membranas basadas en BSCF ($Ba_{1-x}Sr_xCo_{1-y}Fe_yO_{3-\delta}$). Por otro lado, para la revalorización del CO_2 capturado, se estudió la tecnología de looping químico basada en catalizador de óxido de cerio, que aprovecha las propiedades redox del catalizador a diferentes pO_2 y altas temperaturas (entre 700-1400 °C).

En general, las principales etapas limitantes en OTMs son la transferencia de oxígeno a través de la membrana y las reacciones superficiales. Por eso, una mejora en las propiedades de la capa catalítica podría mejorar la permeación total de oxígeno. El primer estudio sobre membranas bifásicas se centró el estudio de capas catalíticas con distintas proporciones de ambas fases. Para este estudio, se seleccionó el NFO-CTO ($NiFe_2O_4/Ce_{0.8}Tb_{0.2}O_{2-\delta}$) como composite. Este material ya ha sido estudiado en nuestro laboratorio, y mostró una gran estabilidad en atmosferas de CO_2, pero con baja permeación de O_2 en comparación con otros composites. Este estudio mostró resultados interesantes, y se combinó con medidas de espectroscopia de impedancia electroquímica (EIS), utilizadas habitualmente para estudiar electrodos para pilas de combustible de óxido sólido (SOFC) y pilas de electrólisis de óxido sólido (SOEC). El segundo estudio sobre composites para OTMs se centró en el aumento de la permeación de oxígeno con composites

basados en espinela-fluorita. En este caso, el transporte de oxígeno está controlado, además de por la temperatura y el gradiente de pO_2, por la conductividad ambipolar, en la que intervienen las conductividades eléctrica e iónica. Así, se cambió la fase de NFO por la fase de CMO (Co_2MnO_4) que tiene mayor conductividad total que el NFO. El composite resultante (CMO-CTO) ha mostrado un mayor rendimiento que el material predecesor NFO-CTO.

Como se ha mencionado anteriormente, el otro estudio sobre OTM se realizó con membranas basadas en BSCF. En este estudio, la membrana capilar BSCF fue electrificada para aumentar la temperatura de la membrana por efecto Joule y como consecuencia un aumento en la permeación de oxígeno. Además, se estudió este efecto bajo deshidrogenación oxidativa de etano, obteniéndose una mejora importante para las membranas BSCF electrificadas en comparación con las membranas BSCF no electrificadas. Estos estudios abren las puertas al uso de ellas con reactores a más baja temperatura.

El último estudio se centra en la revalorización del CO_2 mediante el reformado de metano por ciclos químicos. Los ciclos químicos están basados en las propiedades redox del catalizador y las dos etapas de reducción y oxidación del catalizador. La reducción del catalizador es realizada mediante temperatura y en condiciones inertes o con corrientes reductoras como por ejemplo en metano. Los estudios se centran en la reducción a través de metano que trabaja a temperaturas más bajas que para corrientes inertes y, además, proporciona corrientes de *syngas* (mezcla de CO y H_2) en la etapa de reducción del catalizador, que mejora la eficiencia global del proceso. La revalorización del CO_2 se realizaba en la etapa de oxidación del catalizador. La oxidación de estos catalizadores podría formarse con flujos de H_2O y/o CO_2 a altas temperaturas 700-1000 °C. Nuestro estudio se centra en óxidos de cerio dopados al 10% con elementos trivalentes, generalmente lantánidos. En este estudio se correlacionó la velocidad de *splitting* del CO_2 en la etapa de oxidación con el volumen de celda de la estructura cristalina y la conductividad total de estos materiales.

Resum

Aquesta tesi està centrada en la combinació de diferents tecnologies per millorar les tecnologies emergents de captura i emmagatzematge de carboni (CSS) i la revalorització del CO_2 capturat. La principal tecnologia estudiada en aquesta tesi van ser les membranes de transport d'oxigen (OTMs), les quals poden produir oxigen pur de manera més flexible que les actuals tecnologies de producció d'oxigen, com la destil·lació criogènica de l'aire. La producció d'oxigen pur és crucial per al desenvolupament de reactors d'oxicombustió que podrien ser més eficients per a la captura de CO_2 que els reactors actuals de combustió amb aire. Els estudis sobre OTMs es van dividir en dos temes principals: membranes composites de dos fases estables en CO_2 i membranes basades en BSCF ($Ba_{1-x}Sr_xCo_{1-y}Fe_yO_{3-\delta}$). D'altra banda, per a la revalorització del CO_2 capturat, es va estudiar la tecnologia de looping químic basada en catalitzador d'òxid de ceri, que aprofita les propietats redox del catalitzador a diferents pO_2 i altes temperatures (entre 700-1400 ºC).

En general, les principals etapes limitants en OTMs són la transferència d'oxigen a través de la membrana i les reaccions superficials. Per això, una millora en les propietats de la capa catalítica podria millorar la permeació total d'oxigen. El primer estudi sobre membranes bifàsiques es va centrar en l'estudi de capes catalítiques amb diferents proporcions de ambdues fases. Per a aquest estudi, es va seleccionar el NFO-CTO ($NiFe_2O_4/Ce_{0.8}Tb_{0.2}O_{2-\delta}$) com a composite. Aquest material ja ha sigut estudiat en el nostre laboratori, i va mostrar una gran estabilitat en atmosferes de CO_2, però amb baixa permeació d'O_2 en comparació amb altres composites. Aquest estudi va mostrar resultats interessants, i es va combinar amb mesures d'espectroscòpia d'impedància electroquímica (EIS), utilitzades habitualment per estudiar elèctrodes per a piles de combustible d'òxid sòlid (SOFC) i piles d'electròlisi d'òxid sòlid (SOEC). El segon estudi sobre composites per a OTMs es va centrar en l'augment de la permeació d'oxigen amb composites basats en espinela-fluorita. En aquest cas, el transport d'oxigen està controlat, a més de per la temperatura i el gradient de pO_2, per la conductivitat ambipolar, en la qual intervenen les conductivitats elèctrica i iònica. Així, es va canviar la fase de NFO per la fase de CMO (Co_2MnO_4) que té una major conductivitat total que el NFO. El composite resultant (CMO-CTO) ha mostrat un major rendiment que el material predecessor NFO-CTO.

Com s'ha mencionat anteriorment, l'altre estudi sobre OTM es va realitzar amb membranes basades en BSCF. En aquest estudi, la membrana capil·lar BSCF va ser electrificada per augmentar la temperatura de la membrana per efecte Joule i com a conseqüència un augment en la permeació d'oxigen. A més, es va estudiar aquest efecte sota deshidrogenació oxidativa d'età, obtenint-se una millora important per a les membranes BSCF electrificades en comparació amb les membranes BSCF no electrificades. Aquests estudis obren les portes a l'ús d'elles amb reactors a una temperatura més baixa.

L'últim estudi es centra en la revalorització del CO_2 mitjançant el reformat de metà per cicles químics. Els cicles químics estan basats en les propietats redox del catalitzador i les dues etapes de reducció i oxidació del catalitzador. La reducció del catalitzador és realitzada mitjançant temperatura i en condicions inertes o amb corrents reductores com per exemple en metà. Els estudis se centren en la reducció a través de metà que treballa a temperatures més baixes que per a corrents inertes i, a més, proporciona corrents de *syngas* (barreja de CO i H_2) en l'etapa de reducció del catalitzador, que millora l'eficiència global del procés. La revalorització del CO_2 es realitzava en l'etapa d'oxidació del catalitzador. L'oxidació d'aquests catalitzadors podria formar-se amb fluxos de H_2O i/o CO_2 a altes temperatures 700-1000 ºC. El nostre estudi es centra en òxids de ceri dopats al 10% amb elements trivalent, generalment lantànids. En aquest estudi es va correlacionar la velocitat de *splitting* del CO_2 en l'etapa d'oxidació amb el volum de cel·la de l'estructura cristal·lina i la conductivitat total d'aquests materials.

1.

INTRODUCTION

1. Introduction

1.1. Climatic change and CO_2 as a greenhouse gas

One of the major challenges of this century to be addressed by the technical and scientific community is mitigating climatic change. The actual climatic change is correlated to increased CO_2 concentration in the atmosphere. This increase produces greenhouse effects that bring an increase in the global temperature[1]. Also, it could break the global natural ecosystem by increasing the melting of the polar ice caps, rising sea levels, increasing desertification, more extreme natural phenomena, etc[2].

The CO_2 emissions have been increasing since the Industrial Revolution, but those emissions were focused on the most developed countries and close to the industrial areas. With globalization, this problem has extended to the whole world. Recently, it was discovered that there is a real tendency between the emissions of CO_2 and the level of development of a country. In this matter, several huge countries, like Brazil, China, India, etc., have been passing through high industrialization with the consequent increase in their CO_2 emissions. This, added to the existing countries with high industrialization, leads to a worrisome increase in global CO_2 emissions, increasing from 280 ppm to 400 ppm from 1850 until these days[3]. Also, it has to be mentioned that globalization has brought about a considerable increase in the transport of people and goods. This also has a severe effect on CO_2 emissions around the globe. Moreover, these emissions are distributed and in constant movement, making eliminating and controlling them very difficult.

The first intents of mitigating the emissions of CO_2 were mainly focused on industrial processes because their emissions are concentrated in specific locations (normally chimneys), in contrast to the emissions due to the transport industry. In order to control and decrease greenhouse gas emissions, it is important to improve and develop the current and new carbon capture and storage (CCS) technologies [4,5]. The main part of CO_2 emissions from the industry comes from combustion processes. In these matters, CCS could be divided into different types of combustion processes, depending on where it will capture the CO_2. Generally, the CCS in combustion processes could be separated into two types, depending on where the carbon is extracted: pre-combustion CCS and post-combustion CCS.

1.1.1. CO_2 capture, storage and valorisation

As mentioned in the previous part, there are different strategies to apply CCS depending on when and how the CO_2 is extracted. Generally, there are three types of strategy (represented in Figure 1. 1): post-combustion, pre-combustion and oxycombustion.

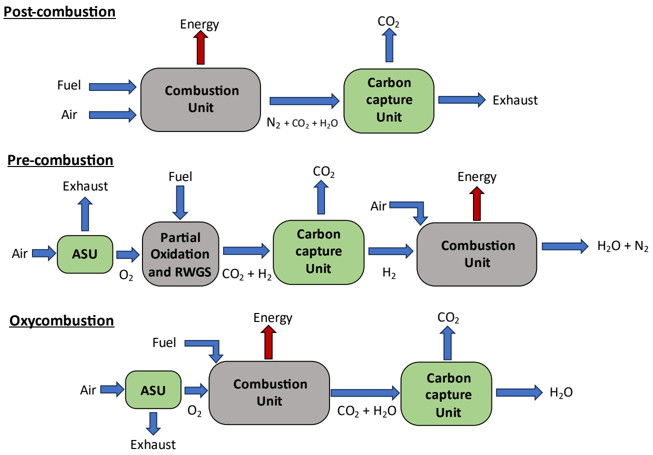

Figure 1. 1. Conceptual schemes for the three different carbon capture-based technologies: Post-combustion, pre-combustion and oxy-combustion.

For CCS technologies, the most mature strategy is considered for post-combustion processes because most studies are focused on current problems in the industry. Here, different CCS technologies were developed depending on the CO_2 concentration and the contaminants in the objective stream. The most used technologies are chemical absorption, solid adsorption, membrane separation and cryogenic distillation. The highest extended technology is the amine adsorption technology. The CO_2 is captured in the solvent at temperatures between 40-60 °C. Then, in order to regenerate the solvent, the CO_2 is released from the amine solution at 100-120 °C. One of the problems of the amine solution is the high energy consumption during the regeneration, as well as other issues related to equipment corrosion and amine degradation[6]. The main improvement of this technology comes from using better amine solvents. Another mature technology is solid adsorption, where the most common adsorbents are KOH and zeolites. However, these solutions are limited to the low ratios of CO_2/N_2 and the high influence on the gas temperature. Those issues are also important in membrane separation techniques and cryogenic distillation. Table 1. 1 represents an overview of CCS for post-combustion processes.

Table 1. 1. State of the art of principal technologies for CCS[7].

Technologies	**Capacity (10^3 tpd)**	**CO_2 feed (%)**	**Capture rate (%)**	**Companies**
Amine solvents	*0.1 – 4*	*3 – 25*	*85 – 97*	*-Air Liquide* *-Caboncapt Technologies CO. LTD.* *-Aker Carbon Capture*
Cryogenic distillation	*1 – 15*	> 40	*90 – 98*	*-Air Liquide*
PSA + Cryogenic	*0.3 – 10*	≥ 15	*98 – 99*	*-Air Liquide*
Carbonates	~ 7	≥ 20	≥ 95	*-Capsol Technologies* *-Heirloom* *-K2-*CO_2 *-Carbon Engineering LTD.**

In the case of the pre-combustion strategy, the principal concept consists of extracting the carbon from the fuel before the combustion process, ***Figure 1. 1***. For this purpose, the fuel is pretreated to produce syn gas by partial oxidation or steam reforming. Also, it is essential to convert the produced CO to CO_2. It is also common to add more steam, improving the water gas shift reaction. When the fuel is fully converted to a mixture of CO_2 and H_2, this H_2 is separated with membranes and transported to the combustion chamber. Then, combustion is produced between O2 and H2 without carbon's presence. As mentioned, capturing carbon from fuels in precombustion processes has several complex reactions before the combustion chamber. These reactions are not easy to be conducted for the large and different types of fuels used in industry.

In addition, the oxy-combustion process has recently been taken up again as an alternative to the traditional combustion process, Figure 1. 1. This process has been considered since it is more efficient and more accessible to capture CO_2 from the exhaust streams than traditional combustion processes [8,9]. However, for this process, more efficient technologies have to be developed to produce pure oxygen.

It also has to be mentioned that not only the capture of the CO_2 emission is important. Also, it is essential to develop technologies that are able to transform CO2 into more high-value compounds such as fuels or fundamental chemicals (methanol, benzene, etc.). For example, CO_2 is commonly used as a reactant for reforming reactions with organic compounds, such as dry reforming of methane, CO_2 hydrogenation to formic acid, reverse water gas shift, etc[10]. Several technologies have been developed for these applications in the past years. One of the most promising technologies is those focused on splitting water and CO_2 to produce syngas. Syngas is a mixture of CO and H2 that is the starting point for the production of more valuable compounds such as fuels or fundamental chemicals.

1.1.2. Oxycombustion processes for CO_2 capture

Recently, the oxy-combustion process has been considered as an alternative to traditional combustion processes since it is more efficient and easier to capture CO_2 from the exhaust gases[8,9]. For traditional combustion processes, the O_2 involved in the combustion comes from air streams. As it is well known, the air contains 21% of O_2, 78% of N_2 and other gasses like Ar, CO_2, H_2O, etc. The main reaction carried out during combustion is that between the O_2 and the fuel (hydrocarbons), Eq. 1. 1. Like the major component in the air is the N_2, the CO_2 and H_2O will be diluted in the exhaust stream. Also, N_2 is generally an inert gas, but in combustion processes, it could react with the O_2 at high temperatures, forming NO_x. On the contrary, in the oxycombustion process, there is no presence of N_2, so the exhaust will be a mixture of CO_2 and H_2O, being easily separated by condensation[11].

$$C_xH_y + O_2 \rightarrow CO_2 + H_2O \qquad \text{Eq. 1.1}$$

However, if the reaction only takes place with O_2, then the flame temperature control will be very complicated. In order to solve these issues, recirculating part of the exhaust gases to the inlet stream is common. This recirculation could be with only CO_2, after the condensation of the water, or could be with a mixture of CO_2 and H_2O[12]. The main difference between the two of them is the different energy savings. In the case of pure CO_2, the mix with the fuel and the O_2 will be at a low temperature. In the case of the mixture of CO_2 and H_2O, this stream could increase the temperature for fuel and the O_2 stream before the reactor, but the water will be affected later during the reaction. Both solutions had their advantages and disadvantages, and for that reason, they have to be studied for each case. However, the principal issue with this technology is the supply of pure oxygen. In this matter, air separation units (ASU) have to be developed and improved in order to produce pure oxygen more efficiently.

1.1.3. Oxygen production

For effectively using the oxy-combustion process, it is essential to improve the technologies capable to produce pure oxygen more efficiently than those already existing[8]. The most mature technology for pure O_2 production is cryogenic air distillation, which is capable of producing up to 30,000 $m^3 \cdot h^{-1}$ of O_2 with more than

95% oxygen purity[5,8]. In this matter, this technology operates at cryogenic temperatures and high vacuum to separate the oxygen from the air. For this reason, cryogenic distillation from air demands large energy consumption. Nerveless, this process has been developed for more than 100 years, being this technology optimal for big-scale oxygen production[5]. However, the production of O_2 is also essential in small and medium-scale applications. In this matter, several different technologies have been developed, like pressure and temperature adsorption, chemical looping, ionic transport membranes, polymeric membranes and others[8].

Pressure and temperature adsorption are based on the different polarization for the different compounds in the air. In this case, the N_2 is more polarizable than the O_2 absorbed by a sorbent (liquid or solid). This is a physical interaction, so the regeneration of the sorbent is not complex. Also, this technology operates at temperatures below 150 ºC and atmospheric conditions. However, for oxygen production with high purity, large amounts of sorbents are needed due to their quick deactivation, making this technology very difficult for large times operations and high-oxygen-purity productions.

In the case of chemical looping, the pure oxygen is extracted from the reduction of inorganic materials at high temperatures, at temperatures above 1200 ºC. Some materials with redox properties are reduced at these high temperatures, thus releasing O_2. The interesting fact of this technology comes from the other part of the cycle when the material can be re-oxidized with H_2O and/or CO_2 producing H_2 or syngas. Regardless, this technology operates at very high temperatures, and that requires large energy consumption for its operation. It is a very interesting option for producing pure O_2 and revalorizing CO_2 to high-value syngas in the same process.

Another appealing technology is the use of oxygen transport membranes (OTMs) for obtaining pure O_2. These membranes are formed by dense ceramic compounds presenting ionic and/or electronic conductivity properties. Depending on the conductivity properties of the material, this oxygen production takes place from a driving force between both sides of the membrane. This driving force could be an electrical potential or oxygen concentration gradient. In addition, these properties are favored at high temperatures, for that reason, OTMs operate at high temperatures, between 700 ºC to 1000 ºC. This technology has still been developed to scale up, but in the future, it could be an interesting technology for producing O2 on medium and small scales.

1.2. Mixed ionic and electronic conductivity materials (MIEC) for O_2 production

1.2.1. MIEC membranes and oxygen transport mechanism

Advanced ceramic materials with redox properties, like mixed ionic and electronic conductivity (MIEC), could be used to develop membranes with 100% selectivity to the oxygen transport. This O_2 is transported through the crystal defects (oxygen vacancies, interstitial oxygen, electronic defects, etc.) in MIEC-dense membranes. Those defects and the ability to transport oxygen are related to both conductivities, ionic and electronic. However, the factors that control both conductivities are different from each other. In general, the electronic conductivity is related to the bandgap and the ionic conductivity is related to the crystal structure[13]. The most considered materials that show MIEC properties had perovskite crystal structure (ABO_3). In general, for these materials, when A site is doped with different lanthanides or alkali-earth, it will affect ionic conductivity. Also, the combinations of different metals in the B site will impact the electronic conductivity. The MIEC properties are highly influenced by the temperature and the oxygen partial pressure. Using these materials as dense membranes gives the possibility of extracting oxygen from different sources with more than 99.99% purity.

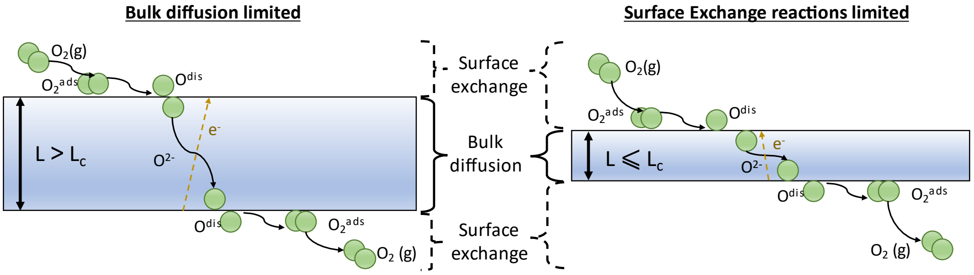

Figure 1. 2. Limiting steps for oxygen separation with OTMs. Left: limited by bulk diffusion; Right: limited by surface exchange reactions.

However, the oxygen transport through a dense ceramic membrane not only depends on the MIEC properties of the materials. Also, it depends on the thickness of the oxygen transport membrane (OTM), Figure 1. 2. Generally, OTMs will be limited by surface exchange reactions or bulk diffusion, depending on the thickness of the membrane (L). The main difference between both limiting steps is the critical thickness of the membrane (L_c). This thickness can be calculated by considering the diffusion coefficient (D_{chem}) and the surface exchange reaction coefficient (k_{chem}), Eq. 1. 2. D_{chem} and k_{chem} can be obtained by making use of experimental methods like O^{18}- O^{16} isotopic exchange and conductivity relaxation [14–19].

$$L_c = \frac{D_{chen}}{k_{chem}} \qquad \text{Eq. 1. 2}$$

When bulk diffusion is the limiting step, the oxygen flux through the MIEC membrane responds to the Wagner equation (Eq. 1. 3)[13,20,21].

$$J_{O_2} = \frac{R\cdot T}{4\cdot F^2\cdot L}\int_{P''_{O_2}}^{P'_{O_2}} \sigma_{amb}\, d\ln P_{O_2} \qquad \text{Eq. 1. 3}$$

$$\sigma_{amb} = \frac{\sigma_i\cdot\sigma_e}{\sigma_{tot}} = \frac{\sigma_i\cdot\sigma_e}{(\sigma_i+\sigma_e)} \qquad \text{Eq. 1. 4}$$

Where R corresponds to the ideal gas constant, T is the membrane temperature, F is the Faraday constant, σ_{amb} is the ambipolar conductivity (Eq. 1.4) and the P'_{O2} and P''_{O2} are the oxygen partial pressure for each side of the membrane. Here, the driving force for OTMs is the different oxygen partial pressure between both sides of the membrane. Also, the oxygen transport processes are directly favored at high temperatures, between 700 ºC and 1000 ºC. Nevertheless, the oxygen flux is also influenced by the membrane thickness, as it can see in Eq. 1. 3 and in Figure 1. 2. In order to minimize the resistance for bulk diffusion, the optimal thickness in OTMs should be the critical thickness (L_c). But normally, this L_c does not ensure the mechanical stability of the ceramic membrane.

Conversely, surface exchange reactions control the process when the membrane thickness is lower than the critical thickness, Figure 1. 2. However, the surface exchange reactions had different behavior than bulk diffusion. Here, more factors have to be taken into account like flux of gases, sweep gas properties, oxygen partial pressure, surface active sites and also the temperature and the MIEC properties on the surface. Even so, CFD studies for a common membrane show how the resistance on each side depends on the temperature, Figure 1. 3 [22,23]. Here, the sweep side had higher resistance at higher temperatures, and it changed at lower temperatures, independently of the membrane thickness. Nevertheless, experimental results show that surface exchange reactions at the sweep side are more relevant than on the feed side[23,24]. Experimental results are very affected by the different factors mentioned before.

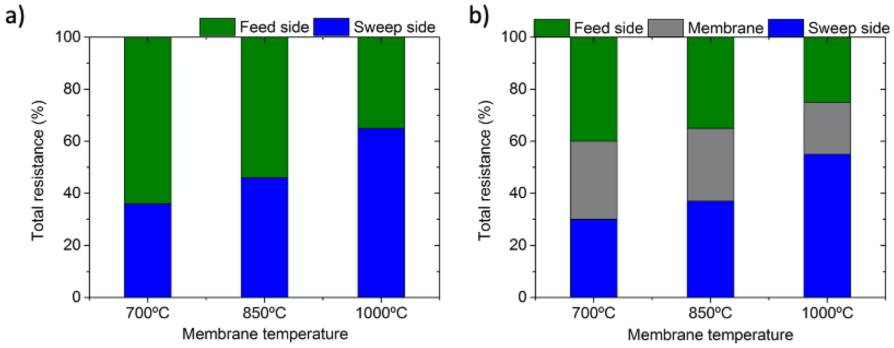

Figure 1. 3. CFD study for different resistances in BSCF OTMs with thickness: a) 10 μm; b) 1000 μm [22].

One of the most considered strategies to improve the surface exchange reactions is the addition of a catalytic layer on each membrane surface. This will increase the surface-active sites and, in consequence, will produce an increase in O_2 permeation. Several studies show that the optimal thickness of this catalytic layer is in the range of 20-40 μm. However, the porosity of the catalytic layer is also important[22,25].

Furthermore, the O_2 permeation can be improved by increasing the main driving force, which is the oxygen partial pressure gradient between both sides of the membrane[23]. This can be achieved by increasing the pressure on the feed side or by applying a vacuum on the sweep side. However, the membrane needs to present good mechanical stability at these operation pressures. That can be done by increasing the thickness of the membrane (above 400 μm). Also, it can be changed the structure of the membrane by increasing the thickness of one catalytic layer, which is known as an asymmetric membrane.

Other important factors are the gas streams on different sides of the membrane. In this matter, lower fluxes can bring a considerable difference between the oxygen partial pressure on the surface of the membrane and inlet gas, creating a polarization resistance on this surface, more significant at the sweep side. Many researchers commonly reported this flow resistance, and it disappears, increasing the stream flow on both sides [26,27]. Additionally, the polarization resistances at the sweep chamber are different depending on the gas used (He, Ar, CO_2, etc.). Where the bigger molecular size of the sweep gas will bring better sweep force[22]. In this matter, CO_2 will be a good sweep gas and can be considered in oxy-combustion processes for better sweeping. Nevertheless, the most used materials for OTMs are not stable in operation conditions under CO_2 environments.

1.2.2. Oxygen permeability and stability in Perovskite-type oxygen transport membranes (OTMs)

In order to be competitive with the current oxygen production technologies, an OTM must achieve O_2 permeation fluxes of at least 10 NmL·min^{-1}·cm^{-2} [28]. The first oxygen transport membranes reported in 1985 were based on perovskite crystal structures (ABO_3) by Teraoka et al[29]. In these studies, $SrCo_{0.8}Fe_{0.2}O_{3-\delta}$ showed the highest oxygen permeation and opened the gates to study the OTMs technology with ceramic materials. Even so, these first materials were unstable under realistic operation conditions due to their decomposition from the cubic perovskite structure to an orthorhombic brownmillerite structure. These structures are more constrained, and they perform worse O_2 permeation rates than the cubic structure. Years later, in 2000, Shao and coworkers reported a study focusing on the $Ba_{0.5}Sr_{0.5}Co_{0.8}Fe_{0.2}O_{3-\delta}$ (BSCF) as an OTMs that resulted in one of the most OTM publications. This membrane exhibits high and stable oxygen permeation under air and inert gas gradient. In the case of a membrane with 1 mm of thickness, BSCF provides around 3 mL·min^{-1}·cm^{-2} at 900 ºC [30,31]. In addition, BSCF has the highest oxygen permeation described in the bibliography, reaching almost 68 mL·min^{-1}·cm^{-2} at 1000 ºC [32]. As the $SrCo_{0.8}Fe_{0.2}O_{3-\delta}$, the cubic perovskite structure is the active phase for oxygen transport in OTMs. However, the cubic phase of the BSCF changed to a hexagonal phase below 850 ºC. This hexagonal phase is less active for oxygen diffusion. Recent studies show how the addition of small amounts of yttrium into the B site stabilize the cubic perovskite structure at temperatures below 850 ºC [33–35]. Table 1. 2 represents some oxygen permeation values for different OTM with perovskite crystal structures.

Table 1. 2. Oxygen permeation values for different perovskite types of OTMs.

OTM	Feed / sweep	L (mm)	T (ºC)	J_{O2} ($mL\cdot min^{-1}\cdot cm^{-2}$)	Ref.
$Ba_{0.5}Sr_{0.5}Co_{0.8}Fe_{0.2}O_{3-\delta}$	Air/Ar	1.0	850	2.46	22
$La_{0.4}Sr_{0.6}Co_{0.2}Fe_{0.8}O_{3-\delta}$	Air/N_2	0.8	850	0.40	36
$Ba_{0.5}Sr_{0.5}Co_{0.8}Fe_{0.1}Y_{0.1}O_{3-\delta}$	Air/He	1.2	850	1.04	33
$SrFeO_{3-\delta}$	Air/He	1.0	850	0.45	37
$SrCo_{0.5}Fe_{0.5}O_{3-\delta}$	Air/Ar	1.0	850	0.60	38
$SrCo_{0.4}Fe_{0.6}O_{3-\delta}$	Air/He	1.0	850	2.16	29
$SrTi_{0.75}Fe_{0.25}O_{3-\delta}$	Air/Ar	0.5	850	0.02	39
$SrTi_{0.75}Co_{0.25}O_{3-\delta}$	Air/Ar	0.5	850	0.16	
$La_{0.6}Ca_{0.4}Co_{0.3}Fe_{0.7}O_{3-\delta}$	Air/He	1.0	850	0.70	40
$Pr_{0.6}Sr_{0.4}Co_{0.5}Fe_{0.5}O_{3-\delta}$	Air/He	1.0	850	0.20	41
$PrBaCo_2O_{5+\delta}$	Air/He	0.7	850	0.49	42
$SmBaCo_2O_{5+\delta}$	Air/He	0.7	850	0.13	
$Ba_2In_{1.8}Cr_{0.2}O_{5+\delta}$	Air/He	1.0	850	1.20	43

Moreover, the OTMs can be used in catalytic membrane reactors (CMRs) for the conduction of different reactions [44–48]. CMRs have been studied for several relevant reactions represented in Figure 1. 4, such as oxy-combustion, partial oxidation of methane (POM), water splitting, and oxidative dehydrogenation of ethane (ODHE), to name a few [49–54].

However, in general, these perovskites were not stable in CO_2 atmospheres. The alkaline earth elements react with the CO_2, producing the corresponding carbonates, or they interact with the CO_2, blocking the active sites that entail a decrease in the oxygen permeation[20]. Some efforts to improve the stability of perovskites on CO_2 have been made in the past years by doping with different elements. The most significant consisted of doping the A site with lanthanides, like

La, Pr, etc[36,40,41]. Nevertheless, the obtained O_2 permeation rates of these formulations under CO_2 atmospheres were lower than when using any other sweep gases.

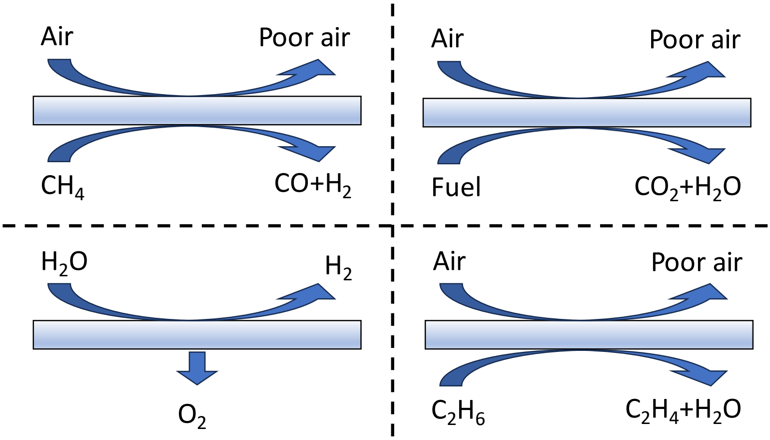

Figure 1. 4. Different possible reactions for OTM as catalytic membrane reactors.

Nowadays, increasing the tolerance to CO_2 environments is fundamental to incorporating OTMs in oxy-combustion processes. A recent helpful study demonstrates that adding protective and catalytic layers like $Ce_{0.8}Gd_{0.2}O_{2-\delta}$ in BSCF membranes could be a solution to avoid the degradation of OTMs under CO_2 environments[55].

Despite the stability issues, there are some other efforts to scale up perovskite as OTMs, generally for BSCF-based membranes. Here, the principal issue is the sealing of the membrane into the reactor. Normally, the membrane had to be sealed inside the reactor on alumina or metal alloys. There are several limitations due to the high difference in the thermal expansion coefficient (TEC) between the membrane material and the reactor material[56]. The BSCF has a TEC around $20\cdot10^{-6}$ K^{-1}, comparably higher than materials used in oxide fuel cells (SOFC) where the TECs for sealings and reactors materials are close to common electrolytes as YSZ or CGO ($10\sim12\cdot10^{-6}$ K^{-1}) [57–59]. In the case of tubular membranes, a solution can be conducting a cold seal outside of the reactor. Even so, there are possibilities for the membrane to break due to a thermal shock. There are also studies for BSCF OTMs focused on metallic alloys for sealing and steels with TECs closer to BSCF, but this solution might be expensive for being commercialized [60,61]. Also, these reactors could be poisoned with the CO_2 present in the feed air for extended periods of operation.

Ruddlesden-Poppers phases A_2BO_4 are also MIEC materials with high oxygen transport capacity[62–64]. They show high oxygen diffusion due to their oxygen transport being based on interstitial oxygen and not in oxygen vacancies[65–69]. Still, they usually are not fully stable in CO_2 and present instabilities under different atmospheres (pO_2 between 10^{-1}-10^{-5} bar) on both membrane sides[63,70,71]. Their TECs change between pO_2 10^{-1}-10^{-5} bar. As an example, the $TEC_{(0\text{-}1400^{\circ}C)}$ of $La_2NiO_{4+\delta}$ remains constant under air, $13\cdot10^{-6}$ K^{-1}, but in Ar (pO_2 10^{-4} bar), its $TEC_{(0\text{-}1400^{\circ}C)}$ starts at $10\cdot10^{-6}$ K^{-1} and increase until $12\cdot10^{-6}$ K^{-1} [66]. These changes in TEC values make this kind of OTM fragile under operation conditions and difficult to seal. Even so, these materials are great candidates for air electrodes in SOFC[72–74].

Table 1. 3. Oxygen permeation values for different Ruddlesden-Poppers types of OTMs.

OTM	Feed / sweep	L (mm)	T (ºC)	J_{O2} ($mL\cdot min^{-1}\cdot cm^{-2}$)	Ref.
$La_2NiO_{4+\delta}$	Air/He	0.9	850	0.31 – 0.59	63,75
$Pr_{1.9}Ni_{0.75}Cu_{0.25}O_{4+\delta}$	Air/He	0.5	850	0.51	76
$Pr_{1.9}Ni_{0.71}Cu_{0.24}Ga_{0.05}O_{4+\delta}$	Air/He	0.5	850	3.58	
$Nd_{1.9}Ni_{0.75}Cu_{0.25}O_{4+\delta}$	Air/Ar	1.0	850	0.50	77
$La_2CuO_{4-\delta}$	Air/He	1.0	850	0.19	70
$La_2Ni_{0.9}Fe_{0.1}O_{4+\delta}$	Air/He	1.0	850	0.27	63

1.2.3. Dual-phase materials for OTMs

Since perovskite OTMs are generally not stable in CO_2 environments at long-term operation, dual-phase OTMs combining materials stables to CO_2 were developed;

both materials together exhibit MIEC properties [71,78–81]. Dual-phase OTMs are more stable in CO_2 environments, and their TECs are closer to the reactor's materials, around $10·10^{-6}$ K^{-1}. However, the oxygen permeation reached for most dual-phase OTMs is lower than for perovskite OTMs. For dual-phase OTMs, the bulk diffusion is also limited by the percolative channels for both phases and their microstructure.

Depending on the natural properties of both materials, dual-phase OTMs could be made by ionic, electronic and mix ionic-electronic conductors. One of the phases for dual-phase OTMs is generally an ionic conductor, usually based on doped zirconia and doped ceria materials. These materials are commonly used as electrolytes for solid oxide fuel cells (SOFCs). They have a cubic fluorite crystal structure and are stable in CO_2 atmospheres. Also, the ionic conductivity of these oxides depends on the specific lattice composition. The most used doped zirconia materials are yttria-stabilized zirconia (YSZ) and scandium-doped zirconia (ScSZ)[82–84]. In the case of doped ceria, among the available dopants used for increasing the ionic conductivity, the most common are gadolinium-doped (CGO) and samarium-doped ceria (CSO) [85,86]. Ceria has also been doped with praseodymium or terbium, increasing their mixed ionic electronic conductivity [87,88]. The TEC for ionic conductors is very close for the alumina and the other components for an OTM stack, being ~ $10.5 \cdot 10^{-6}$ K^{-1} for zirconia doped materials and ~$12 \cdot 10^{-6}$ K^{-1} for cerium doped materials[83,89].

T.J. Mazanec et al. reported the first dual-phase OTMs in 1992 by combining the ionic conductor YSZ with different metals like palladium, platinum and indium[90]. The metal conductors had high electronic conductivity, but these dual-phase OTMs broke under inert atmospheres and/or were highly expensive and limited. In the next generation, the electronic phase was based on oxide semiconductors. The most used materials present a perovskite crystal structure where these oxide structures can be pure electronic semiconductors. One of the most considered formulations was a dual-phase with $La_{0.8}Sr_{0.2}MnO_{3-\delta}$ (LSM) as electronic phase[91]. This material was studied as a SOFC cathode and is compatible with the standard ionic conductors[92–96].

Perovskite materials with MIEC properties are also combined with ionic conductors for dual-phase OTMs[97–99]. This dual-phase material had comparable less oxygen permeation than the perovskite phase alone, but in general, they have a TEC closer to the material reactor's TEC. Even so, most of them comprise alkaline earth in the material and hence present stability challenges under CO_2 atmospheres at mid-long times of operation[79,81,97,100]. Other MIEC materials were used combined with ionic conductors for dual-phase OTMs. In the case of Ruddlesden-Poppers, materials are stable under CO2 environments, but these materials tend to degrade in the absence of oxygen [71]. Even dual-phase OTMs with MIEC materials improve the resistance to CO2, they normally are affected under its presence, blocking active sites and decreasing the oxygen permeation in all the cases[101].

Spinels (MM'_2O_2) are the second material class most used for the electronic phase in dual-phase membranes. Most of these materials are stable in CO_2, but many, especially those containing Co, Ni, or Cu, decompose in reducing atmospheres ($pO_2 < 10^{-15}$ bar)[102–106]. These dual-phase OTMs like $NiFe_2O_4/Ce_{0.8}Tb_{0.2}O_{2-\delta}$ (NFO/CTO) combined with ionic conductors exhibit high stability in CO_2 atmospheres and can even be stable in the presence of low amounts of SO_2 without permanent degradation[78,102,106,107]. Also, under CO_2, the oxygen permeation is higher than under inert gases like Ar or He. However, this material shows limited permeation rates compared to other dual-phase materials[101].

Table 1. 4. Oxygen permeation values for different dual-phase OTMs in Air/He environments. *Ar instead of He as sweep stream.

OTM	Ratio	L (mm)	T (ºC)	J_{O2} ($mL\cdot min^{-1}\cdot cm^{-2}$)	Ref.
$Ce_{0.8}Gd_{0.2}O_{2-\delta}$ / Ag	50/50	1.0	850	0.13	108
$Ce_{0.9}Gd_{0.1}O_{2-\delta}$ / $Ba_{0.5}Sr_{0.5}Co_{0.8}Fe_{0.2}O_{3-\delta}$	60/40	0.5	875	1.08	97
$Ce_{0.85}Sm_{0.15}O_{2-\delta}$ / $Sm_{0.6}Sr_{0.4}FeO_{3-\delta}$	75/25	0.5	940	0.50	109
$Ce_{0.85}Pr_{0.1}Cu_{0.05}O_{2-\delta}$ / $Pr_{0.5}Sr_{0.5}Fe_{0.95}Cu_{0.05}O_{3-\delta}$	60/40	0.6	1000	1.60	110
$Ce_{0.85}Pr_{0.1}Cu_{0.05}O_{2-\delta}$ / $Pr_{0.5}Sr_{0.5}Fe_{0.8}Al_{0.2}O_{3-\delta}$	60/40	0.6	1000 900	1.05 0.58	111
$Ce_{0.8}Gd_{0.2}O_{2-\delta}$ / $La_{0.5}Sr_{0.5}Fe_{0.8}Cu_{0.2}O_{3-\delta}$	60/40	0.6	950	0.57	112
$Ce_{0.9}Pr_{0.1}O_{2-\delta}$ / $La_{0.5}Sr_{0.5}Fe_{0.9}Cu_{0.1}O_{3-\delta}$	40/60	0.5	900	0.93	81
$Ce_{0.85}Sm_{0.15}O_{2-\delta}$ / $Sm_{0.6}Sr_{0.4}FeO_{3-\delta}$	75/25	0.5	940	0.50	109
$Ce_{0.8}Nd_{0.2}O_{2-\delta}$ / $Nd_{0.5}Sr_{0.5}Al_{0.2}Fe_{0.8}O_{3-\delta}$	60/40	0.6	1000 850	1.00 0.28	113
$Ce_{0.9}Nd_{0.1}O_{2-\delta}$ / $Nd_{0.6}Sr_{0.4}CoO_{3-\delta}$	60/40	0.6	950	0.65	114
$Ce_{0.9}Pr_{0.1}O_{2-\delta}$ / $Pr_{0.6}Sr_{0.4}FeO_{3-\delta}$	60/40	0.6	950 850	3.17 0.71	98
$Ce_{0.9}Gd_{0.1}O_{2-\delta}$ / Fe_2O_3	60/40	0.5	1000	0.18	80
$Ce_{0.9}Gd_{0.1}O_{2-\delta}$ / $La_2NiO_{4+\delta}$	40/60	0.24	950 850	1.52 0.78	71
10Sc1YSZ* / $MnCo_2O_4$	70/30	0.5	850	0.23	115
$Ce_{0.9}Gd_{0.1}O_{2-\delta}$ / $NiFe_2O_4$	70/30	1.0	850	0.05	116
$Ce_{0.8}Tb_{0.2}O_{2-\delta}$ / $NiFe_2O_4$	50/50	0.6	1000 850	0.20* 0.07*	78

Table 1. 5. Oxygen permeation values for different dual-phase OTMs with CO_2 in sweep stream.

OTM	Ratio	L (mm)	T (ºC)	J_{O2} (mL·min^{-1}·cm^{-2})	Ref.
$Ce_{0.9}Gd_{0.1}O_{2-\delta}$ / $Ba_{0.5}Sr_{0.5}Co_{0.8}Fe_{0.2}O_{3-\delta}$	60/40	0.5	875	0.27	97
$Ce_{0.8}Sm_{0.2}O_{2-\delta}$ / $Sr_2Fe_{1.5}Mo_{0.5}O_{5-\delta}$	60/40	0.6	950	0.1	117
$Ce_{0.85}Pr_{0.1}Cu_{0.05}O_{2-\delta}$ / $Pr_{0.5}Sr_{0.5}Fe_{0.95}Cu_{0.05}O_{3-\delta}$	60/40	0.6	1000	0.85	110
$Ce_{0.85}Pr_{0.1}Cu_{0.05}O_{2-\delta}$ / $Pr_{0.5}Sr_{0.5}Fe_{0.8}Al_{0.2}O_{3-\delta}$	60/40	0.6	1000 900	0.73 0.30	111
$Ce_{0.8}Gd_{0.2}O_{2-\delta}$ / $La_{0.5}Sr_{0.5}Fe_{0.8}Cu_{0.2}O_{3-\delta}$	60/40	0.6	950	0.35	112
$Ce_{0.9}Pr_{0.1}O_{2-\delta}$ / $La_{0.5}Sr_{0.5}Fe_{0.9}Cu_{0.1}O_{3-\delta}$	40/60	0.5	900	0.71	81
$Ce_{0.8}Sm_{0.2}O_{2-\delta}$ / $Sr_2Fe_{1.5}Mo_{0.5}O_{5-\delta}$	60/40	0.6	950	0.1	117
$Ce_{0.8}Nd_{0.2}O_{2-\delta}$ / $Nd_{0.5}Sr_{0.5}Al_{0.2}Fe_{0.8}O_{3-\delta}$	60/40	0.6	1000 850	0.76 0.08	113
$Ce_{0.9}Nd_{0.1}O_{2-\delta}$ / $Nd_{0.6}Sr_{0.4}CoO_{3-\delta}$	60/40	0.6	950	0.55	114
$Ce_{0.9}Pr_{0.1}O_{2-\delta}$ / $Pr_{0.6}Sr_{0.4}FeO_{3-\delta}$	60/40	0.6	950 850	2.12 0.71	98
$Ce_{0.9}Gd_{0.1}O_{2-\delta}$ / Fe_2O_3	60/40	0.5	1000	0.20	80
$Ce_{0.9}Gd_{0.1}O_{2-\delta}$ / $La_2NiO_{4+\delta}$	40/60	0.24	950 850	1.31 0.61	71
10Sc1YSZ / $MnCo_2O_4$	70/30	0.5	850	0.24	115
$Ce_{0.8}Tb_{0.2}O_{2-\delta}$ / $NiFe_2O_4$	50/50	0.6	1000 850	0.42 0.13	78

1.3. CO_2 revalorisation

Nowadays, the CO_2 is commonly used in different sectors, like food industry, metallurgy, petrochemistry and others. For example, in food industry the, CO_2 is used as a refrigerant and inert gas in food packaging and preservation. Also, it is used for carbonated drinks. In metallurgy, it is used as a treatment agent in steels and as an inert gas in welding.

The CO_2 capture and storage technologies are only a part of the transition of the decarbonization of the industry. Nowadays, it is also important to improve new technologies to transform this CO_2 using renewable energies. However, most of these resources are inherently intermittent, which requires the development of efficient energy-storage solutions. The transformation of surplus renewable energy with CO_2 into fuels is very attractive because of the high energy-storage density of fuels and the use of the synthetic molecules produced in several sectors such as long-distance transportation or industry[118].

In the present thesis, two technologies have been studied that are able to transform CO_2: thermosolar chemical looping and solid oxide electrolysis cells (SOEC). Both technologies for the valorization of CO2 are based on redox materials with MIEC properties, like doped ceria materials.

1.3.1. Thermosolar chemical looping

Thermosolar chemical looping is based on the high temperature (between 800-1400 ºC) redox properties of inorganic oxide catalysts using concentrated solar power plants. This technology consists of cycles of two principal steps: first, a reduction step and second, an oxidation step [119]. In the first step, the catalyst is partially reduced at high temperatures (between 1100-1400 ºC). In this reduction, the material releases oxygen (Eq. 1. 5), and it stays active for the next step. Then, the catalyst is re-oxidized with CO_2 and/or H_2O at the same or lower temperature (Eq.

1. 6). This reoxidation of the catalyst produces the splitting of CO_2 and H_2O, giving a mixture of CO and H_2, also known as syngas. This syngas is the principal precursor to produce liquid fuels using Fischer-Tropsch catalytic units [120,121].

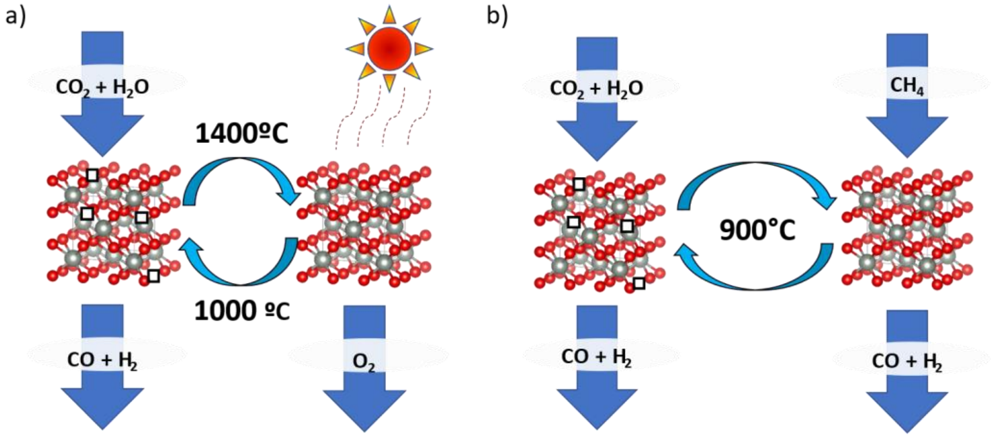

Figure 1. 5. Chemical looping diagrams for a CeO_2 (oxygen vacancies, $V_O^{\cdot\cdot}$, are depicted with white squares): a) Themosolar chemical looping; b) Chemical looping methane reforming.

$$MO_x \leftrightarrow MO_{x-\delta} + \frac{\delta}{2} O_2 \qquad \text{Eq. 1. 5}$$

$$\alpha\, CO_2 + \beta\, H_2O + MO_{x-\delta} \rightarrow MO_x + \alpha\, CO + \beta\, H_2 \qquad \text{Eq. 1. 6}$$

Where MO_x is the oxide redox catalyst and δ is the oxygen deficiency (α+β=δ). For this process, the materials most commonly used and with the highest performance are based on cerium oxide. Cerium oxide is considered the state-of-the-art material in solar-driven thermochemical syngas production based on its high stability over prolonged and repeated cycling and fast CO_2 and H_2O splitting kinetics, with more than a decade of research and development[122,123]. However, because of the high temperatures and the dependency on the weather, this technology has several issues to improve the efficiency of the process. Several efforts are being made in order to improve the thermal balance for this process[124].

Other researchers were focused on decreasing the process temperature, using redox material with a lower reduction temperature or using H_2 or CH_4 atmospheres that bring lower temperature reduction for the actual redox catalyst[125,126]. Recently also appear new physical methods have to reduce material and performance chemical looping, like, for example, using microwaves[118].

Changing the reduction step using a reducing gas not only reduces the process temperature but could also be used to improve global efficiency. In the case of using methane in the reduction step, partial oxidation of the methane (POM) and combustion reactions could appear, Eq. 1. 7 and 1. 8, respectively. These reactions could be used to improve the efficiency of the process, increasing the production of syngas in the case of the POM reaction, Figure 1. 5b. This technology gets the name of chemical looping methane reforming (CLR)

$$\frac{1}{\delta}CH_4 + MO_x \rightarrow MO_{x-\delta} + \frac{1}{\delta}\,CO + \frac{2}{\delta}\;H_2 \qquad \text{Eq. 1. 7}$$

$$\frac{1}{\delta}CH_4 + MO_x \rightarrow\; MO_{x-\delta} + \frac{1}{\delta}CO_2 + \frac{2}{\delta}\;H_2O \qquad \text{Eq. 1. 8}$$

The addition of methane in the reduction step decreases the reactor temperature to 900ºC even less, until 700 ºC with lower global reduction and activity[126]. Comparing Thermosolar chemical looping with dry reforming of methane, CLR offers additional advantages (for example, carbon depositions occurring in the POM step can be reduced by the Boudouard reaction in the CO_2 splitting step, etc.)[127]. Figure 1. 5b describes the scheme for the CLR at 900 ºC, with CeO_2 as a reference catalyst like in thermochemical looping. In this case, cerium oxide is also the material of reference.

1.3.2. Solid oxide electrolysis cells (SOEC)

Solid oxide electrolysis cells (SOEC) technology is an emerging technology based on inorganic materials capable to revalorize the CO_2 captured[128–130]. This technology has been proposed principally to produce hydrogen and syngas at high temperatures (700-1000 ºC) due to its high efficiencies and renewable sources like water, CO_2 and electricity[128,129,131–133]. Even so, the materials and configurations for SOEC are very similar to those for OTMs. In this case, the membrane has only ionic conductivity (electrolyte), and the catalytic layers also have MIEC properties (electrodes). The driving force in SOEC is an electrical overpotential on both sides of the electrolyte (V_{cell}). Figure 1. 6 represents the scheme for a SOEC in co-electrolysis mode.

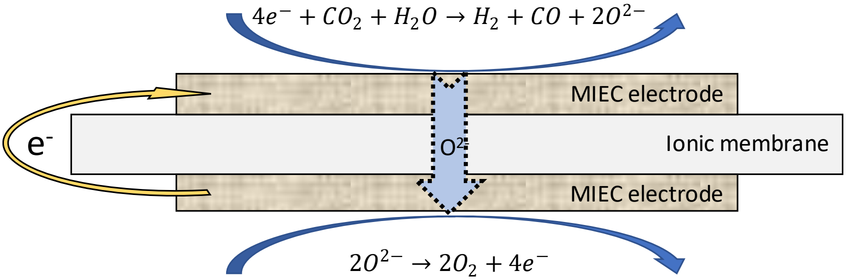

Figure 1. 6. Partial reactions in SOEC membrane for co-electrolysis mode.

As the driving force is the electrical power, the current supplied will be related to the H_2, CO and O_2 production (Eq. 1. 9).

$$F_{O_2} = \frac{I}{n_{e^-} \cdot F} \qquad \text{Eq. 1. 9}$$

Where I is the current applied, n_{e-} is the number of electrons in the oxygen partial reaction and F is the Faraday constant (96485 C·mol^{-1}). As an electrical device, it follows the ohm law (Eq. 1. 10), and the current applied depends on the voltage applied on both sides of the membrane (ΔV) and the resistance of the cell (R).

$$\Delta V = I \cdot R \qquad \text{Eq. 1. 10}$$

$$V_{cell} = V_0 + I \cdot ASR \qquad \text{Eq. 1. 11}$$

$$ASR = R_p^{cathode} + R_{electrolyte} + R_p^{anode} \qquad \text{Eq. 1. 12}$$

$$R_{electrolyte} = \frac{L}{\sigma} \qquad \text{Eq. 1. 13}$$

For SOEC devices, Ohms' law is described as Eq. 1. 11, where the cell voltage (V_{cell}) depends on the open circuit voltage (V_0) that will be defined for the co-electrolysis potential. In part of the resistance of the cell, the area-specific resistance (ASR) englobes the resistances on both electrodes (anode and cathode) and the resistance of the electrolyte at operational conditions (Eq. 1. 12). The resistance for the electrolyte depends on its conductivity (σ) and the thickness (L), Eq. 1. 13. Also, the resistance for the electrodes will be determined for their MIEC properties at each operational condition.

Generally, the conventional cells in SOEC stacks had two principal configurations: electrolyte-supported or electrode-supported. Like OTMs, the thickness of the dense membrane, in this case, the electrolyte, is one of the main aspects of good performance (Eq. 1. 13). In the case of electrolyte-supported the membrane has 200 µm thickness and the electrodes 15-30 µm of thickness [128,134]. Conversely, the electrode supported has an electrolyte thickness of around 5-30 µm, and the electrode supported is normally about 200-500 µm thickness [135,136].

In general, the electrode supported has been more studied in up-scale reactors, the Ni-YSZ ($Zr_{0.92}Y_{0.08}O_{2-\delta}$) cermet being the most common electrode supported [129,137]. For the electrolyte, the most common [85,86,88]materials had fluorite crystal structure like cerium doped materials. But in terms of stability and economy, the most common electrolyte used is the YSZ [83,84,138]. Finally, the state of the art for air electrodes are based on dual-phase materials with $La_{0.5}Sr_{0.5}MnO_{3-\delta}$ as the electronic phase and cerium/zirconium doped materials as ionic phase [91,94–96].

1.4. Scope of the thesis.

The present thesis is focused on the study of different technologies based on mixed ionic and electronic conductors (MIECs), trying to correlate and combine their different properties. In this matter, the main technology studied considered is oxygen transport membranes (OTMs) based in dual phase materials stable in CO_2. Here, it was combined electrochemical impedance spectroscopy, commonly used to study the electrodes in solid-oxide electrolysis cells, to determine the future behaviour as catalytic layers in OTMs. Another concept studied in OTMs was electrified $Ba_{0.5}Sr_{0.5}Co_{0.8}Fe_{0.2}O_{2-\delta}$-based membranes to increase the membrane temperature locally. The last study focused on how cerium-based materials affect the total conductivity in CO_2 revalorization via chemical looping methane reforming. In addition, other objectives were considered and studied during this thesis:

- Study the role of the electronic and ionic phase ratio in the surface exchange reactions for oxygen transport membranes based on NFO/CTO dual-phase material.
- Improve the oxygen permeation under CO_2 and SO_2 environments, typical from postcombustion exhausts.
- How affects the electrification in $Ba_{0.5}Sr_{0.5}Co_{0.8}Fe_{0.2}O_{2-\delta}$-based membrane as catalytic membrane reactor for oxidative dehydrogenation of ethane.
- How affects a different catalytic layer in the electrification of $Ba_{0.5}Sr_{0.5}Co_{0.8}Fe_{0.2}O_{2-\delta}$-based membrane.

1.5. References.

1. Harmsen, M. *et al.* Uncertainty in non-CO2 greenhouse gas mitigation contributes to ambiguity in global climate policy feasibility. *Nat Commun* **14**, (2023).

2. Kim, Y. H., Min, S. K., Gillett, N. P., Notz, D. & Malinina, E. Observationally-constrained projections of an ice-free Arctic even under a low emission scenario. *Nat Commun* **14**, (2023).

3. Ghoniem, A. F. *Energy Conversion Engineering: Towards Low CO2 Power and Fuels*. (Cambridge University Press, 2021).

4. Himma, N. F., Wardani, A. K., Prasetya, N., Aryanti, P. T. P. & Wenten, I. G. Recent progress and challenges in membrane-based O2/N2 separation. *Reviews in Chemical Engineering* **35**, 591–625 (2019).

5. Allam, R. J. Improved oxygen production technologies. *Energy Procedia* **1**, 461–470 (2009).

6. Gao, W. *et al.* Industrial carbon dioxide capture and utilization: State of the art and future challenges. *Chemical Society Reviews* vol. 49 8584–8686 Preprint at https://doi.org/10.1039/d0cs00025f (2020).

7. Barlow, H., Shahi, S. S. M. & Loughrey, M. *STATE OF THE ART: CCS TECHNOLOGIES 2023*. https://www.globalccsinstitute.com/resources/publications-reports-research/state-of-the-art-ccs-technologies-2023/ (2023).

8. Wu, F., Argyle, M. D., Dellenback, P. A. & Fan, M. Progress in O2 separation for oxy-fuel combustion–A promising way for cost-effective CO2 capture: A review. *Progress in Energy and Combustion Science* vol. 67 188–205 Preprint at https://doi.org/10.1016/j.pecs.2018.01.004 (2018).

9. Chen, L., Yong, S. Z. & Ghoniem, A. F. Oxy-fuel combustion of pulverized coal: Characterization, fundamentals, stabilization and CFD modeling. *Progress in Energy and Combustion Science* vol. 38 156–214 Preprint at https://doi.org/10.1016/j.pecs.2011.09.003 (2012).

10. Zheng, Y. *et al.* Energy related CO2 conversion and utilization: Advanced materials/nanomaterials, reaction mechanisms and technologies. *Nano Energy* **40**, 512–539 (2017).

11. Buhre, B. J. P., Elliott, L. K., Sheng, C. D., Gupta, R. P. & Wall, T. F. Oxy-fuel combustion technology for coal-fired power generation. *Progress in*

Energy and Combustion Science vol. 31 283–307 Preprint at https://doi.org/10.1016/j.pecs.2005.07.001 (2005).

12. Chen, L., Yong, S. Z. & Ghoniem, A. F. Oxy-fuel combustion of pulverized coal: Characterization, fundamentals, stabilization and CFD modeling. *Progress in Energy and Combustion Science* vol. 38 156–214 Preprint at https://doi.org/10.1016/j.pecs.2011.09.003 (2012).

13. Sunarso, J. *et al.* Mixed ionic-electronic conducting (MIEC) ceramic-based membranes for oxygen separation. *Journal of Membrane Science* vol. 320 13–41 Preprint at https://doi.org/10.1016/j.memsci.2008.03.074 (2008).

14. Mauvy, F. *et al.* Chemical oxygen diffusion coefficient measurement by conductivity relaxation-correlation between tracer diffusion coefficient and chemical diffusion coefficient. *J Eur Ceram Soc* **24**, 1265–1269 (2004).

15. Geffroy, P. M., Blond, E., Richet, N. & Chartier, T. Understanding and identifying the oxygen transport mechanisms through a mixed-conductor membrane. *Chemical Engineering Science* vol. 162 245–261 Preprint at https://doi.org/10.1016/j.ces.2017.01.006 (2017).

16. Cox-Galhotra, R. A. & McIntosh, S. Unreliability of simultaneously determining kchem and D chem via conductivity relaxation for surface-modified La 0.6Sr0.4Co0.2Fe0.8O 3-δ. *Solid State Ion* **181**, 1429–1436 (2010).

17. Solís, C., Escolastico, S., Haugsrud, R. & Serra, J. M. La5.5WO12-δ characterization of transport properties under oxidizing conditions: A conductivity relaxation study. *Journal of Physical Chemistry C* **115**, 11124–11131 (2011).

18. Geffroy, P. M., Fouletier, J., Richet, N. & Chartier, T. Rational selection of MIEC materials in energy production processes. *Chem Eng Sci* **87**, 408–433 (2013).

19. Nicollet, C. *et al.* Acidity of surface-infiltrated binary oxides as a sensitive descriptor of oxygen exchange kinetics in mixed conducting oxides. *Nat Catal* (2020) doi:10.1038/s41929-020-00520-x.

20. Arratibel Plazaola, A. *et al.* Mixed Ionic-Electronic Conducting Membranes (MIEC) for Their Application in Membrane Reactors: A Review. *Processes* **7**, 128 (2019).

21. Wu, X. Y. & Ghoniem, A. F. Mixed ionic-electronic conducting (MIEC) membranes for thermochemical reduction of CO2: A review. *Prog Energy Combust Sci* **74**, 1–30 (2019).

22. Catalán-Martínez, D., Santafé-Moros, A., Gozálvez-Zafrilla, J. M., García-Fayos, J. & Serra, J. M. Characterization of oxygen transport phenomena on BSCF membranes assisted by fluid dynamic simulations including surface exchange. *Chemical Engineering Journal* **387**, (2020).

23. Zhu, X., Liu, H., Cong, Y. & Yang, W. Permeation model and experimental investigation of mixed conducting membranes. *AIChE Journal* **58**, 1744–1754 (2012).

24. Joo, J. H. *et al.* Dramatically enhanced oxygen fluxes in fluorite-rich dual-phase membrane by surface modification. *Chemistry of Materials* **26**, 4387–4394 (2014).

25. Hong, W. K. & Choi, G. M. Oxygen permeation of BSCF membrane with varying thickness and surface coating. *J Memb Sci* **346**, 353–360 (2010).

26. Baumann, S. *et al.* Ultrahigh oxygen permeation flux through supported Ba0.5Sr0.5Co0.8Fe0.2O3-δ membranes. *J Memb Sci* **377**, 198–205 (2011).

27. Zhang, C., Xu, Z., Chang, X., Zhang, Z. & Jin, W. Preparation and characterization of mixed-conducting thin tubular membrane. *J Memb Sci* **299**, 261–267 (2007).

28. Bose, A. C. *Inorganic Membranes for Energy and Environmental Applications*. *Inorganic Membranes for Energy and Environmental Applications* (Springer New York, 2009). doi:10.1007/978-0-387-34526-0.

29. Teraoka, Y., Zhang, H.-M., Furukawa, S. & Yamazoe, N. OXYGEN PERMEATION THROUGH PEROVSKITE-TYPE OXIDES. *Chem Lett* **14**, 1743–1746 (1985).

30. Catalán-Martínez, D., Santafé-Moros, A., Gozálvez-Zafrilla, J. M., García-Fayos, J. & Serra, J. M. Characterization of oxygen transport phenomena on BSCF membranes assisted by fluid dynamic simulations including surface exchange. *Chemical Engineering Journal* **387**, 124069 (2020).

31. Liu, S. & Gavalas, G. R. Oxygen selective ceramic hollow fiber membranes. *J Memb Sci* **246**, 103–108 (2005).

32. Baumann, S. *et al.* Ultrahigh oxygen permeation flux through supported Ba0.5Sr0.5Co0.8Fe0.2O3-δ membranes. *J Memb Sci* **377**, 198–205 (2011).

33. Haworth, P., Smart, S., Glasscock, J. & Diniz Da Costa, J. C. Yttrium doped BSCF membranes for oxygen separation. *Sep Purif Technol* **81**, 88–93 (2011).

34. Almar, L. *et al.* Improved Phase Stability and CO2 Poisoning Robustness of Y-Doped Ba0.5Sr0.5Co0.8Fe0.2O3-δ SOFC Cathodes at Intermediate Temperatures. *ACS Appl Energy Mater* **1**, 1316–1327 (2018).

35. Haworth, P., Smart, S., Glasscock, J. & Diniz Da Costa, J. C. High performance yttrium-doped BSCF hollow fibre membranes. *Sep Purif Technol* **94**, 16–22 (2012).

36. Gaudillere, C., Garcia-Fayos, J. & Serra, J. M. Enhancing oxygen permeation through hierarchically-structured perovskite membranes elaborated by freeze-casting. *J Mater Chem A Mater* **2**, 3828–3833 (2014).

37. Zhang, Z., Chen, D., Dong, F. & Shao, Z. Efficient and CO2-tolerant oxygen transport membranes prepared from high-valence B-site substituted cobalt-free SrFeO3-δ. *J Memb Sci* **495**, 187–197 (2015).

38. Shin, M. J. & Yu, J. H. Oxygen transport of A-site deficient Sr 1-xFe 0.5Co 0.5O 3-δ (x=0-0.3) membranes. *J Memb Sci* **401–402**, 40–47 (2012).

39. Liu, Y., Baumann, S., Schulze-Küppers, F., Mueller, D. N. & Guillon, O. Co and Fe co-doping influence on functional properties of SrTiO3 for use as oxygen transport membranes. *J Eur Ceram Soc* **38**, 5058–5066 (2018).

40. Chen, G. *et al.* High flux and CO2-resistance of La0.6Ca0.4Co1–Fe O3− oxygen-transporting membranes. *J Memb Sci* **590**, 117082 (2019).

41. Partovi, K., Liang, F., Ravkina, O. & Caro, J. High-flux oxygen-transporting membrane Pr0.6Sr 0.4Co0.5Fe0.5O3-δ;: CO 2 stability and microstructure. *ACS Appl Mater Interfaces* **6**, 10274–10282 (2014).

42. Zhang, K., Ge, L., Ran, R., Shao, Z. & Liu, S. Synthesis, characterization and evaluation of cation-ordered LnBaCo2O5+δ as materials of oxygen permeation membranes and cathodes of SOFCs. *Acta Mater* **56**, 4876–4889 (2008).

43. Widenmeyer, M. *et al.* Engineering of oxygen pathways for better oxygen permeability in Cr-substituted Ba2In2O5 membranes. *J Memb Sci* **595**, (2020).

44. Sunarso, J., Hashim, S. S., Zhu, N. & Zhou, W. Perovskite oxides applications in high temperature oxygen separation, solid oxide fuel cell and

membrane reactor: A review. *Progress in Energy and Combustion Science* vol. 61 57–77 Preprint at https://doi.org/10.1016/j.pecs.2017.03.003 (2017).

45. Schulze-Küppers, F. *et al.* Design and fabrication of large-sized planar oxygen transport membrane components for direct integration in oxy-combustion processes. *Sep Purif Technol* **220**, 89–101 (2019).

46. Portillo, E., Gallego Fernández, L. M., Vega, F., Alonso-Fariñas, B. & Navarrete, B. Thermodynamic analysis of the integration of an oxygen transport membrane unit into a coal oxy-fired circulating fluidized bed power plant. *J Environ Chem Eng* 105266 (2021) doi:10.1016/j.jece.2021.105266.

47. Kotowicz, J., Job, M. & Brzęczek, M. Thermodynamic analysis and optimization of an oxy-combustion combined cycle power plant based on a membrane reactor equipped with a high-temperature ion transport membrane ITM. *Energy* 117912 (2020) doi:10.1016/j.energy.2020.117912.

48. Zhang, G., Jin, W. & Xu, N. Design and Fabrication of Ceramic Catalytic Membrane Reactors for Green Chemical Engineering Applications. *Engineering* **4**, 848–860 (2018).

49. Wang, H., Cong, Y. & Yang, W. Investigation on the partial oxidation of methane to syngas in a tubular Ba0.5Sr0.5Co0.8Fe0.2O3-δ membrane reactor. in *Catalysis Today* vol. 82 157–166 (2003).

50. Wang, H., Cong, Y. & Yang, W. Oxidative coupling of methane in Ba0.5Sr0.5Co 0.8Fe0.2O3-δ tubular membrane reactors. in *Catalysis Today* vol. 104 160–167 (2005).

51. Garcia-Fayos, J., Lobera, M. P., Balaguer, M. & Serra, J. M. Catalyst screening for oxidative coupling of methane integrated in membrane reactors. *Front Mater* **5**, (2018).

52. Beall, C. E. *et al.* Influence of carbon on the dynamic changes in Co oxidation state of Ba0.5Sr0.5Co0.8Fe0.2O3-δ perovskite catalyst during the oxygen reduction and evolution reactions. *EcoMat* (2023) doi:10.1002/eom2.12353.

53. Cao, Z. *et al.* Simultaneous overcome of the equilibrium limitations in BSCF oxygen-permeable membrane reactors: Water splitting and methane coupling. in *Catalysis Today* vol. 193 2–7 (2012).

54. Schucker, R. C. *et al.* Oxidative Dehydrogenation of Ethane to Ethylene in an Oxygen-Ion-Transport-Membrane Reactor: A Proposed Design for Process Intensification. *Ind Eng Chem Res* **58**, 7989–7997 (2019).

55. Solís, C., Balaguer, M., Garcia-Fayos, J., Palafox, E. & Serra, J. M. Progress in Ce0.8Gd0.2O2-: δprotective layers for improving the CO2stability of Ba0.5Sr0.5Co0.8Fe0.2O3-δO2-transport membranes. *Sustain Energy Fuels* **4**, 3747–3752 (2020).

56. Kwon, Y., Nam, G. D., Lee, G., Choi, S. & Joo, J. H. Recent Progress and Challenges in Mixed Ionic–Electronic Conducting Membranes for Oxygen Separation. *Advanced Energy and Sustainability Research* **3**, 2200086 (2022).

57. Campbell, W. J. & Grain, C. Thermal Expansion of Alpha-Alumina. *Advances in X-ray Analysis* **5**, 244–256 (1961).

58. Wei, B. *et al.* Crystal structure, thermal expansion and electrical conductivity of perovskite oxides BaxSr1-xCo0.8Fe0.2O3- δ (0.3 ≤ x ≤ 0.7). *J Eur Ceram Soc* **26**, 2827–2832 (2006).

59. Herzog, S., Liu, C., Nauels, N., Kaletsch, A. & Broeckmann, C. Failure Mechanisms of Ba0.5Sr0.5Co0.8Fe0.2O3−δ Membranes after Pilot Module Operation. *Membranes (Basel)* **12**, (2022).

60. Pfaff, E. M., Kaletsch, A. & Broeckmann, C. Design of a Mixed Ionic/Electronic Conducting Oxygen Transport Membrane Pilot Module. *Chem Eng Technol* **35**, 455–463 (2012).

61. Nauels, N., Herzog, S., Modigell, M. & Broeckmann, C. Membrane module for pilot scale oxygen production. *J Memb Sci* **574**, 252–261 (2019).

62. Ishihara, T., Miyoshi, S., Furuno, T., Sanguanruang, O. & Matsumoto, H. Mixed conductivity and oxygen permeability of doped Pr2NiO4-based oxide. *Solid State Ion* **177**, 3087–3091 (2006).

63. Klande, T., Efimov, K., Cusenza, S., Becker, K. D. & Feldhoff, A. Effect of doping, microstructure, and CO2 on La 2NiO4+δ-based oxygen-transporting materials. *J Solid State Chem* **184**, 3310–3318 (2011).

64. Sciences, N. Cation Diffusion and Related Degradation Phenomena in La 2 NiO 4 + į for Oxygen Separation Membranes. (2012).

65. Bassat, J. M., Odier, P., Villesuzanne, A., Marin, C. & Pouchard, M. Anisotropic ionic transport properties in La2NiO 4+δ single crystals. *Solid State Ion* **167**, 341–347 (2004).

66. Flura, A. *et al.* Chemical and structural changes in Ln2NiO4+δ (Ln=La, Pr or Nd) lanthanide nickelates as a function of oxygen partial pressure at high temperature. *J Solid State Chem* **228**, 189–198 (2015).

67. Hyodo, J., Tominaga, K., Ju, Y. W., Ida, S. & Ishihara, T. Electrical conductivity and oxygen diffusivity in Cu- and Ga-doped Pr 2NiO4. *Solid State Ionics* vol. 256 5–10 Preprint at https://doi.org/10.1016/j.ssi.2013.12.036 (2014).

68. N. GUNASEKARAN, A. MEENAKSHISUNDARAM, V. S. KINETICS AND MECHANISM OF CO OXIDATION ON Ln:NiO4 OXIDES (Ln = La, Pr or Nd). **22**, 89–98 (1984).

69. Pikalova, E. Y. *et al.* Structure , oxygen transport properties and electrode performance of Ca- substituted Nd 2 NiO 4 ☆. *Solid State Ion* **335**, 53–60 (2019).

70. Świerczek, K., Zhao, H., Zhang, Z. & Du, Z. MIEC-type ceramic membranes for the oxygen separation technology. *E3S Web of Conferences* **108**, 1–9 (2019).

71. Han, N. *et al.* Highly Stable Dual-Phase Membrane Based on Ce 0.9 Gd 0.1 O 2–δ —La 2 NiO 4+δ for Oxygen Permeation under Pure CO 2 Atmosphere. *Energy Technology* **7**, 1–10 (2019).

72. Ishihara, T. Oxide ion conductivity in defect perovskite, Pr2NiO4 and its application for solid oxide fuel cells. *Journal of the Ceramic Society of Japan* **122**, 179–186 (2014).

73. Amow, G. & Skinner, S. J. Recent developments in Ruddlesden-Popper nickelate systems for solid oxide fuel cell cathodes. *Journal of Solid State Electrochemistry* **10**, 538–546 (2006).

74. A. Montenegro-Hernández, L. Mogni, A. C. Validation of Nd 2 NiO 4+δ as Oxygen Electrode Material for Intermediate Temperature Solid Oxide Cells with LSGM Electrolyte. **58**, 183–190 (2013).

75. Han, N., Wei, Q., Zhang, S., Yang, N. & Liu, S. Rational design via tailoring Mo content in La2Ni1-xMoxO4+δ to improve oxygen permeation properties in CO2 atmosphere. *J Alloys Compd* **806**, 153–162 (2019).

76. Ishihara, T., Sirikanda, N., Nakashima, K., Miyoshi, S. & Matsumoto, H. Mixed Oxide Ion and Hole Conductivity in Pr[sub 2−α]Ni[sub 0.76−x]Cu[sub 0.24]Ga[sub x]O[sub 4+δ] Membrane. *J Electrochem Soc* **157**, B141 (2010).

77. Gędziorowski, B. *et al.* Ruddlesden-Popper-type Nd2-xNi1-yCuyO4±δ layered oxides as candidate materials for MIEC-type ceramic membranes. *J Eur Ceram Soc* **40**, 4056–4066 (2020).

78. Garcia-Fayos, J., Balaguer, M. & Serra, J. M. Dual-Phase Oxygen Transport Membranes for Stable Operation in Environments Containing Carbon Dioxide and Sulfur Dioxide. *ChemSusChem* **8**, 4242–4249 (2015).

79. Shi, L. *et al.* High CO2-tolerance oxygen permeation dual-phase membranes Ce0.9Pr0.1O2--Pr0.6Sr0.4Fe0.8Al0.2O3-. *J Alloys Compd* **806**, 500–509 (2019).

80. Luo, H. *et al.* CO2-tolerant oxygen-permeable Fe2O 3-Ce0.9Gd0.1O2-δ dual phase membranes. *Ind Eng Chem Res* **50**, 13508–13517 (2011).

81. Chen, G. *et al.* Novel CO2-tolerant dual-phase Ce0.9Pr0.1O2–δ - La0.5Sr0.5Fe0.9Cu0.1O3–δ membranes with high oxygen permeability. *J Memb Sci* **595**, 117530 (2020).

82. Borik, M. A. *et al.* Structure and conductivity of yttria and scandia-doped zirconia crystals grown by skull melting. *Journal of the American Ceramic Society* **100**, 5536–5547 (2017).

83. Yamamoto, O. Electrical conductivity of stabilized zirconia with ytterbia and scandia. *Solid State Ion* **79**, 137–142 (1995).

84. Kharton, V. V., Marques, F. M. B. & Atkinson, A. Transport properties of solid oxide electrolyte ceramics: A brief review. *Solid State Ion* **174**, 135–149 (2004).

85. Andersson, D. A., Simak, S. I., Skorodumova, N. V, Abrikosov, I. A. & Rje Johansson, B. *Optimization of ionic conductivity in doped ceria*. vol. 103 www.pnas.orgcgidoi10.1073pnas.0509537103 (2006).

86. Omar, S., Wachsman, E. D., Jones, J. L. & Nino, J. C. Crystal structure-ionic conductivity relationships in doped ceria systems. *Journal of the American Ceramic Society* **92**, 2674–2681 (2009).

87. Balaguer, M., Solís, C. & Serra, J. M. Study of the transport properties of the mixed ionic electronic conductor Ce1-xTbxO2-δ + Co (x = 0.1, 0.2) and evaluation as oxygen-transport membrane. *Chemistry of Materials* **23**, 2333–2343 (2011).

88. Balaguer, M., Solís, C., Roitsch, S. & Serra, J. M. Engineering microstructure and redox properties in the mixed conductor Ce0.9Pr0.1O2-δ + Co 2 mol%. *Dalton Transactions* **43**, 4305–4312 (2014).

89. Balaguer, M., Solís, C. & Serra, J. M. Structural-transport properties relationships on Ce 1- xLn xO 2-δ system (Ln = Gd, La, Tb, Pr, Eu, Er, Yb, Nd) and effect of cobalt addition. *Journal of Physical Chemistry C* **116**, 7975–7982 (2012).

90. MAZANEC, T. Electrocatalytic cells for chemical reaction. *Solid State Ion* **53–56**, 111–118 (1992).

91. Ji, Y., Kilner, J. A. & Carolan, M. F. Electrical properties and oxygen diffusion in yttria-stabilised zirconia (YSZ)-La0.8Sr0.2MnO3±δ (LSM) composites. *Solid State Ion* **176**, 937–943 (2005).

92. Fleig, J., Kim, H. R., Jamnik, J. & Maier, J. Oxygen reduction kinetics of Lanthanum Manganite (LSM) model cathodes: Partial pressure dependence and rate-limiting steps. *Fuel Cells* **8**, 330–337 (2008).

93. CARTER, S. Oxygen transport in selected nonstoichiometric perovskite-structure oxides. *Solid State Ion* **53–56**, 597–605 (1992).

94. Balaguer, M., Vert, V. B., Navarrete, L. & Serra, J. M. SOFC composite cathodes based on LSM and co-doped cerias (Ce 0.8Gd 0.1X 0.1O 2-δ, X = Gd, Cr, Mg, Bi, Ce). *J Power Sources* **223**, 214–220 (2013).

95. Jørgensen, M. J. & Mogensen, M. Impedance of Solid Oxide Fuel Cell LSM/YSZ Composite Cathodes. *J Electrochem Soc* **148**, A433 (2001).

96. Navarrete, L., Balaguer, M., Vert, V. B. & Serra, J. M. Tailoring Electrocatalytic Properties of Solid Oxide Fuel Cell Composite Cathodes Based on (La0.8Sr0.2)0.95MnO3+Δ and Doped Cerias Ce1–xLnxO2–Δ (Ln=Gd, La, Er, Pr, Tb and x=0.1–0.2). *Fuel Cells* **17**, 100–107 (2017).

97. Xue, J., Liao, Q., Wei, Y., Li, Z. & Wang, H. A CO2-tolerance oxygen permeable 60Ce0.9Gd0.1O2-δ-40Ba0.5Sr0.5Co0.8Fe0.2O3-δ dual phase membrane. *J Memb Sci* **443**, 124–130 (2013).

98. Luo, H. *et al.* Novel Cobalt-Free, Noble Metal-Free Oxygen-Permeable 40Pr 0.6 Sr 0.4 FeO 3-δ –60Ce 0.9 Pr 0.1 O 2−δ Dual-Phase Membrane. *Chemistry of Materials* **24**, 2148–2154 (2012).

99. Zhu, X., Liu, Y., Cong, Y. & Yang, W. Ce0.85Sm0.15O1.925-Sm0.6Sr0.4Al0.3Fe0.7O3 dual-phase membranes: One-pot synthesis and stability in a CO2 atmosphere. *Solid State Ion* **253**, 57–63 (2013).

100. Xue, J., Liao, Q., Wei, Y., Li, Z. & Wang, H. A CO2-tolerance oxygen permeable 60Ce0.9Gd0.1O2-δ-40Ba0.5Sr0.5Co0.8Fe0.2O3-δ dual phase membrane. *J Memb Sci* **443**, 124–130 (2013).

101. Kiebach, R. *et al.* A review on dual-phase oxygen transport membranes: from fundamentals to commercial deployment. *J Mater Chem A Mater* **10**, 2152–2195 (2022).

102. Balaguer, M., García-Fayos, J., Solís, C. & Serra, J. M. Fast Oxygen Separation Through SO 2 - and CO 2 -Stable Dual-Phase Membrane Based on NiFe 2 O 4 –Ce 0.8 Tb 0.2 O 2-δ. *Chemistry of Materials* **25**, 4986–4993 (2013).

103. García-Fayos, J., Ruhl, R., Navarrete, L., Bouwmeester, H. J. M. & Serra, J. M. Enhancing oxygen permeation through Fe2NiO4-Ce0.8Tb0.2O2-δ composite membranes using porous layers activated with Pr6O11 nanoparticles. *J Mater Chem A Mater* **6**, 1201–1209 (2018).

104. Yi, E.-J., Yoon, M.-Y., Moon, J.-W. & Hwang, H.-J. Fabrication of a MnCo2O4/gadolinia-doped Ceria (GDC) Dual-phase Composite Membrane for Oxygen Separation. *Journal of the Korean Ceramic Society* **47**, 199–204 (2010).

105. Yi, E.-J., Yoon, M.-Y., Moon, J.-W. & Hwang, H.-J. Fabrication of a MnCo 2 O 4 /gadolinia-doped Ceria (GDC) Dual-phase Composite Membrane for Oxygen Separation. *Journal of the Korean Ceramic Society* **47**, 199–204 (2010).

106. Solís, C. *et al.* Mixed Ionic–Electronic Conduction in NiFe 2 O 4 –Ce 0.8 Gd 0.2 O 2− δ Nanocomposite Thin Films for Oxygen Separation. *ChemSusChem* **11**, 2818–2827 (2018).

107. García-Fayos, J., Ruhl, R., Navarrete, L., Bouwmeester, H. J. M. & Serra, J. M. Enhancing oxygen permeation through Fe2NiO4-Ce0.8Tb0.2O2-δ composite membranes using porous layers activated with Pr6O11 nanoparticles. *J Mater Chem A Mater* **6**, 1201–1209 (2018).

108. Zhang, C. *et al.* Oxygen permeation behavior through Ce0.9Gd0.1O2-δ membranes electronically short-circuited by dual-phase Ce0.9Gd0.1O2-δ-Ag decoration. *J Mater Chem A Mater* **3**, 19033–19041 (2015).

109. Zhu, X., Li, Q., He, Y., Cong, Y. & Yang, W. Oxygen permeation and partial oxidation of methane in dual-phase membrane reactors. *J Memb Sci* **360**, 454–460 (2010).

110. Wang, X. *et al.* High oxygen permeation flux of cobalt-free Cu-based ceramic dual-phase membranes. *J Memb Sci* **633**, (2021).

111. Wang, X. *et al.* Co2-tolerant oxygen permeation membranes containing transition metals as sintering aids with high oxygen permeability. *Processes* **9**, (2021).

112. Chen, G. *et al.* A comprehensive comparative study of CO2-resistance and oxygen permeability of 60 wt % Ce0.8M0.2O2–δ (M = La, Pr, Nd, Sm, Gd) - 40 wt % La0.5Sr0.5Fe0.8Cu0.2O3–δ dual-phase membranes. *J Memb Sci* **639**, (2021).

113. Partovi, K., Bittner, M. & Caro, J. Novel CO2-tolerant Al-containing membranes for high-temperature oxygen separation. *J Mater Chem A Mater* **3**, 24008–24015 (2015).

114. He, Y. *et al.* A novel dual phase membrane 40 wt% Nd0.6Sr0.4CoO3-:δ-60 wt% Ce0.9Nd0.1O2-δ: esign, synthesis and properties. *J Mater Chem A Mater* **6**, 84–92 (2017).

115. Pirou, S., García-Fayos, J., Balaguer, M., Kiebach, R. & Serra, J. M. Improving the performance of oxygen transport membranes in simulated oxy-fuel power plant conditions by catalytic surface enhancement. *J Memb Sci* **580**, 307–315 (2019).

116. Lee, Y. A. *et al.* Oxygen permeation and oxidative coupling of methane with NiFe2O4-Gd0.1Ce0.9O2-δ composite membrane. *Ionics (Kiel)* **27**, 1667–1675 (2021).

117. Liang, W., Zhou, H., Caro, J. & Jiang, H. Methane conversion to syngas and hydrogen in a dual phase Ce0.8Sm0.2O2-Δ-Sr2Fe1.5Mo0.5O5+Δ membrane reactor with improved stability. *Int J Hydrogen Energy* **43**, 14478–14485 (2018).

118. Serra, J. M. *et al.* Hydrogen production via microwave-induced water splitting at low temperature. *Nat Energy* **5**, 910–919 (2020).

119. Carrillo, R. J. & Scheffe, J. R. Advances and trends in redox materials for solar thermochemical fuel production. *Solar Energy* **156**, 3–20 (2017).

120. Zoller, S. *et al.* A solar tower fuel plant for the thermochemical production of kerosene from H2O and CO2. *Joule* **6**, 1606–1616 (2022).

121. Schäppi, R. *et al.* Drop-in fuels from sunlight and air. *Nature* **601**, 63–68 (2022).

122. Chueh, W. C. & Haile, S. M. A thermochemical study of ceria: exploiting an old material for new modes of energy conversion and CO2 mitigation. *Philos Trans A Math Phys Eng Sci* **368**, 3269–94 (2010).

123. Chueh, W. *et al.* High-flux solar-driven thermochemical dissociation of CO2 and H2O using nonstoichiometric ceria. *Science (1979)* **330**, 1797–1801 (2010).

124. Patankar, A. S., Wu, X.-Y., Choi, W., Tuller, H. L. & Ghoniem, A. F. A Reactor Train System for Efficient Solar Thermochemical Fuel Production. *J Sol Energy Eng* **144**, (2022).

125. Sun, E. *et al.* Low-temperature carbon dioxide conversion via reverse water-gas shift thermochemical looping with supported iron oxide. *Cell Rep Phys Sci* **4**, 101581 (2023).

126. Otsuka, K., Wang, Y., Sunada, E. & Yamanaka, I. Direct Partial Oxidation of Methane to Synthesis Gas by Cerium Oxide. *J Catal* **175**, 152–160 (1998).

127. Krenzke, P. T., Fosheim, J. R. & Davidson, J. H. Solar fuels via chemical-looping reforming. *Solar Energy* **156**, 48–72 (2017).

128. Hecht, M. *et al.* Mars Oxygen ISRU Experiment (MOXIE). *Space Science Reviews* vol. 217 Preprint at https://doi.org/10.1007/s11214-020-00782-8 (2021).

129. Laguna-Bercero, M. A. Recent advances in high temperature electrolysis using solid oxide fuel cells: A review. *Journal of Power Sources* vol. 203 4–16 Preprint at https://doi.org/10.1016/j.jpowsour.2011.12.019 (2012).

130. Gómez, S. Y. & Hotza, D. Current developments in reversible solid oxide fuel cells. *Renewable and Sustainable Energy Reviews* vol. 61 155–174 Preprint at https://doi.org/10.1016/j.rser.2016.03.005 (2016).

131. Kupecki, J. *et al.* Energy analysis of a 10 kW-class power-to-gas system based on a solid oxide electrolyzer (SOE). *Energy Convers Manag* **199**, (2019).

132. Sreedhar, I., Agarwal, B., Goyal, P. & Agarwal, A. An overview of degradation in solid oxide fuel cells-potential clean power sources. *Journal of Solid State Electrochemistry* vol. 24 1239–1270 Preprint at https://doi.org/10.1007/s10008-020-04584-4 (2020).

133. Lim, C. K., Liu, Q., Zhou, J., Sun, Q. & Chan, S. H. High-temperature electrolysis of synthetic seawater using solid oxide electrolyzer cells. *J Power Sources* **342**, 79–87 (2017).

134. Lenser, C. *et al.* Solid oxide fuel and electrolysis cells. in *Advanced Ceramics for Energy Conversion and Storage* 387–547 (Elsevier, 2019). doi:10.1016/B978-0-08-102726-4.00009-0.

135. Tong, X., Hendriksen, P. V., Hauch, A., Sun, X. & Chen, M. An Up-scalable, Infiltration-Based Approach for Improving the Durability of Ni/YSZ Electrodes for Solid Oxide Cells. *J Electrochem Soc* **167**, 024519 (2020).

136. Liang, M. *et al.* Preparation of NiO-YSZ composite powder by a combustion method and its application for cathode of SOEC. *Int J Hydrogen Energy* **35**, 2852–2857 (2010).

137. Penchini, D., Cinti, G., Discepoli, G. & Desideri, U. Theoretical study and performance evaluation of hydrogen production by 200 W solid oxide electrolyzer stack. *Int J Hydrogen Energy* **39**, 9457–9466 (2014).

138. Vora, S. D. Advances in Solid Oxide Fuel Cell technology at Siemens Westinghouse. *Advanced Materials and Processes* **163**, 54 (2005).

2.

METHODOLOGY

2. Methodology

In this chapter, it will be described all the experimental methodology used during the conduction of this thesis. In the first place, the different procedures for the synthesis of materials and the preparation will be described. Then, it will continue by describing the characterisation techniques, like X-ray diffraction (XRD), surface area BET, scanning electron microscopy (SEM), etc. Finally, the different equipment used in this thesis, like mixed ionic and electric conductors (MIEC) membrane reactors, fixed-bed reactors and oxygen transport electrochemical reactors.

2.1. Material synthesis

Most of the samples and materials were sintered at the laboratory. However, it was also used commercial samples and materials like $Ba_{0.5}Sr_{0.5}Co_{0.8}Fe_{0.2}O_{3-\delta}$ powder and membranes from IKTS (Fraunhofer Institute for Ceramic Technologies and Systems, Germany), $Ce_{0.8}Gd_{0.2}O_{2-\delta}$ powders to sintered electrolytes from Cerpotech (Norway), etc. This section will describe the elaboration processes for the materials and samples in this thesis and which commercial materials were used.

2.1.1. Modified Pechini method

One of the most common methods for synthetizing advanced ceramic materials is the Solid-State Reaction (SSR)[1]. Furthermore, this process is commonly used in industrial processes for producing ceramic materials, thus lowering costs in reactants and lowering contaminant emissions due to the use of oxide materials instead of nitrates or chlorides. Even so, the particle size with this method is higher than with other methods of fabrication, such as the Pechini method or co-precipitation[2,3]. The particle size is fundamental for future sample elaboration, especially in the case of dual-phase materials. In this matter, lowering the particle size usually brings better porous layers for electrodes or catalytic layers in MIEC membranes. Also, lower particle size facilitates the sintering of dense ceramic membranes. Moreover, in the case of dual-phase membranes, higher dispersion of both phases in a dense membrane will bring higher percolative channels for both conductivities, increasing the membrane performance [4].

Pechini method was selected in this thesis for synthetizing all the different ceramic materials[3]. The different steps for the Pechini method are represented in Figure 2. 1. First, the nitrate precursors were mixed in a distilled water solution, and the quantity of the precursors was previously calculated in stoichiometric amounts. This mixture of nitrates was continuously stirred at 60 ºC. Then, citric acid was added to form the complex precursor. A few minutes later, ethylene glycol (from ThermoScientific) was added and then heated up to 80 ºC in agitation. Here, when most of the water is evaporated, this solution is heated up at 220 ºC in a heater overnight. The product is a powder that has to be ball-milled and then calcinated at synthesizing temperature; this temperature depends on the material but should be between 500-1200 ºC.

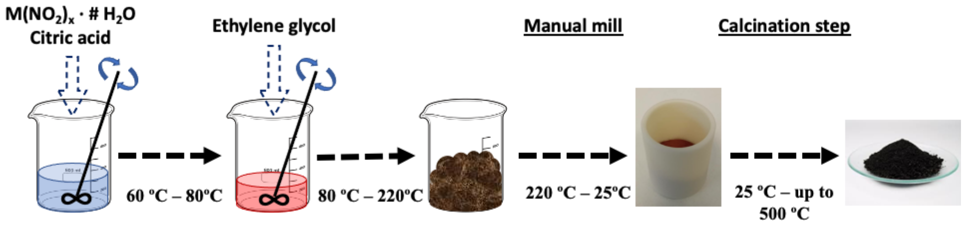

Figure 2. 1. Steps to synthesize ceramic materials by the Pechini method.

Moreover, a physical posttreatment was performed for all the materials elaborated in Figure 2. 2. Here, they had to be milled and sieved to eliminate the agglomerations of particles on the powder and obtain uniform materials. This physical posttreatment consists of milling the powder in a ball mill for 24h. The powder is mixed with zirconia balls in a mass relation of 1:5 (powder: zirconia). Acetone is added to improve the milling. Finally, the powder was dried and sieved below 200 μm particle size.

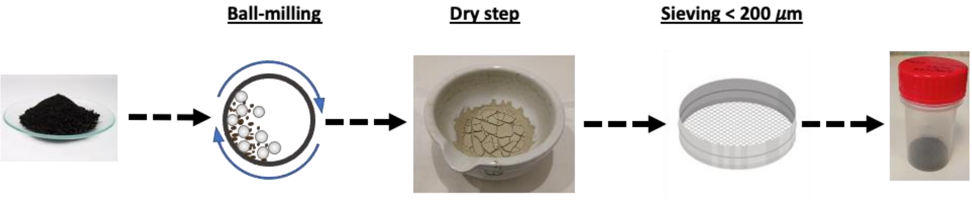

Figure 2. 2. Final mill steps to achieve the final material.

All the powder sintered was analyzed with X-Ray diffraction to verify that the ceramic material was elaborated without impurities or other phases not desired. This characterization technique will be explained in a later section.

2.2. Sample preparation

Different samples were elaborated depending on their final use. Most of these materials can be used as MIEC membranes, electrolytes, electrodes and/or as a catalytic layer. Those materials can be separated into two types of samples: dense samples (MIEC membranes and electrolytes) and porous layers (electrodes and catalytic layers). However, the specific steps and conditions for the sample preparation will be explained in more detail in each corresponding chapter.

2.2.1. Dense samples (MIEC membranes and electrolytes)

As mentioned, dense samples were used as electrolytes, MIEC membranes, or dense bars (to measure total conductivity). The characteristics of both are different, and they are used in other technologies, but they have something in common: they must be completely dense without percolative channels to the gas phases (some occlusive porosity could be accepted). The elaboration of these samples involves the uniaxial pressing and the sintering at high temperatures to obtain dense materials, around 900-1500 °C. Figure 2. 3 represents the diagram for the preparation of dense samples.

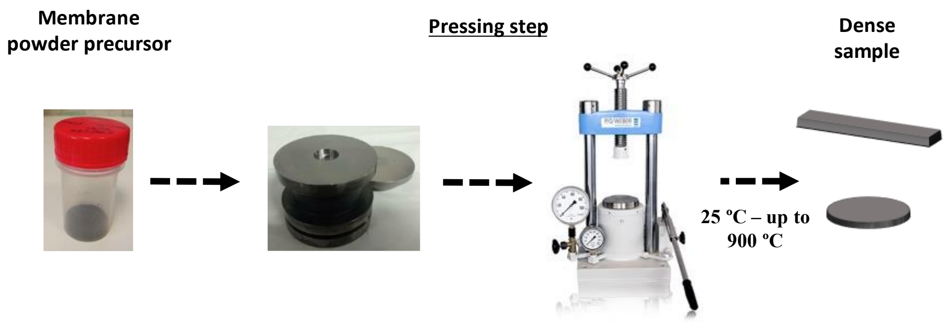

Figure 2. 3. Steps followed in the preparation of dense ceramic samples.

First, for MIEC membranes and electrolytes, homogeneous powder is added to a die with a cylindrical diameter of 26 mm. This powder was distributed carefully inside the die and pressed at 56 MPa for 3 min. Finally, the pellet formed was calcinated to high temperature in order to be sintered, around 1300-1500 °C during 5-10 h. For dense bars, a different die with a rectangular form (0.4x1.2 cm^2) was used.

In some materials, it is necessary to add a polymer to improve the pressing step. This polymer gives some plasticity to the green pellets. The polymer used was the polyvinyl alcohol (PVA), fully hydrolyzed, from Sigma-Aldrich. The addition of PVA to the powder is described in Figure 2. 4. Here, the PVA is added into distillate water agitated at 60 °C, adding 7.5 mg of PVA for each gram of material future added. When the PVA was completely dissolved, it was dropped into the powder and heated up to 80 °C. When the powder was completely dry, the powder was ball-milled and sieved down to 200 µm of particle size. Finally, the sample can be elaborated with the previous process, Figure 2. 3.

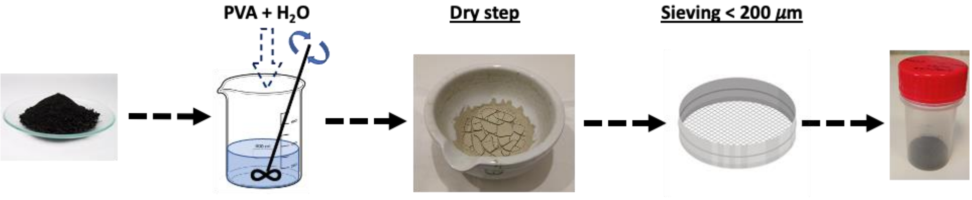

Figure 2. 4. Plastic aid addition in the precursor powder to facilitate the pressing step.

The dimensions of the elaborated dense membranes had to be adjusted for the lab-scale reactors, depending on their future use. This reduction of the dimensions was carried out by grilling the different parts of the membrane with sandpaper. The membrane diameter should be adjusted closer to 15 mm. However, the thickness depends on future use, being around 600 μm for MIEC membranes and 1 mm for the electrolytes.

2.2.2. Porous layers (Electrodes and catalytic layers)

Once dense membranes and electrolytes are prepared, porous layers (catalytic layers or electrodes) can be deposited. Here, the last part of the sample's preparation will be described: the deposition of porous layers. As was explained in the introduction, these porous layers will play an important role in the membrane performance. So, the layer microstructure and the proper adhesion to the dense material surface are crucial. In this matter, the final porous layer has to be well attached to the membrane, with a thickness between 15-40 μm [5–7]. The microstructure of these layers was observed with SEM microscopy.

The screen-printing technique was used to add the porous layer to the dense membrane. The first step is to prepare the ink that contains the precursor of the porous layer, Figure 2. 5. The viscosity of the total ink and the quantity of material per gram of ink are determinants to control the layer thickness. Two different vehicles were used to prepare the inks: Terpineol with 6% cellulose and ZVAR ((2-

metoximetiletoxi) propanol). Also, the ratio 1:1 of powder and the carrier normally was used. In the case of using terpineol, for the ink elaboration, it is necessary to heat it first at 60ºC in agitation to decrease its viscosity. The scheme for the ink preparation is represented in Figure 2. 5. Here, the elaboration starts with the mass measurement for the ceramic powder. Then, the vehicle is added to the same quantity, and the mixture is mixed on a three-roll mill.

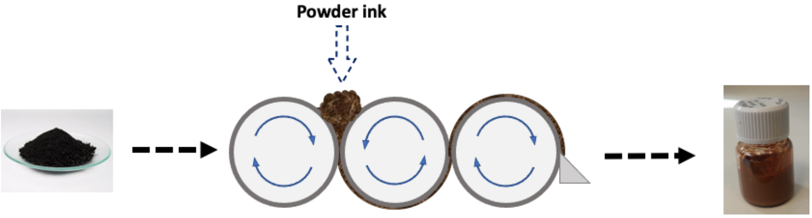

Figure 2. 5. Elaboration of inks by a tricylindrical roll.

To add the layer to the dense membrane, the screen-printing technique was used, described in Figure 2. 6. The ink was settled on the screen and printed on the dense material, with a diameter of 9 mm. For our ink composition, each step of screen-printing will result in a 15 µm thick porous layer (after sintering), being necessary for 2 print steps. Then, the membranes were sintered at around 900-1200 ºC for 2h.

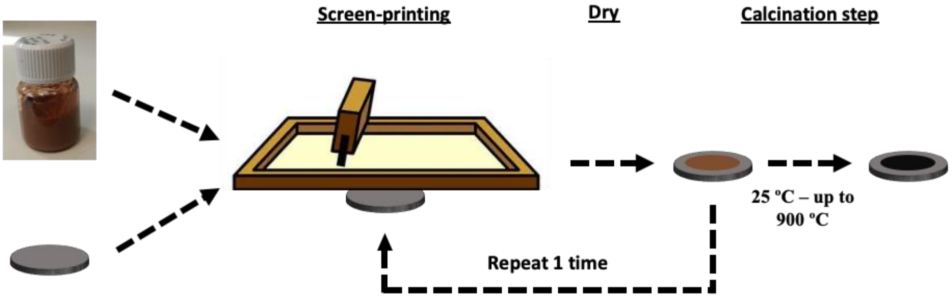

Figure 2. 6. Electrodes and catalytic layer deposition by screen-printing and subsequent calcination.

If the porous layer is going to be used as an electrode, adding the porous layer is not the last step. Namely, a gold mesh is normally added to improve the connection between the electrode and the current collector. For this part, the gold ink was prepared the same way described before. In this case, the deposition is done with a thin paintbrush, drawing a grid. Then, the gold mesh is dried at 80 ºC. Finally, the gold mess was sintered at 900 ºC for 2 h.

2.3. Material characterization

2.3.1. X-ray diffraction technique.

The first and fundamental characterization is the X-ray diffraction (XRD) technique. This technique makes it possible to identify the crystal structure or the different crystalline structures in a sample. All the materials in this thesis present different crystal structures (i.e., fluorite, perovskite…). Also, many of these materials were made in the laboratory and confirming their crystal structure without impurities is essential. In addition, several studies were involved with dual-phase materials, and in these materials, it is important to identify and quantify both phases.

Any material with a crystal structure has a characteristic X-ray diffraction pattern. A monochromatic X-ray beam of wavelength λ with a determinate angle (2θ) crashes on a crystal material. The X-rays are diffracted only when the distance with the successive planes have X-ray diffractions with different complete numbers of wavelengths (Bragg's law, Eq. 2. 1), Figure 2. 7a. Depending on the angle (2θ) at which these diffractions occur, the X-ray diffraction pattern will be determined, Figure 2. 7b.

$$n \cdot \lambda = 2 \cdot d \cdot sen\,(\theta) \qquad \text{Eq. 2. 1}$$

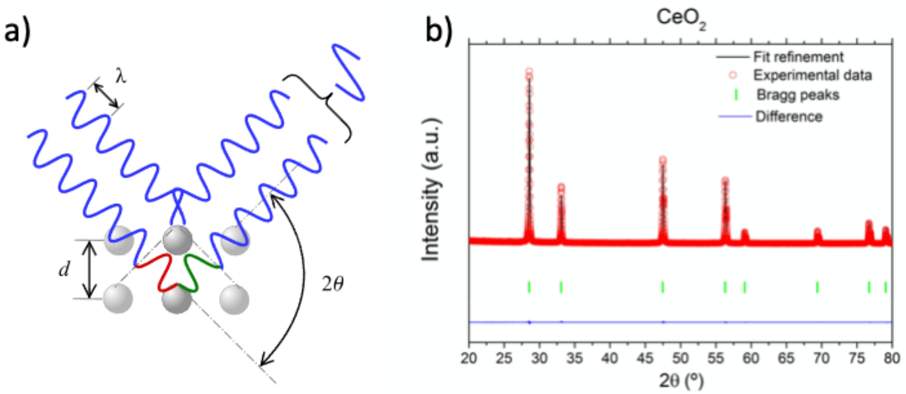

Figure 2. 7. a) X-ray diffraction and Bragg's law; **b)** X-ray diffraction pattern and Rietveld refinement for commercial CeO_2 (Sigma Aldrich).

A PANalytical Cubix fast diffractometer was used for all the XRD in this thesis, using CuKα1 radiation (λ = 1.5406 Å) and an X'Celerator detector in Bragg−Brentano geometry. XRD patterns were recorded in the 2θ range of 20° to 80° and were analyzed using the software X'Pert Highscore Plus software. Rietveld refinement was conducted to obtain the cell parameter for some materials considered in this thesis, using patterns for the bibliography named with their ICSD code to identify.

2.3.2. Scanning Electron Microscopy

To characterize the final micro and macro structures and the topography of the samples, high-resolution scanning electron microscopy (SEM) technology was used. For the materials and the samples used, the microstructure is the determinant of the performance. In the case of the membranes or electrolytes, 100% selectivity for oxygen separation is achieved for completely dense membranes, and some occlusive porosity could be admitted. With dense membranes, only the oxygen flows through the membrane, taking advantage of the ionic conductivity of the membrane (oxygen vacancies or interstitial oxygen). Also, the thickness determines the final performance of the membrane, following the Wagner equation explained in the last chapter. Moreover, in the case of the dual-phase membranes, both phases had to be well dispersed with percolative channels on both sides of the membrane to ensure both conductivities without restrictions.

As mentioned in the last section, the micro structural analysis on porous layers (electrodes or catalytic layers) was essential, checking the thickness and the attachment on the membrane. In addition, in the case of the dual-phase electrodes (or catalytic layers), both phases will be well dispersed to ensure the three-phase boundaries (TPBs). These TPBs are essential in the surface exchange reactions, as explained in the past chapter.

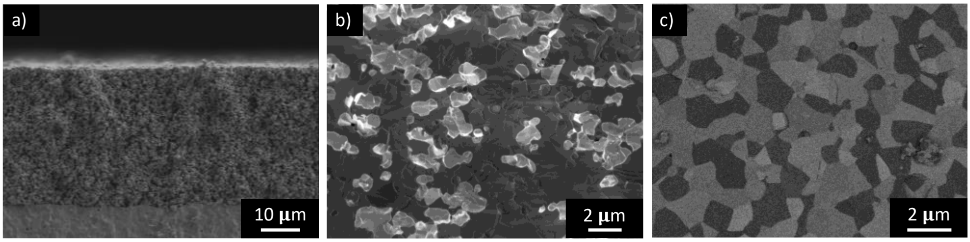

Figure 2. 8. Scanning electron microscopy (SEM) images for different samples and with different detectors: **a)** SED; **b)** InLenss detector; **c)** BSD

In Figure 2. 8, images are represented with the three detectors to characterize the different aspects. Figure 2. 8a shows a transversal image for a catalytic layer on an OTM measured with the secondary electron detector (SED). With this detector, it is possible to characterize the porous structure of this catalytic layer. The resistance will increase with decreasing layer porosities, worsening the overall membrane operation. The image in Figure 2. 8b was taken for a dual-phase membrane with the InLens detector. With this detector, it is possible to see the surface topography, and if the conductivities are very different, it is possible to see the dispersion of both phases. The last SEM detector used in this thesis is the backscattered electron detector (BSD). This detector has a poor resolution for the microstructure, but it provides different grey tones for different materials with different mass weights, Figure 2. 8c.

To reproduce the images, SEM equipment uses an incident high-energy electron (1.5-20 eV) that energy is produced by a heated tungsten filament. These electron collisions cause a secondary emission from the sample and, with the detector, is translated to images from your sample.

2.3.3. Surface area BET

For the powder samples used in fixed bed reactor, the specific surface area is an important property to take into account because, normally, the active sites are on the surface. For these samples, the specific surface area was measured using a Micromeritics ASAP 2420 (Surface Area Porosity Analyzer) applying the BET method. The powders were pressed in a pellet, crushed and sieved between 400-600 µm. Then, the sample was degasified at 250 °C for 24 h using a vacuum, with a 10 $°C\cdot min^{-1}$ heating rate. The adsorption and desorption of N_2 to obtain the BET surface area was at a temperature of -196.15 °C.

2.3.4. Total conductivity

The total conductivity was measured with a standard 4-point DC technique at different temperatures in air, ***Figure 2. 9***. These measurements were taken with dense samples in bars form, as explained in section 2.2.1. Also, these bars are painted with silver ink to perform the different contacts. Furthermore, 1mm thick silver wires were tied at each contact.

To measure the conductivity, it applied an electrical current with external contacts, whereas the potential (voltage) is measured between the contacts. With these two measures, it is possible to calculate the resistance with Ohm`s law for each sample, Eq. 2. 2:

$$R = I \cdot \Delta V \qquad \text{Eq. 2. 2}$$

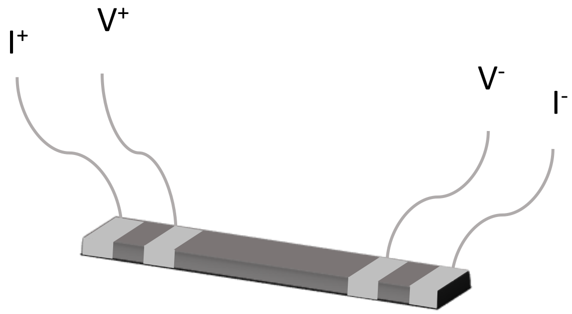

Figure 2. 9. Dense sample bar and the connections for total conductivity measurements.

Then, it was calculating the total conductivity with the resistance and the dimensions of the sample:

$$s = \frac{L}{(a \cdot b)R} \qquad \text{Eq. 2. 3}$$

Where, L is the distance between V^+ and V^- and a and b are the bar width and height, respectively.

The measure of each point of total conductivity is extracted for a slope of several I-V points with a small range of current applied. It was used a Keithley 2601 to supply the current and a Keithley 3706 to analyze the voltages.

2.4. Lab scale reactors

In this section, common lab-scale reactors, like fixed-bed reactors, OTM reactors, and electrochemical membrane reactors, were described and explained. However, another reactor was used in the present thesis, which will be described in their specific chapter.

2.4.1. Fixed-bed reactors

The fixed-bed reactor is used for several reactions and is a very common reactor. This thesis used the fixed-bed reactor in Chapter 6 (Chemical looping methane reforming). The diagram of the fixed-bed reactor and the experimental device is represented in Figure 2. 10.

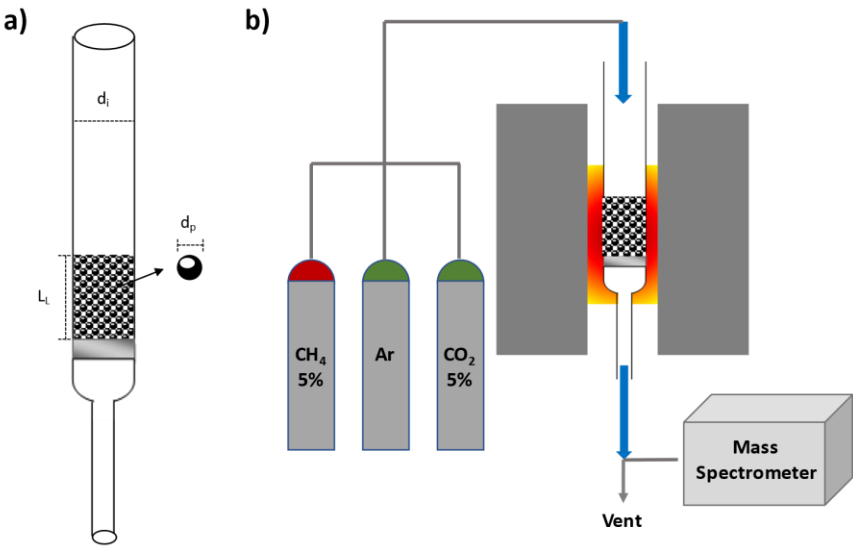

Figure 2. 10. a) Fixed-bed reactor diagram**; b)** Experimental device diagram for the experiments in a fixed-bed reactor.

For a fixed-bed reactor, a homogeneous flux through the catalyst is a very important factor. In order to prevent preferential flux channels, we must control 3 factors (Figure 2. 10a): internal reactor diameter (d_i), particle size diameter (d_p) and the heigh of the fixed-bed reactor (L_L). Therefore, the good diffusion flux across the fixed bed must obey these equations:

$$L_L/d_p > 100 \qquad \text{Eq. 2. 4}$$

$$d_i/d_p > 10 \qquad \text{Eq. 2. 5}$$

These equations are correlated to the Thiele module, which must be less than 0.4. For our reactor, the d_i is 0.9 cm, and for a d_p is 200 µm. The L of the 250 mg of powder was 1 cm. The results for the equation Eq. 2. 4 are 50, and for Eq. 2. 5 is 45. We are in the middle. But if the flow is laminar (Reynolds module less than 2000), then it won't be flow problems:

$$Re = \frac{\rho_{Ar} v_c d_p}{\mu_{Ar}} \qquad \text{Eq. 2. 6}$$

Where Re is the Reynolds number, ρ_{Ar} is the argon density, v_c is the crossing velocity, and μ_{Ar} is the argon viscosity. To calculate the Reynolds number, the properties of the Ar were chosen because it is at least 95% of the concentration of the total flow for the chemical looping test. The crossing velocity comes from the velocity of the fluid between the catalyst and the total volume of the fixed bed:

$$v_c = \frac{Q_T}{S_{gas}} \qquad \text{Eq. 2. 7}$$

Where Q_T is the total flow (100 mL·min^{-1} for chemical looping tests) and S_{gas} is the cross-section for the gas phase on the fixed-bed reactor. This S_{gas} can be calculated:

$$S_{gas} = \frac{V_{fixed-bed} - V_{solid}}{L_L} \qquad \text{Eq. 2. 8}$$

Where $V_{fixed\text{-}bed}$ is the total volume of fixed-bed, and V_{solid} is the total volume of the catalyst. The V_{solid} can be calculated as:

$$V_{solid} = \frac{m_{solid}}{\rho_{theo}} \qquad \text{Eq. 2. 9}$$

Where, m_{solid} is the quantity of catalyst for each experiment (250 mg for chemical looping tests) and ρ_{theo} is the theoretical density for the catalyst calculated by Rietveld refinement. It was assumed 7 g·cm^{-2} for these calculations thus the values for ρ_{theo} oscillate between 7.27 to 6.97 g·cm^{-2}.

The Reynolds number for our experiments in the fixed-bed reactor is around 450, so it is assumed that we have laminar flow.

Figure 2. 10b represents the experimental device for the chemical looping methane reforming test. It was 3 mass flow controllers for each atmosphere. The fixed-bed reactor was inside a cylindrical furnace. The gas flows go across the reactor from the top to the bottom. Then, the part of the product gas goes to a mass spectrometer to analyze, and the other goes to the heart.

2.4.2. MIEC membrane reactors

Another important reactor used in the present thesis is the OTM reactor. In order to measure new or modified MIEC membranes, we have a quartz reactor prepared for this kind of measurement.

This reactor has two principal parts (Figure 2. 11): The sweep chamber, where the sweep gas will move the products to the analyzer and the exhaust, and the feed chamber, where the membrane extracts the oxygen. For both, the more important part of this reactor is the feed chamber, where the membrane is sealed.

Figure 2. 11 a represents the scheme for the MIEC membrane reactor. Metal alloy rings were used to seal the membrane to the reactor. Figure 2. 11b gives a closer look at both sides of the membrane. Depending on the metal alloy used, the seal temperature could oscillate around 850-960 ºC on sealing temperature. From the top, the feed chamber has the injection from oxidant atmosphere (Air or mix of Ar and O_2) inside a quartz tube. For the outside goes the exhaust of this oxidant flow.

From the bottom comes the sweep gas, normally Ar, but in some cases, the sweep gas is CO_2, which is more interesting for the industry. The sweep gas with the O_2 permeate was analyzed at steady state by online gas chromatography using a micro-GC Varian CP-4900 equipped with Molsieve5A, Pora-Plot-Q glass capillary, and CP-Sil modules. Membrane gas leak-free conditions were ensured by continuously monitoring the N_2 concentration in the product gas stream.

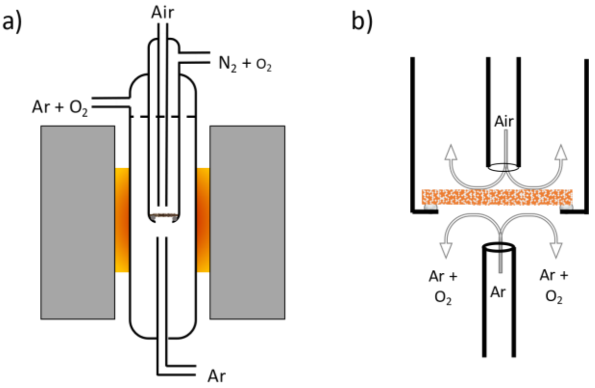

Figure 2. 11. a) MIEC membrane reactor lab scale; **b)** Zoom from membrane reactor chambers.

2.4.3. Electrochemical reactors

Electrochemical impedance spectroscopy is a technique that can study the limiting processes (surface exchange reactions, absorption of oxygen, gas diffusion) for solid electrodes.

For these electrochemical studies, it was used an electrochemical reactor developed in our lab; this reactor is to be able to make electrochemical impedance spectroscopy (EIS) measurements closer to actual operation conditions, Figure 2. 12.

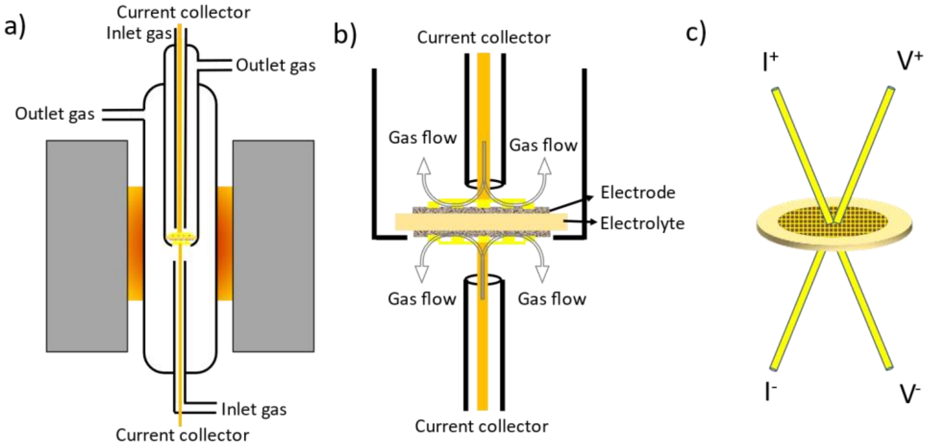

Figure 2. 12. a) Experimental device for the EIS studies; **b)** Scheme of the position of the sample inside the electrochemical reactor; **c)** Scheme of the position of the current collectors on the sample.

The EIS impedance can be correlated with Ohm's law:

$$E = I \cdot Z \qquad \text{Eq. 2. 10}$$

Where the voltage (*E*) is a function of the current (*I*) and the impedance (*Z*). This voltage excitation is applied with a sinusoidal signal (alternating current, AC):

$$E_t = E_0 \sin{(\omega \cdot t)} \qquad \text{Eq. 2. 11}$$

Where, the voltage (E_t) is function of the amplitude (E_0) of this voltage and with the frequency is applicated (ω). For linear systems, the current also has a sinusoidal response with the phase shifted (φ):

$$I_t = I_0 \sin{(\omega \cdot t + j)} \qquad \text{Eq. 2. 12}$$

Then, the EIS impedance will be written like:

$$Z = Z_0 \frac{\sin{(\omega \cdot t)}}{\sin{(\omega \cdot t + \varphi)}} \qquad \text{Eq. 2. 13}$$

Where, Z_0 is the quotient of voltage and current amplitude (E_0/I_0). Then, it is possible to express the impedance as an equation with real and imaginary parts:

$$Z(\omega) = Z_0 e^{i \cdot \varphi} = Z_0 e^{\cos\varphi + i \cdot \sin\varphi} \qquad \text{Eq. 2. 14}$$

Then, the measurements of the impedance in the imaginary (Z') and real (Z") part can be represented like a Nyquist diagram (example in Figure 2. 13a). Also, for EIS measures, the bode diagram is illustrated, imaginary art of the impedance as a function of the frequency. This will identify at what frequency resistances are obtained (example in Figure 2. 13b).

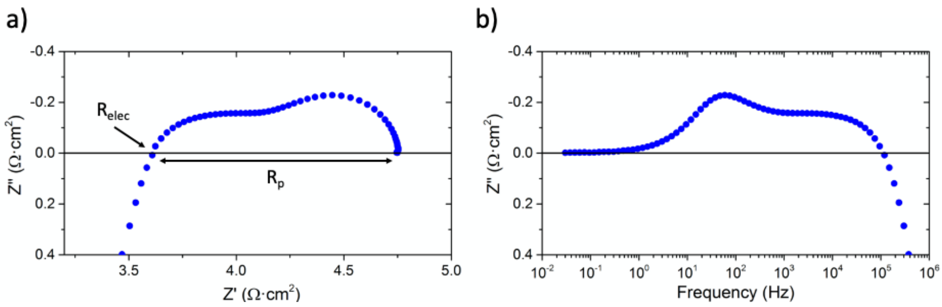

Figure 2. 13. EIS example for an electrode in air at 700ºC. **a)** Nyquist diagram (R_{elec}= electrolyte resistance and R_p= polarization resistance); **b)** bode diagram.

With these measures, it is possible to analyze the limiting steps on the surface exchange reactions on an electrode at different temperatures and pO_2 atmospheres. The first part is to analyze all the information it is possible to get for each measurement and then see how these liming steps on the surface exchange reactions and see how they change at different conditions.

Normally, the first part to analyze in a Nyquist diagram for an EIS measurement is the polarization resistance (R_p). R_p is the resistance for all the steps involved in the surface exchange reactions (R_1 + R_2, Figure 2. 14a). Also, this diagram provides information on the electrolyte resistance (Z' when Z" is 0, R_{elec}). Other information can be extracted from the Bode diagram (Figure 2. 13b), like at which frequency these limiting steps appear. For example, mid frequencies are related to the surface exchange reactions and the low frequencies are related to the oxygen diffusion.

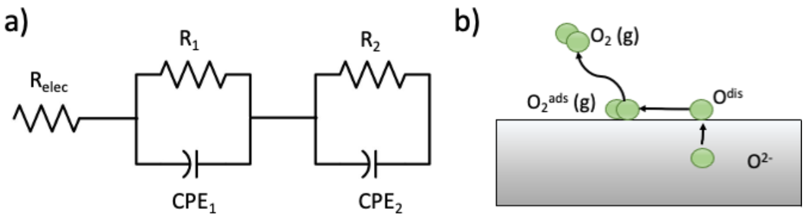

Figure 2. 14. a) Equivalent circuit for reference electrode in air at 700 ºC; **b)** Different steps in surface exchange reactions for MIEC materials.

The resistance for the distinct contributions' changes with the pO_2 following a power law (Eq. 2. 15), where the exponent is characteristic of the controlling surface-exchange step:

$$R_i \sim pO_2^{-n} \qquad \text{Eq. 2. 15}$$

$$O_2(g) \leftrightarrow O_{2\,ads} \qquad n=1 \qquad \text{Eq. 2. 16}$$

$$O_{2\,ads} \leftrightarrow 2\,O_{ads} \qquad n=1/2 \qquad \text{Eq. 2. 17}$$

$$O_{ads} + 2e^- + V_o^{\cdot\cdot} \leftrightarrow O_o^x \qquad n=1/4 \qquad \text{Eq. 2. 18}$$

The samples in this thesis (symmetrical cells) were analyzed by 2-4 point configuration, Figure 2. 12c, in a Solartron 1470E and 1455A FRA module equipment. The input signal was a 20 mV AC amplitude signal with frequencies between 0.03 to $1 \cdot 10^6$ Hz. Additionally, the software of ZviewTM 2 was used to analyze and fit the electrodes to equivalent circuits and obtain all the parameters at different conditions.

2.5. References.

1. Petric, A. & Ling, H. Electrical conductivity and thermal expansion of spinels at elevated temperatures. *Journal of the American Ceramic Society* **90**, 1515–1520 (2007).

2. Tianshu, Z. Ionic conductivity in the CeO2–Gd2O3 system (0.05≤Gd/Ce≤0.4) prepared by oxalate coprecipitation. *Solid State Ion* **148**, 567–573 (2002).

3. Danks, A. E., Hall, S. R. & Schnepp, Z. The evolution of 'sol-gel' chemistry as a technique for materials synthesis. *Mater Horiz* **3**, 91–112 (2016).

4. Kiebach, R. *et al.* A review on dual-phase oxygen transport membranes: from fundamentals to commercial deployment. *J Mater Chem A Mater* **10**, 2152–2195 (2022).

5. Catalán-Martínez, D., Santafé-Moros, A., Gozálvez-Zafrilla, J. M., García-Fayos, J. & Serra, J. M. Characterization of oxygen transport phenomena on BSCF membranes assisted by fluid dynamic simulations including surface exchange. *Chemical Engineering Journal* **387**, (2020).

6. Baumann, S. *et al.* Ultrahigh oxygen permeation flux through supported Ba0.5Sr0.5Co0.8Fe0.2O3-δ membranes. *J Memb Sci* **377**, 198–205 (2011).

7. Hong, W. K. & Choi, G. M. Oxygen permeation of BSCF membrane with varying thickness and surface coating. *J Memb Sci* **346**, 353–360 (2010).

3.

OPTIMIZATION OF DUAL-PHASE ELECTRODES FOR HIGH-TEMPERATURE MEMBRANE REACTORS

3. Optimization of dual-phase electrodes for high-temperature membrane reactors

3.1. Introduction

Integration of carbon capture and storage (CCS) approaches in combustion processes has become one of the most challenging goals of this decade. CCS is of particular interest in the combustion chambers in industrial processes. Capture processes are generally implemented after combustion or directly with oxy-combustion methods, injecting pure O_2 instead of air. The advantages of oxy-combustion regarding traditional combustion include a higher efficiency of fuel utilization than the combustion with air [1]. In addition, the product of the oxy-combustion is CO_2 and H_2O, which are easily separated and stored.

Oxygen Transport Membranes (OTMs) technology provides pure oxygen more efficiently for different operation ranges than traditional methods like cryogenic air distillation [1–3]. OTMs are promising candidates for applications in oxygen supply, CO_2 capture, or catalytic membrane reactors [4–6]. As it was mentioned in Chapter 1, oxygen flux rates viable for industrial application for these membranes should reach an oxygen permeation flux of around 10 $mL\cdot min^{-1}\cdot cm^{-2}$ or, in the case of OTM reactors, ~ 5 $mL\cdot min^{-1}\cdot cm^{-2}$ [7,8]. OTMs typically consist of mixed ionic-electronic conductors (MIECs) that transport O^{2-} and electronic carriers at high temperatures (1000-700 ºC). Generally, perovskite materials with structure (ABO_3) are used [9]. Up to now, the state of the art in MIEC membrane material is $Ba_{0.5}Sr_{0.5}Co_{0.8}Fe_{0.2}O_{3-\delta}$ (BSCF), while the substitution of Fe by Cu has demonstrated an improvement in the oxygen permeability due to the catalytic effect of segregated particles made of copper oxide phases [10]. Still, perovskites containing alkaline earth elements in the A-site are generally prone to decompose at low pO_2 and in the presence of CO_2 and SO_2 [11]. In particular, upon exposure to CO_2, alkaline carbonates are formed with the consequent performance degradation. Several groups have studied the rational doping in the A-site and B-site to improve the stability of these perovskites, but long-term stability in CO_2 and SO_2-containing atmospheres remains challenging [4,9].

On the other hand, some materials with only electronic or ionic conductivity are stable in CO_2-containing atmospheres, like metallic oxides and lanthanide oxides with spinel or fluorite structures [12,13]. The mix of those materials provides a dual-phase or composite material with MIEC properties. Dual-phase membranes generally have lower permeation than pure MIEC membranes but higher stability under different atmospheres [14–16]. For composite materials, the optimal ratio and composition of each phase are highly dependent on the individual material properties essential to having good percolation of both phases and not compromising oxygen permeation [17]. Normally, one of the phases is a pure ionic material such as Gadolinium-doped Ceria (CGO), Yttria-stabilized Zirconia (YSZ), or Scandia-stabilized Zirconia (ScSZ). There are three types of dual-phase materials, depending on the nature of the electronic phase, which can be: i) a pure metallic material like Pd, Ag, or Cu [18–21], ii) a MIEC material like $La_{0.5}Sr_{0.5}Fe_{0.8}Co_{0.2}O_{3-\delta}$ (LSFC), $Ba_{0.5}Sr_{0.5}Co_{0.8}Fe_{0.2}O_{3-\delta}$ (BSCF) [13,14,22,23], and iii) metallic oxides with only electronic conductivity like $NiFe_2O_4$ (NFO), $CoMn_2O_4$ (CMO) or $La_{0.5}Sr_{0.5}MnO_3$ (LSM) [24–26]. In previous works, composites based on $NiFe_2O_4/Ce_{0.8}Tb_{0.2}O_{2-\delta}$ (NFO-CTO) were characterized as OTMs under reducing atmospheres and in the presence of CO_2 and SO_2. The stability of NFO-CTO was excellent under those harsh atmospheres [27–29].

In this chapter, we studied the properties of the dual-phase material NFO-CTO as a catalytic layer. The electrochemical impedance study of the different ratios (x%

NFO – (100-x)% CTO) as electrodes revealed the relevance of the surface ionic transport. Then, the influence of the surface exchange on the oxygen permeation of a 50% NFO-50% CTO membrane was studied by varying the NFO-CTO ratio in the catalytic layers. A correlation of both techniques allowed us to characterize the reaction mechanism better and optimize the ratio by improving the surface exchange reactions of these composite catalytic layers.

3.2. Sample preparation and characterization

$NiFe_2O_4$ (NFO) and $Ce_{0.8}Tb_{0.2}O_{2-\delta}$ (CTO) ceramic powders were synthesized to fabricate membranes, porous catalytic layers for oxygen permeation studies, and porous electrodes for EIS studies. One pot Pechini method was used to prepare the dual-phase materials. The stoichiometric amount of $Ce(NO_3)_3{\cdot}6H_2O$, and $Fe(NO_3)_3{\cdot}9H_2O$ provided by Sigma Aldrich, and $Tb(NO_3)_3{\cdot}6H_2O$ and $Ni(NO_3)_3{\cdot}6H_2O$ from ABCR were mixed in a homogeneous solution. The precursors were calcined at 750 °C for 5 h, to form the desired spinel and fluorite phases. Five different composite formulations were prepared by varying spinel and fluorite content, Table 3. 1.

Table 3. 1. Dual-phase membrane compositions: dual-phase catalytic layer ratios.

Dual-phase composition	**Acronym**
20%Fe_2NiO_4-80%$Ce_{0.8}Tb_{0.2}O_{2-\delta}$	20NFO80CTO
40%Fe_2NiO_4-60%$Ce_{0.8}Tb_{0.,2}O_{2-\delta}$	40NFO60CTO
50%Fe_2NiO_4-50%$Ce_{0.8}Tb_{0.2}O_{2-\delta}$	50NFO50CTO
60%Fe_2NiO_4-40%$Ce_{0.8}Tb_{0.2}O_{2-\delta}$	60NFO40CTO
80%Fe_2NiO_4-20%$Ce_{0.8}Tb_{0.2}O_{2-\delta}$	80NFO20CTO
Without catalytic layer	No layer

For EIS studies, $Ce_{0.8}Gd_{0.2}O_{2-\delta}$ (CGO82) electrolyte disks of 26 mm diameter were sintered at 1450 ºC for 10 h. The screen-printed membranes or electrolytes were then sintered at 1100 ºC for 2 h. To determine the influence of the composition of the porous layers in the O_2 permeation, the 50NFO50CTO composition was selected for the membranes. Dense specimens were obtained at 1400 °C for 10 h. Porous layers (~ 30 μm) of different ratio NFO-CTO composites were screen-printed following the same procedure as for the EIS studies.

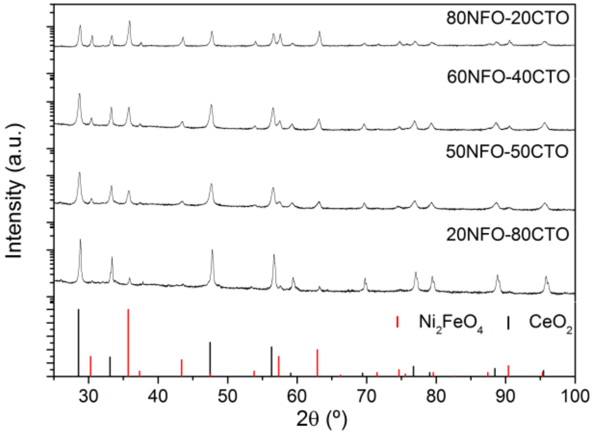

Figure 3. 1. XRD patterns of the NFO-CTO dual-phase powder materials series as synthesized at 750 °C for 5 h.

The XRD patterns for the different dual-phase materials are shown in Figure 3. 1 for 20NFO80CTO, 40NFO60CTO, 50NFO50CTO, 60NFO40CTO, and 80NFO20CTO. Reference patterns of the single spinel (NFO, CIF code 28108) electronic phase (EP) and the fluorite (CeO_2, CIF code 55284) ionic phase (IP) are also provided for comparison. The XRD for the CTO has a displacement to the right with respect to the undoped CeO_2 since Tb^{+4} has a lower ionic radius and, thus, a shorter cell parameter than the pure CeO_2 (Table 3. 2). Otherwise, NFO shows no displacement, indicating that none of the other elements are incorporated in the lattice, confirming the compatibility of these two materials in a composite. Besides, the dual-phase powders sintered at 750 ºC for 5 h by the one-pot Pechini method showed no secondary phases or impurities. Separately, samples of each dual-phase composition were calcinated at 1100 ºC for 2 h, the same treatment as the addition of the catalytic layers. The Rietveld refinement of these samples (Figure 3. 2 and Figure 3. 3) confirms the ratios for the dual-phase catalytic layers, reported in Table 3. 2.

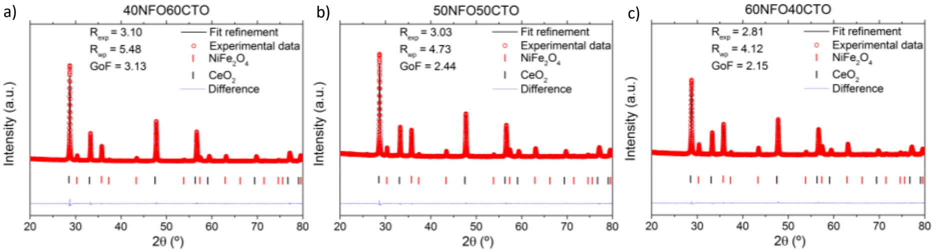

Figure 3. 2. Rietveld refinement for the samples treated at 1100 ºC for 2 h**: a) 40NFO60CTO; b) 50NFO50CTO; c) 60NFO40CTO.**

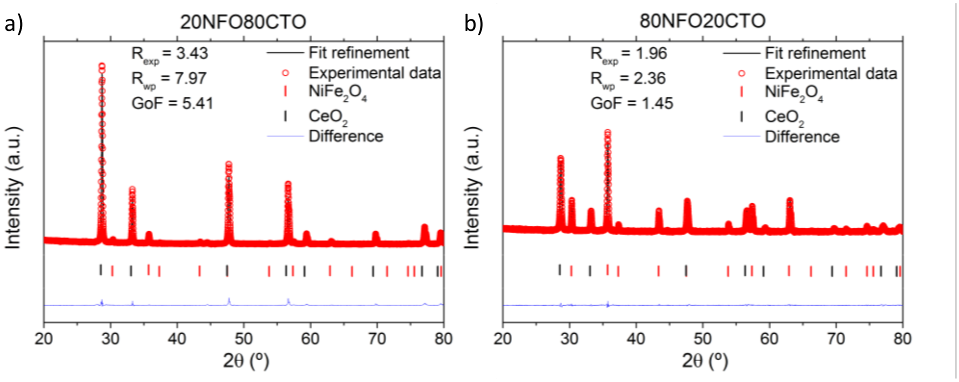

Figure 3. 3. Rietveld refinement for the samples treated at 1100 ºC for 2 h: **a) 20NFO80CTO; b) 80NFO20CTO.**

An essential aspect of dual-phase materials is their distribution along the membrane or the catalytic layer. Both phases must form percolative channels to achieve good ionic and electronic transport. In addition, dual-phase catalytic layers should have both phases well distributed and with high porosity, adequate for gas diffusion. SEM cross-section images shown in Figure 3. 4 allowed us to measure the thickness of the catalytic layer, which was between 25-35 μm for all the samples. Figure 3. 5 shows the dual-phase distribution in the catalytic layers by SEM cross-section images (BSD detector). The 20NFO80CTO dual-phase catalytic layer exhibits a low-percolative electronic structure with isolated NFO grains. This could influence the electronic transport through the membrane and the oxygen permeability. Likewise, the opposite ratio (80NFO20CTO) will also affect the oxygen permeability, which is limited by the ionic percolation. The phase distribution of the rest of the intermediate-ratio compositions is adequate for the percolation of both ionic and electronic species.

Table 3. 2. Cell parameters calculated for the different dual-phase samples.

Dual-phase ratio	**Cell parameter (Å)**		**Dual-phase ratio (%$_{vol}$)**	
	$NiFe_2O_4$	**$Ce_{0.8}Tb_{0.2}O_{2-\delta}$**	**$NiFe_2O_4$**	**$Ce_{0.8}Tb_{0.2}O_{2-\delta}$**
20NFO80CTO	8.34 ± 0.04	5.383 ± 0.003	20.6	79.4
40NFO60CTO	8.325 ± 0.003	5.383 ± 0.002	41.1	58.9
50NFO50CTO	8.332± 0.001	5.3889 ± 0.0004	51.1	48.9
60NFO40CTO	8.320± 0.005	5.381 ± 0.004	60.6	39.4
80NFO20CTO	8.331± 0.002	5.391 ± 0.001	80.5	19.5

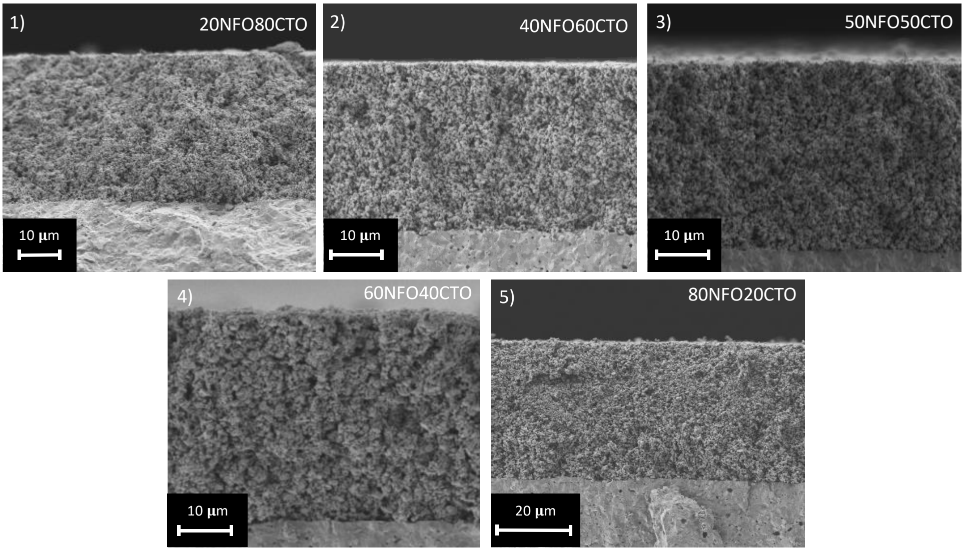

Figure 3. 4. Cross-section SEM image for the different dual-phase layers: 1) **20NFO80CTO**; 2) **40NFO60CTO**; 3) **50NFO50CTO**; 4) **60NFO40CTO** and 5) **80NFO20CTO.**

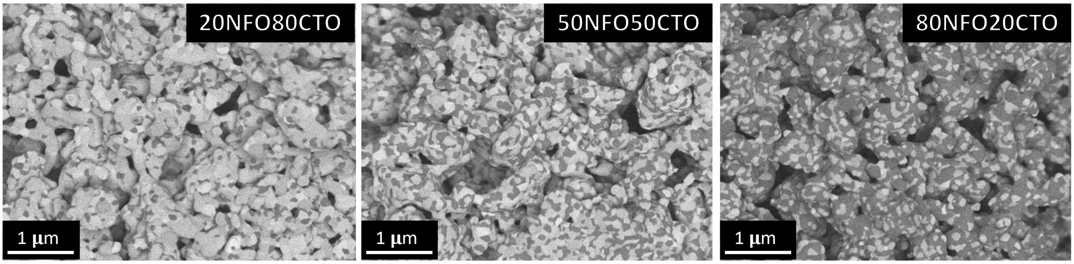

Figure 3. 5. SEM cross-section images with the BSD detector for **20NFO80CTO**, **50NFO50CTO**, and **80NFO20CTO** catalytic layers.

3.3. EIS study for different ratios in dual-phase electrodes

EIS analysis on symmetrical cells enabled us to study the surface reactions for catalytic layers and understand the limitations of the dual-phase composition. Here, different dual-phase materials (20NFO80CTO, 40NFO60CTO, 50NFO50CTO, 60NFO40CTO, and 80NFO20CTO) were measured as electrodes in a temperature range between 850 ºC and 700 ºC in air and fixing the temperature at 850 and 700 ºC, at different pO_2.

Figure 3. 6 shows the polarization resistance (R_p) as a function of the temperature and electrode composition. The polarization resistance accounts for the electrode resistances involving various gas-exchange steps. The inset in Figure 3. 6 shows the Nyquist plot of 50NFO50CTO at 850 ºC in air. Overall, the best-performing electrode is the 20NFO80CTO showing a R_p of 0.117 $\Omega\cdot cm^2$ at 850 ºC in air, followed by 40NFO60CTO, 50NFO50CTO, 60NFO40CTO, and 80NFO20CTO, respectively.

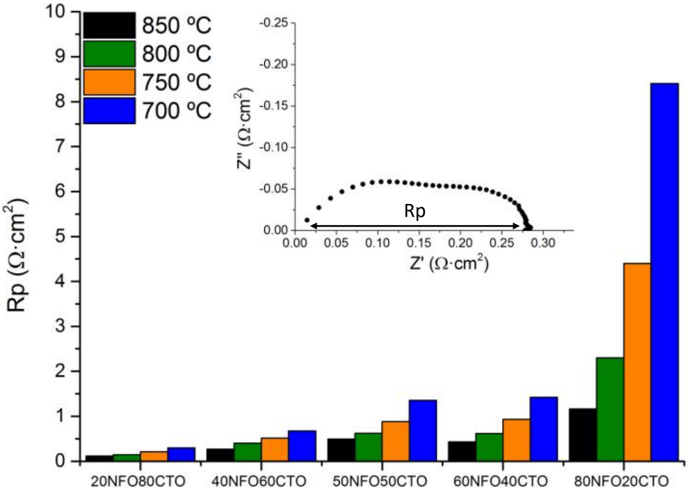

Figure 3. 6. Polarization resistance (R_p) for the dual-phase electrodes (20NFO80CTO, 40NFO60CTO, 50NFO50CTO, 60NFO40CTO, and 80NFO20CTO) from 850 to 700 °C in air.

The impedance spectra of the cells with 60NFO40CTO, 50NFO50CTO, and 40NFO60CTO electrodes show that the polarization resistance increased as temperature decreased (Figure 3. 7). Qualitatively, the major resistive contributions are shifted progressively towards lower frequencies with decreasing temperatures. Figure 3. 8 represents the impedance spectra for the cells with 80NFO20CTO and 20NFO80CTO electrode compositions. The higher amount of ionic phase (CTO) in the dual-phase electrode provides a lower polarization resistance (R_p), which can also be correlated with a higher oxygen permeation, as shown in the next section. Remarkably, the difference in R_p is 10 times lower for 20NFO80CTO compared to 80NFO20CTO (Figure 3. 8) at 850 ºC.

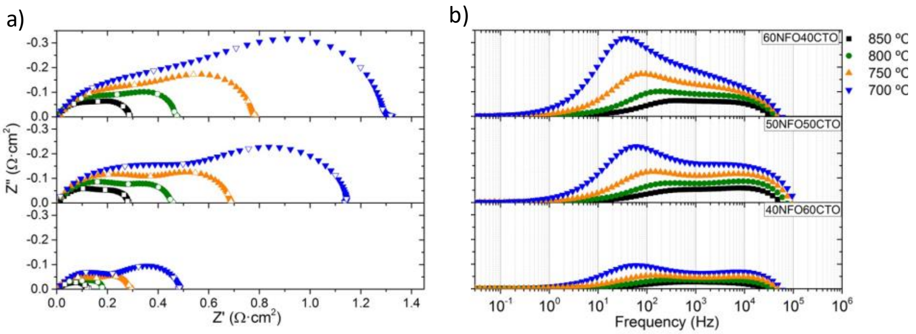

Figure 3. 7. Impedance spectra for symmetrical cells (Nyquist **(a)** and Bode **(b)** diagram) with different concentrations of dual-phase materials (60NFO40CTO, 50NFO50CTO, and 40NFO60CTO) as electrodes in air at different temperatures (T = 850-700 °C) (ohmic losses were subtracted for clarity reasons).

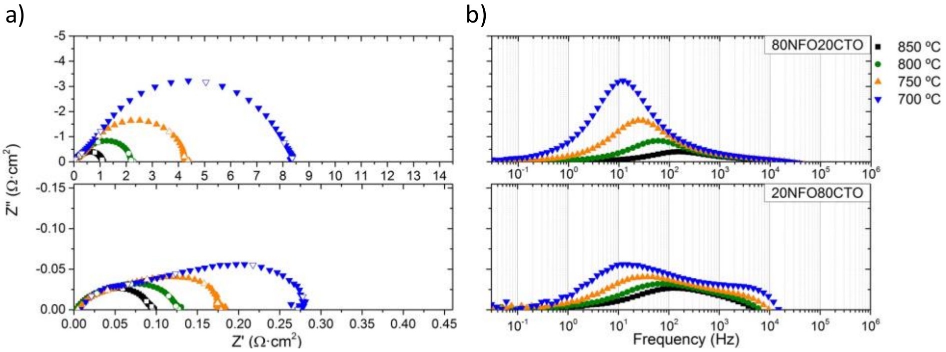

Figure 3. 8. Impedance spectra for symmetrical cells (Nyquist **(a)** and Bode **(b)** diagram) with different concentrations of dual phase materials (80NFO20CTO and 20NFO80CTO) as electrodes in air at different temperatures (T = 850-700 °C) (ohmic losses were subtracted for clarity reasons).

Impedance spectra were fitted to the equivalent circuit: $L + R_{\mathrm{ohmic}} + RQ_{\mathrm{MF}} + RQ_{\mathrm{HF}}$ ($R_p = R_{\mathrm{MF}} + R_{\mathrm{HF}}$) since it is possible to distinguish two contributions in the high and mid frequency range (HF and MF). The 20NFO80CTO material presented another resistance at low frequencies, R_{LF}. The fitting parameters of the equivalent circuit are available in

Table 3. ***3***.

Table 3. 3. Fitted parameters of the equivalent circuit for all the samples in air at 850 ºC.

Fit	**Units**	**NFO/CTO**				
		20/80	**40/60**	**50/50**	**60/40**	**80/20**
R_{HF}	$\Omega\cdot cm^2$	0.022 ±0.003	0.21 ±0.02	0.418 ±0.007	0.339 ±0.001	0.289 ±0.004
Ceq_{HF}	F/cm^2	$1.95\cdot10^{-3}$	$8.62\cdot10^{-6}$	$6.62\cdot10^{-6}$	$2.42\cdot10^{-5}$	$1.67\cdot10^{-4}$
ω_{HF}	Hz	$3.72\cdot10^{3}$	$8.84\cdot10^{4}$	$5.75\cdot10^{4}$	$1.94\cdot10^{4}$	$3.31\cdot10^{3}$
R_{MF}	$\Omega\cdot cm^2$	0.085 ±0.005	0.056 ±0.003	0.075 ±0.002	0.090 ±0.001	0.873 ±0.005
Ceq_{MF}	F/cm^2	$3.45\cdot10^{-3}$	$1.50\cdot10^{-3}$	$1.52\cdot10^{-3}$	$1.59\cdot10^{-3}$	$3.05\cdot10^{-4}$
ω_{MF}	Hz	$1.35\cdot10^{2}$	$4.71\cdot10^{2}$	$3.48\cdot10^{2}$	$2.76\cdot10^{2}$	$1.49\cdot10^{2}$
R_{LF}	$\Omega\cdot cm^2$	0.010 ±0.002				
Ceq_{LF}	F/cm^2	$5.72\cdot10^{-2}$				
ω_{LF}	Hz	8.16				

The processes that occur at HF can be related to electronic conduction, whereas MF processes can be connected to the dissociation of O_2 on the TPB [30–32]. The resistance at higher frequencies increases at lower temperatures. We attribute this to the NFO's poor total conductivity compared with, for example, $La_{0.5}Sr_{0.5}MnO_3$ (electronic semiconductor material commonly used), 0.26 $S\cdot cm^{-1}$, and 300 $S\cdot cm^{-1}$, respectively [33,34]. By comparing the activation energy (E_a) of each contribution and the activation energy for the R_p (Table 3. 4), it is possible to infer the nature of the limiting step in these electrodes. For all of them (except for 80NFO20CTO), the E_a of R_p is closer to the contribution at HF, indicating that electronic conductivity is the dominant contribution. Therefore, the best performance is observed for the electrode with less NFO content, 20NFO80CTO. In the case of 80NFO20CTO, the E_a for the R_p is closer to the contribution of MF rather than HF, which is attributed to the low availability of TPBs and low ionic-conductivity percolation due to the low amount of CTO.

Table 3. 4. Activation energy (E_a) for the global and the different contributions and the polarization resistance at 850 ºC.

	E_a R_p	**E_a R_{HF}**	**E_a R_{MF}**	**E_a R_{LF}**	**R_p (850 ºC)**
	eV	eV	eV	eV	$\Omega\cdot cm^2$
20NFO80CTO	0.59	0.81	0.39	1.15	0.117
40NFO60CTO	0.57	0.46	0.88		0.265
50NFO50CTO	0.64	0.40	1.28		0.493
60NFO40CTO	0.75	0.58	1.16		0.429
80NFO20CTO	1.24	1.02	1.30		1.162

An EIS experiment at different pO_2 was carried out to more precisely study the surface reactions and the other contributions. Figure 3. 9 shows the contribution of the cells when the pO_2 decreases stepwise from 21% to 2.1% at 850 ºC. By reducing pO_2, a new contribution appears at low frequencies (LF). The three different contributions in the impedance spectra are fitted to the following three resistance: $R_p = R_{LF} + R_{MF} + R_{HF}$. The low-frequency contribution (LF), which can be related to the gas diffusion of the O_2 [35], shows the strongest increment of its associated resistance (R_{LF}) with decreasing pO_2. This R_{LF} increment is particularly pronounced in the case of 20NFO80CTO compared to the others [35].

The resistance for the distinct contributions' changes with the pO_2 following a power law (Eq. 3. 1), where the exponent is characteristic of the controlling surface-exchange step:

$$R_i \sim pO_2^{-n} \qquad \text{Eq. 3. 1}$$

$$n=1: \quad O_2(g) \leftrightarrow O_{2\,ads} \qquad \text{Eq. 3. 2}$$

n=1/2: $O_{2\,ads} \leftrightarrow 2\,O_{ads}$ Eq. 3. 3

n=1/4: $O_{ads} + 2e^{-} + V_{O}^{\cdot\cdot} \leftrightarrow O_{O}^{x}$ Eq. 3. 4

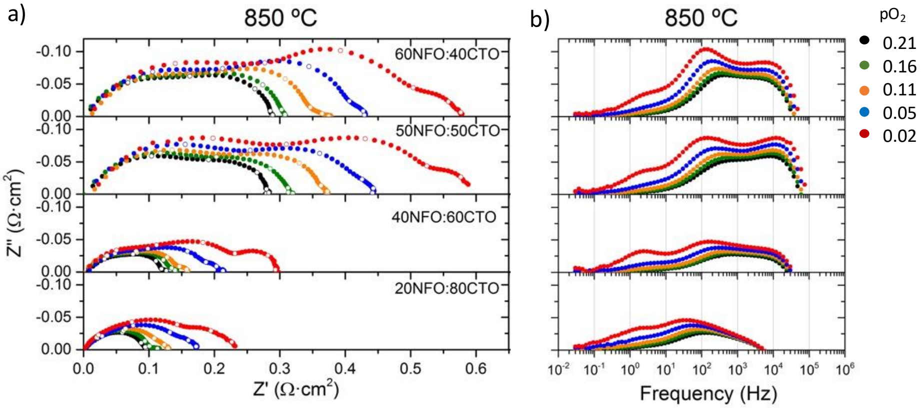

Figure 3. 9. Impedance spectra for symmetrical cells (Nyquist **(a)** and Bode **(b)** diagram) with different concentrations of dual phase materials (60NFO40CTO, 50NFO50CTO and 40NFO60CTO, and 20NFO80CTO) as electrodes at 850 ºC in different pO_2 (pO_2 = 0.21-0.02) (ohmic losses were subtracted for clarity reasons).

The polarization resistance contributions of 20NFO80CTO, 40NFO60CTO, 50NFO50CTO, and 60NFO40CTO are shown in Figure 3. 10. The resistance at mid frequencies (R_{MF}) can be associated with the incorporation of oxygen (exponential factor near -1/2 as in Eq. 3. 3) or with low concentrations of TPB (exponential factor is near -1/4 as in Eq. 3. 4) [35,36]. These two steps typically control the surface-exchange kinetics in dual-phase materials. Resistances at low frequencies and with an exponential factor near -1 are associated with sluggish O_2 gas diffusion [35]. 20NFO80CTO and 80NFO20CTO electrodes are limited by MF processes (See Figure 3. 10 and Figure 3. 11). For 20NFO80CTO, the limiting step is related to the TPB concentration (n = -1/4,) but for the 80NFO20CTO, the limiting step is the dissociation of the oxygen (n = -1/2). The limiting step appearing at higher frequencies (HF) can be correlated to the low conductivity of the NFO (0.26 S·cm^{-1} at 800 ºC) [33].

Even so, for 20NFO80CTO, the resistance at MF associated with the TPBs concentration is similar to the resistance at LF (gas-phase diffusion of O_2) at low pO_2, while HF resistance is lower. This is in line with the optimal performance of 20NFO80CTO observed for this composite series.

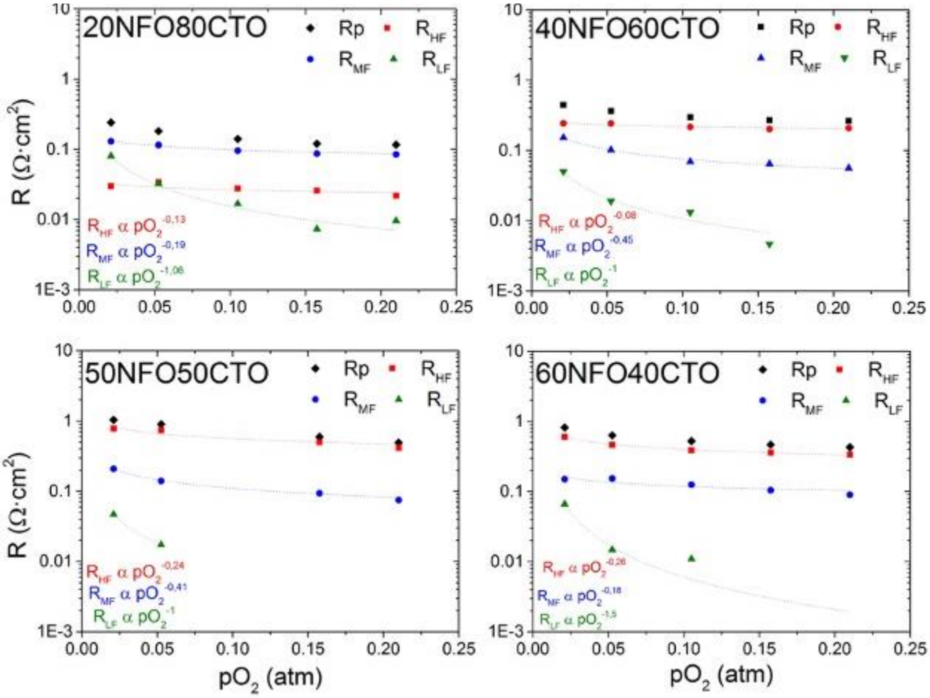

Figure 3. 10. Polarization resistances of the cells with different amounts of NFO and CTO as electrodes as a function of the pO_2 = 0.21-0.021 atm at 850 °C.

R_p contributions of the 80NFO20CTO are shown in Figure 3. 11, displaying the highest Rp compared to the other samples. The limiting contribution is related to oxygen dissociation (exponential factor -1/2). Additionally, a contribution at very high frequencies (1-10 kHz) becomes visible and can be related to the electronic transport in NFO, for which pO_2 dependence (n = 0) is associated with the restricted transport of oxygen ions to the CTO phase [37]. This resistance does not depend on the pO_2; thus, it is not controlled by surface exchange reactions.

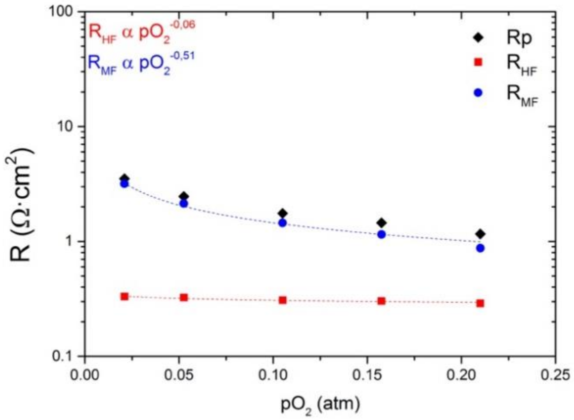

Figure 3. 11. Polarization resistances of the cell with 80NFO20CTO electrodes as a function of the $pO_2 = 0.21\text{-}0.021$ atm at T = 850 °C.

3.4. Influence of the catalytic layers on the oxygen permeation

Oxygen permeation studies were performed in the range from 850 to 700 ºC for 650 µm-thick 50NFO50CTO monolithic membranes and different compositions of the dual-phase catalytic layers, xNFO(100-x)CTO (x = 20, 50, 60, and 80). A bare membrane without a catalytic layer was also measured for comparison. Figure 3. 12 illustrates the improvement of the oxygen permeation flux by adding a catalytic layer regardless of its composition, as expected from the improvement of the determining surface gas exchange [38].

In general, the surface exchange reaction includes two known mechanisms of oxygen transport: (i) the oxygen diffuses through the surface of the catalytic layer, and (ii) the oxygen ions are transported by the ionic phase of the catalytic layer until the bulk of the membrane. In the case of 80NFO20CTO, the abundant electronic phase blocks the oxygen-ion transport through the catalytic layer and limits the reaction in TPB, as shown in the schematics in Figure 3. 13a. In the case of 20NFO80CTO, ions may go through the interphase and the surface, having both transport mechanisms as depicted in Figure 3. 13b, resulting in the highest oxygen permeation observed in Figure 3. 12.

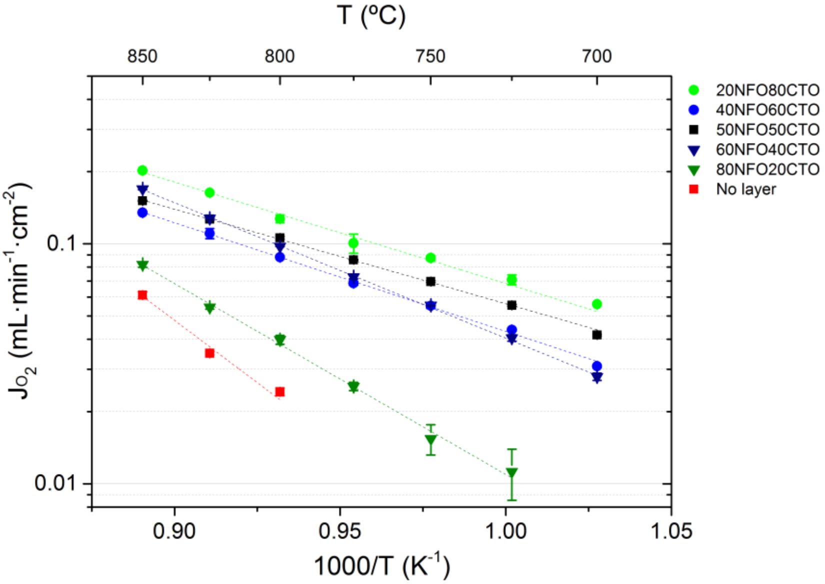

Figure 3. 12. Oxygen permeation at 850-700 °C for 50NFO50CTO membranes with different dual-phase catalytic layer compositions.

For the 40NFO60CTO, 50NFO50CTO, and 60NFO40CTO dual-phase membrane materials, the highest oxygen permeation flux has not been achieved by the one with more ionic phase (40NFO60CTO) at 850 ºC [29]. Consequently, the intrinsic difference in transport mechanism between the gas-tight separation layer (membrane) and the surface-activation catalytic layer is reflected in a distinct optimal composition of each dual-phase functional layer. The percolative channels are more influential in bulk transport than surface-exchange reactions.

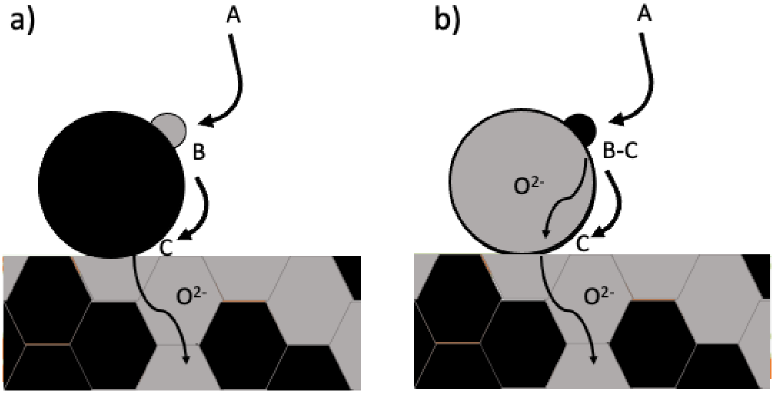

Figure 3. 13. Oxygen mechanism transport for the catalytic layer of **a)** 80NFO20CTO and **b)** 20NFO80CTO.

As already explained, the activation energy (E_a) is related to the process's limiting steps. In the case of oxygen transport through ionic membranes, there are two main limiting steps: surface exchange reactions and diffusion through the bulk. The diffusion through the bulk follows Wagner´s Law and is controlled by temperature and pO_2 gradient, the thickness of the membrane, and the ambipolar conductivity [38]. Typically, lower E_a values indicate that the dual-phase membrane permeation is controlled by bulk diffusion, while higher E_a values involve an increasing influence of surface exchange reactions [38]. In the present study, the activation energies have a similar correlation to oxygen permeation, i.e., the higher the oxygen permeation flux, the lower the activation energy.

Table 3. 5 shows E_a values and the oxygen permeation flux (J_{O2}) at 850 °C of the different catalytic layers: 20NFO80CTO, 40NFO60CTO, 50NFO50CTO, 60NFO40CTO, 80NFO20CTO and no catalytic layer. 60NFO40CTO has a higher activation energy than the rest, thus being more limited by surface-exchange reactions. 50NFO50CTO catalytic layer showed the exception in behavior with the lowest E_a in this study. A plausible explanation could be that the membrane and the catalytic layer have the same composition, thus, the interface and attachment are

most optimal in this case. Still, it exhibits lower oxygen permeation flux than the catalytic layer 20NFO80CTO, which can be explained by a higher absolute number of TPB to incorporate O^{2-}. And this one has twice lower E_a than 80NFO20CTO, indicating that the ionic phase is fundamental to improving the oxygen transport and the surface reactions in the catalytic layers.

Table 3. 5. Results of oxygen permeation studies over a 650 µm-thick 50NFO50CTO with different compositions of catalytic layers: activation energy (850-700ºC); and oxygen permeation at 850ºC.

Catalytic layer composition	**E_a J_{O2}**	**J_{O2} (850 ºC)**
	eV	**mL·min^{-1}·cm^{-2}**
20NFO80CTO	0.84 ± 0.04	0.202 ± 0.002
40NFO60CTO	0.90 ± 0.01	0.135 ± 0.002
50NFO50CTO	0.78 ± 0.01	0.151 ± 0.001
60NFO40CTO	1.12 ± 0.01	0.169 ± 0.001
80NFO20CTO	1.58 ± 0.05	0.082 ± 0.002
No layer	2.18± 0.05	0.060 ± 0.002

3.5. Conclusions

The influence of the composition of dual-phase porous catalytic layers on the oxygen-membrane separation was investigated by oxygen transport and electrochemical methods. EIS studies showed a decrease in polarization resistance as the amount of ionic phase in the catalytic layers increases, which agrees with the oxygen permeation studies. For the catalytic layer with the highest amount of ionic phase (20NFO80CTO), the surface exchange reaction is controlled by the processes occurring at mid frequencies (around 100 Hz), which are related to the TPB concentration. On the other hand, the rest of the electrodes are controlled by high-frequency processes (about 1000-10000 Hz), which indicates that these catalytic layers (electrodes) are limited by electronic conduction. The experiments at different pO_2 allowed for characterizing the limiting steps for each dual-phase layer. 80NFO20CTO layer mechanism is determined by 2 steps: the principal appears at MF and with an exponent of n=-1/2 related to the O_2 dissociation; the second one appears for HF and with n = 0 that indicates insufficient electronic conductivity of the NFO (0.26 $S\cdot cm^{-1}$ at 800 ºC). In the case of intermediate phase ratios, i.e., 60NFO40CTO, 50NFO50CTO, and 40NFO60CTO, the transport process is limited by 3 steps: the principal appears at HF and with an exponent of n=-1/4 that indicates the low density of three phase boundary; the second one appears at MF (n=-1/2) indicative of O_2 dissociation limitations; and the last one at LF (n=-1) ascribed to low oxygen concentration related with its adsorption (or gas diffusion). The latest case is for 20NFO80CTO, showing the primary limiting step at MF (n=-1/2) related to limited TPBs. Still, the low total resistance suggests that the diffusion of O_2 becomes very limiting at low pO_2, unlike other dual-phase electrodes. Among these materials, the optimal catalytic layer is the one with the highest amount of ionic phase (20NFO80CTO) that reaches an oxygen permeation flux of 0.2 $NmL\cdot min^{-1}\cdot cm^{-2}$ on a 50NFO:50CTO membrane at 850 ºC. The lowest activation energies in oxygen permeation were obtained for 20NFO80CTO and 50NFO50CTO, being 0.84 and 0.78 eV, respectively. The oxygen permeation is controlled by the oxygen bulk diffusion rather than the surface exchange reactions for these two layers. Moreover, the 20NOF80CTO exhibits the highest oxygen permeation flux. There is a correlation between the response of the electrodes/catalytic layers from EIS tests and the ΔpO_2-driven oxygen permeation studies. Dual-phase layers with a higher proportion of ionic phase showed the highest performance in both studies. Therefore, it can be concluded that for dual-phase catalytic layers, the surface exchange reactions are controlled by steps related to the ionic phase rather than the electronic phase.

3.6. References.

1. Wu, F., Argyle, M. D., Dellenback, P. A. & Fan, M. Progress in O2 separation for oxy-fuel combustion–A promising way for cost-effective CO2 capture: A review. *Progress in Energy and Combustion Science* vol. 67 188–205 Preprint at https://doi.org/10.1016/j.pecs.2018.01.004 (2018).

2. Himma, N. F., Wardani, A. K., Prasetya, N., Aryanti, P. T. P. & Wenten, I. G. Recent progress and challenges in membrane-based O2/N2 separation. *Reviews in Chemical Engineering* **35**, 591–625 (2019).

3. Allam, R. J. Improved oxygen production technologies. *Energy Procedia* **1**, 461–470 (2009).

4. Schulze-Küppers, F. *et al.* Design and fabrication of large-sized planar oxygen transport membrane components for direct integration in oxy-combustion processes. *Sep Purif Technol* **220**, 89–101 (2019).

5. Kotowicz, J., Job, M. & Brzęczek, M. Thermodynamic analysis and optimization of an oxy-combustion combined cycle power plant based on a membrane reactor equipped with a high-temperature ion transport membrane ITM. *Energy* 117912 (2020) doi:10.1016/j.energy.2020.117912.

6. Zhang, G., Jin, W. & Xu, N. Design and Fabrication of Ceramic Catalytic Membrane Reactors for Green Chemical Engineering Applications. *Engineering* **4**, 848–860 (2018).

7. Lobera, M. P., Escolástico, S., Garcia-Fayos, J. & Serra, J. M. Ethylene production by ODHE in catalytically modified Ba 0.5Sr0.5Co0.8Fe0.2O 3-γ membrane reactors. *ChemSusChem* **5**, 1587–1596 (2012).

8. Gaudillere, C., Garcia-Fayos, J. & Serra, J. M. Enhancing oxygen permeation through hierarchically-structured perovskite membranes elaborated by freeze-casting. *J Mater Chem A Mater* **2**, 3828–3833 (2014).

9. Sunarso, J., Hashim, S. S., Zhu, N. & Zhou, W. Perovskite oxides applications in high temperature oxygen separation, solid oxide fuel cell and membrane reactor: A review. *Progress in Energy and Combustion Science* vol. 61 57–77 Preprint at https://doi.org/10.1016/j.pecs.2017.03.003 (2017).

10. Leo, A. *et al.* Copper oxide - perovskite mixed matrix membranes delivering very high oxygen fluxes. *J Memb Sci* **526**, 323–333 (2017).

11. Almar, L. *et al.* Improved Phase Stability and CO2 Poisoning Robustness of Y-Doped Ba0.5Sr0.5Co0.8Fe0.2O3-δ SOFC Cathodes at Intermediate Temperatures. *ACS Appl Energy Mater* **1**, 1316–1327 (2018).

12. Lhotzky, C. Development of new dual phase membranes for oxygen separation Research Report. (2016).

13. Li, C. *et al.* Oxygen permeation through single-phase perovskite membrane: Modeling study and comparison with the dual-phase membrane. *Sep Purif Technol* **235**, 116224 (2020).

14. Xue, J., Liao, Q., Wei, Y., Li, Z. & Wang, H. A CO2-tolerance oxygen permeable 60Ce0.9Gd0.1O2-δ-40Ba0.5Sr0.5Co0.8Fe0.2O3-δ dual phase membrane. *J Memb Sci* **443**, 124–130 (2013).

15. Han, N. *et al.* Highly Stable Dual-Phase Membrane Based on Ce 0.9 Gd 0.1 O 2–δ —La 2 NiO 4+δ for Oxygen Permeation under Pure CO 2 Atmosphere. *Energy Technology* **7**, 1–10 (2019).

16. Chen, G. *et al.* Novel CO2-tolerant dual-phase Ce0.9Pr0.1O2–δ - La0.5Sr0.5Fe0.9Cu0.1O3–δ membranes with high oxygen permeability. *J Memb Sci* **595**, 117530 (2020).

17. Joo, J. H. *et al.* Substantial Oxygen Flux in Dual-Phase Membrane of Ceria and Pure Electronic Conductor by Tailoring the Surface. *ACS Appl Mater Interfaces* **7**, 14699–14707 (2015).

18. Zhang, C. *et al.* Oxygen permeation behavior through Ce0.9Gd0.1O2-δ membranes electronically short-circuited by dual-phase Ce0.9Gd0.1O2-δ-Ag decoration. *J Mater Chem A Mater* **3**, 19033–19041 (2015).

19. Chen, C. S., Kruidhof, H., Bouwmeester, H. J. M., Verweij, H. & Burggraaf, A. J. Oxygen permeation through oxygen ion oxide-noble metal dual phase composites. *Solid State Ion* **86–88**, 569–572 (1996).

20. Samson, A. J., Søgaard, M. & Vang Hendriksen, P. (Ce,Gd)O2-δ-based dual phase membranes for oxygen separation. *J Memb Sci* **470**, 178–188 (2014).

21. Chen, C. S. *et al.* Microstructural development, electrical properties and oxygen permeation of zirconia-palladium composites. *Solid State Ion* **76**, 23–28 (1995).

22. Joo, J. H. *et al.* Dramatically enhanced oxygen fluxes in fluorite-rich dual-phase membrane by surface modification. *Chemistry of Materials* **26**, 4387–4394 (2014).

23. Zhu, X. & Yang, W. Composite membrane based on ionic conductor and mixed conductor for oxygen permeation. *AIChE Journal* **54**, 665–672 (2008).

24. Kwon, Y. il *et al.* Novel strategy for improving the oxygen permeability of zirconia-based dual-phase membranes. *Energy Environ Sci* **12**, 1358–1368 (2019).

25. Yi, E.-J., Yoon, M.-Y., Moon, J.-W. & Hwang, H.-J. Fabrication of a MnCo2O4/gadolinia-doped Ceria (GDC) Dual-phase Composite Membrane for Oxygen Separation. *Journal of the Korean Ceramic Society* **47**, 199–204 (2010).

26. García-Fayos, J., Ruhl, R., Navarrete, L., Bouwmeester, H. J. M. & Serra, J. M. Enhancing oxygen permeation through Fe2NiO4-Ce0.8Tb0.2O2-δ composite membranes using porous layers activated with Pr6O11 nanoparticles. *J Mater Chem A Mater* **6**, 1201–1209 (2018).

27. Pirou, S., García-Fayos, J., Balaguer, M., Kiebach, R. & Serra, J. M. Improving the performance of oxygen transport membranes in simulated oxy-fuel power plant conditions by catalytic surface enhancement. *J Memb Sci* **580**, 307–315 (2019).

28. Gaudillere, C., Garcia-Fayos, J., Balaguer, M. & Serra, J. M. Enhanced Oxygen Separation through Robust Freeze-Cast Bilayered Dual-Phase Membranes. *ChemSusChem* **7**, 2554–2561 (2014).

29. Garcia-Fayos, J., Balaguer, M. & Serra, J. M. Dual-Phase Oxygen Transport Membranes for Stable Operation in Environments Containing Carbon Dioxide and Sulfur Dioxide. *ChemSusChem* **8**, 4242–4249 (2015).

30. Navarrete, L., Balaguer, M., Vert, V. B. & Serra, J. M. Tailoring Electrocatalytic Properties of Solid Oxide Fuel Cell Composite Cathodes Based on (La0.8Sr0.2)0.95MnO3+Δ and Doped Cerias Ce1–xLnxO2–Δ (Ln=Gd, La, Er, Pr, Tb and x=0.1–0.2). *Fuel Cells* **17**, 100–107 (2017).

31. Almar, L. *et al.* A Durable Electrode for Solid Oxide Cells: Mesoporous Ce0.8Sm0.2O1.9 Scaffolds Infiltrated with a Sm0.5Sr0.5CoO3-δ Catalyst. *Electrochim Acta* **235**, 646–653 (2017).

32. Balaguer, M., Vert, V. B., Navarrete, L. & Serra, J. M. SOFC composite cathodes based on LSM and co-doped cerias (Ce 0.8Gd 0.1X 0.1O 2-δ, X = Gd, Cr, Mg, Bi, Ce). *J Power Sources* **223**, 214–220 (2013).

33. Petric, A. & Ling, H. Electrical conductivity and thermal expansion of spinels at elevated temperatures. *Journal of the American Ceramic Society* **90**, 1515–1520 (2007).

34. Nikonov, A. V., Kuterbekov, K. A., Bekmyrza, K. Zh. & Pavzderin, N. B. A brief review of conductivity and thermal expansion of perovskite-related oxides for SOFC cathode. *Eurasian Journal of Physics and Functional Materials* **2**, 274–292 (2018).

35. Almar, L., Szász, J., Weber, A. & Ivers-Tiffée, E. Oxygen Transport Kinetics of Mixed Ionic-Electronic Conductors by Coupling Focused Ion Beam Tomography and Electrochemical Impedance Spectroscopy. *J Electrochem Soc* **164**, F289–F297 (2017).

36. Almar, L. *et al.* Improved Phase Stability and CO2 Poisoning Robustness of Y-Doped Ba0.5Sr0.5Co0.8Fe0.2O3-δ SOFC Cathodes at Intermediate Temperatures. *ACS Appl Energy Mater* **1**, 1316–1327 (2018).

37. Vladikova, D. E. *et al.* Impedance studies of cathode/electrolyte behaviour in SOFC. *Electrochim Acta* **53**, 7491–7499 (2008).

38. Baumann, S. *et al.* Ultrahigh oxygen permeation flux through supported Ba0.5Sr0.5Co0.8Fe0.2O3-δ membranes. *J Memb Sci* **377**, 198–205 (2011).

4.

NOVEL DUAL-PHASE MIEC MEMBRANES FOR CATALYTIC MEMBRANE REACTORS

4. Novel dual-phase MIEC membranes for catalytic membrane reactors.

4.1. Introduction

As aforementioned, the previous study was focused on dual-phase materials based on $NiFe_2O_4/Ce_{0.8}Tb_{0.2}O_{2-\delta}$ (NFO/CTO) with spinel and fluorite crystal phase structures. This composite material exhibits high stability in CO_2 atmospheres and can even be stable in the presence of low amounts of SO_2 without permanent degradation [1–3]. However, this material shows limited permeation rates compared to other dual-phase materials [4].

In this regard, the primary goal of this study is to improve the permeation for this type of dual-phase OTMs. For that purpose, it was chosen 20% terbia-doped ceria ($Ce_{0.8}Tb_{0.2}O_{2-\delta}$, CTO) as ionic conductor material and Co_2MnO_4 (CMO) replacing the $NiFe_2O_4$ phase (NFO)[5] to study the effect of changing the electronic phase in comparison to previous works [2,3,6,7]. The rationale behind the choice of CMO was due to its high electronic conductivity compared to NFO. Namely, the electric conductivity for CMO and NFO is 60 and 0.26 $S \cdot cm^{-1}$ at 800 ºC, respectively [5]. In addition, this material is of some interest as a cathode for Solid Oxide Fuel Cells (SOFC) because it is commonly used as a current collector in SOFC stacks [8,9]. Improving the electrical conductivity could allow for a lower amount of the electronic phase, thus increasing the amount of the ionic conductivity phase while remaining stable under CO_2. This would result in higher ambipolar transport, thus boosting oxygen permeation. The ratio of the dual-phase ($Co_2MnO_4/Ce_{0.8}Tb_{0.2}O_{2-\delta}$) material was fixed to 40% vol. for the electronic phase and 60% vol. for the ionic phase. This study introduces this dual-phase material as a promising candidate for

OTMs in oxycombustion processes, improving oxygen permeation in CO_2 gas environments.

4.2. Sample preparation

$Co_2MnO_4/Ce_{0.8}Tb_{0.2}O_{2-\delta}$ (CMO/CTO) dual-phase material was prepared by the modified Pechini method, as explained in Chapter 2. This dual-phase material was produced in one pot with a mixture of all the precursors for both phases. To obtain both phases, it was calcinated at 850 ºC for 5 h. The dense membranes and the rectangular bars (for total conductivity measurements) were sintered at 1200 ºC for 5 h. The catalytic layers were sintered at 950 ºC for 2 h after screen-printing deposition on the dense membrane surfaces. In the case of electrochemical impedance studies, the electrodes of this dual-phase material were sintered at the same temperature as the catalytic layers but on a $Ce_{0.8}Gd_{0.2}O_{2-\delta}$ electrolyte.

For this study, two types of samples were considered: one for the oxygen permeation studies and stability in CO_2 and SO_2 and the other for oxygen permeation studies under methane atmospheres. The dimensions of the membranes are specified in Table 4. 1. This membrane formulation will be limited by bulk diffusion, the thickness of the membrane. The optimal dimensions for OTMs for maximizing O_2 permeation is a thin, dense membrane, between 15-30 µm, on a porous support to achieve enough mechanical stability. In this case, dense membranes with more than 600 µm were produced to secure the mechanical strength.

Table 4. 1. Physical dimensions for the dual-phase membranes used in this chapter.

Material	**Environment study**	**Membrane thickness (µm)**	**Catalytic layer thickness (µm)**
40% $NiFe_2O_4$- 60% $Ce_{0.8}Tb_{0.2}O_{2-\delta}$	Ar, CO_2 and SO_2	679	35~30
40% $NiFe_2O_4$- 60% $Ce_{0.8}Tb_{0.2}O_{2-\delta}$	Ar and CH_4	684	35~30

4.3. Physical characterization and total conductivity

4.3.1. Microstructural characterization

X-ray diffraction (XRD) confirmed the crystal structure and phase purity of the synthesized CMO/CTO samples, shown in Figure 4. 1. The Rietveld refinement of the membrane sample sintered at 1200 ºC (Figure 4. 1a) revealed the composition: 45.7 %vol of CMO and 54.3% vol. of CTO for the dual-phase material. Figure 4. 1b shows the XRD pattern for the dual-phase material calcined at 800 ºC for 5 h (at the bottom) and for the rectangular bar at 1200 ºC for 5 h (at the top). Here, the X-ray diffraction patterns for both phases revealed the absence of detectable impurities. The diffraction peak position was maintained, indicating that the dual-phase material did not suffer any compositional change upon annealing at higher temperatures. The sharper peaks observed for the sample calcined at 1200 ºC illustrate the expected increase in crystallinity, maintaining the principal peaks for the CTO and CMO at 28.7 ° and 36.2 °, respectively. The compatibility of both phases -even reached via one-pot synthesis- is remarkable, yet when other related fluorite-spinel composites, such as $Ce_{0.8}Gd_{0.2}O_{1.9}$-$FeCo_2O_4$ [10], lead to secondary phases, e.g., perovskites, along the grain boundaries.

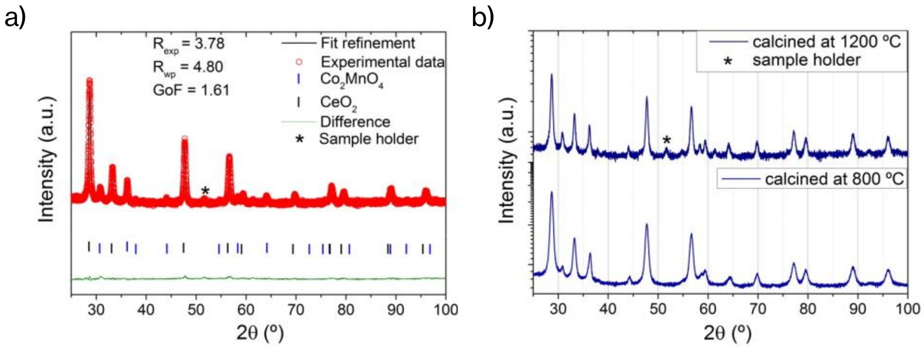

Figure 4. 1. a) Rietveld refinement for CMO/CTO calcined at 1200 ºC for 5 h. The ICSD code for CMO was 01-084-0482, and for CTO 01-083-5824; **b)** X-ray diffraction for CMO/CTO after calcined at 800 ºC (bottom) and at 1200 ºC (top).

To assess the density of the membranes, cross-section images were taken by performing scanning electron microscopy (SEM) (Figure 4. 2a). SEM analysis confirms that the membrane is dense, but some occlusive porosity can be observed. Furthermore, the backscattered electron detector (BSD) was used to see both phases with good percolative paths (Figure 4. 2b). Therefore, ambipolar diffusion through the dual-phase membrane could occur without percolative impediment [11], thus increasing oxygen diffusion.

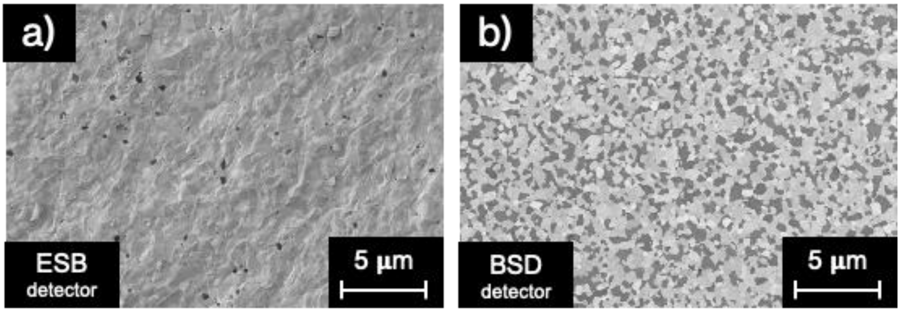

Figure 4. 2. SEM cross-section images for 40CMO60CTO membrane**: a)** with the ESB detector and **b)** with the BSD detector.

4.3.2. Total conductivity

One of the main objectives of this study was to influence the oxygen permeation of the dual-phase spinel/fluorite materials by tailoring the electronic conductivity of the composite, i.e., using CMO as a better electronic conductor than NFO. The reason for the difference in electronic conductivity between these two materials is ascribed to the conduction through different carriers. According to Šutka and Gross, $NiFe_2O_4$ crystalizes in an inverse spinel structure in which Ni^{2+} cations are located in the octahedral sites of the spinel and presents n-type conductivity, which is based on hole (h+) hopping between Ni^{2+} and Ni^{3+} in octahedral sites ($Ni^{2+} + h^+ \leftrightarrow Ni^{3+}$) [12]. However, NFO can change to p-type depending on the fabrication method, especially when the fabrication method leads to higher Ni^{3+}/N^{i2+} ratios [13]. In that case, the conductivity mechanism will be based on electron hopping between $Fe^{3+} + e^{-} \leftrightarrow Fe^{2+}$. On the other hand, Co_2MnO_4 has p-type conductivity [14]. In this spinel, both Co^{3+} and Mn^{3+} cations are located in the octahedral sites, and conductivity is based on electron hopping on these species, especially between Mn^{3+} and Mn^{4+}. It is possible that both the differences between the conductivity mechanism and the electronic configuration gave rise to the huge difference in electrical conductivity, which could also be associated with favorable (less energy demanding) redox requirements of Mn oxidation/reduction transitions if compared to Fe ones. Increasing the electric conductivity is expected to have an impact on the O_2 permeation, following the Wagner equation (Eq. 4. 1):

$$J_{O_2} = -\frac{RT}{4^2F^2L}\int_{lnP_{O_2}^{'}}^{lnP_{O_2}^{''}} \frac{\sigma_{ion}\sigma_{el}}{\sigma_{ion}+\sigma_{el}} \partial\, lnP_{O_2} \qquad \text{Eq. 4. 1}$$

Where R is the gas constant, T is the membrane temperature, F is the Faraday constant, L is the membrane thickness; $\ln P_{O2}''$ and $\ln P_{O2}'$ are the oxygen partial pressures for the sweep and the feed chamber; $\frac{\sigma_{ion}\sigma_{el}}{\sigma_{ion}+\sigma_{el}}$ is the ambipolar conductivity (σ_{amb}), formed by the product of ionic and electronic conductivity and divided by the total conductivity [15].

In this study, the total conductivity of the CMO/CTO material was measured and shown in Figure 4. 3. Also, it was compared with the CTO and other dual-phase material (NFO/CTO), a very stable material in CO_2 [2,6]. Remarkably, the total conductivity of the CMO/CTO material is more than one order of magnitude higher than that of the NFO/CTO composite, 0.77 $S \cdot cm^{-1}$ and 0.07 $S \cdot cm^{-1}$, respectively, at 800 ºC in air [6]. The CTO has a total conductivity of around 0.034 $S \cdot cm^{-1}$ at 800 ºC in air.

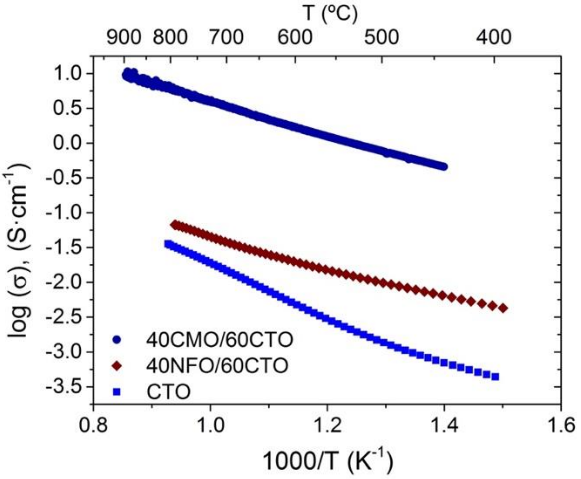

Figure 4. 3. Total conductivity in air at different temperatures for the dual-phase materials 40CMO/60CTO (this study), 40NFO/60CTO, and CTO [6].

4.4. Electrochemical studies

The electrochemical properties of this dual-phase material were characterized by EIS. The dual-phase material was deposited on both sides of a disk-shaped CGO electrolyte as a porous electrode. This study entails two parts: (i) evaluating the influence of pO_2 at 850 ºC and (ii) the effect of temperature, studied under different atmospheres. Namely, air, 5% of O_2/95% Ar, and 5% O_2/95% CO_2. These studies aim at discerning the limiting steps on surface reactions for this dual phase as oxygen-exchange activation layers under OTM operational conditions. A previous study based on NFO/CTO dual-phase materials shows how polarization resistances obtained by EIS studies have a direct correlation with oxygen permeation [16]. To investigate the influence of different oxygen concentrations in the surface exchange reactions, the composite material was studied by EIS for different pO_2 at 850 ºC, represented in Figure 4. 4 as Nyquist (a) and Bode (b) diagrams. The resistance for the different contributions follows a power law with the pO_2 as shown in Eq. 4. 2, where the exponential number is characteristic of the controlling step in the surface exchange reaction mechanism: Eq. 4. 2 to Eq. 4.6 [17].

$R_i \sim pO_2^{-n}$ Eq. 4. 2

n=1: $O_2(g) \leftrightarrow 2\, O_{2\, ads}$ Eq. 4. 3

n=3/8: $O_{ads} + e^- \leftrightarrow O_{ads}^-$ Eq. 4. 4

n=1/4: $O_{ads}^- \leftrightarrow O_{lattice}^-$ Eq. 4. 5

n=1/8: $O_{lattice}^- + e^- \leftrightarrow O_{lattice}^{2-}$ Eq. 4. 6

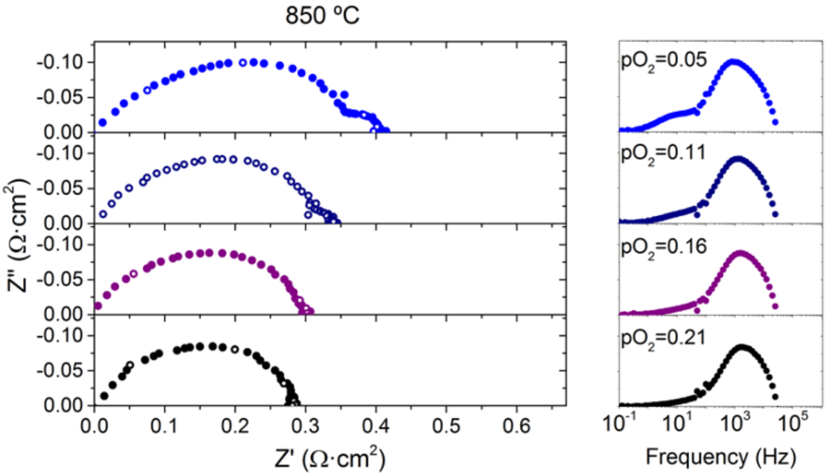

Figure 4. 4. Impedance spectra for symmetrical cells with CMO/CTO electrodes (Nyquist and Bode diagram) for dual-phase material CMO/CTO as the electrode at 850 ºC at different pO_2 (pO_2= 0.21-0.05 bar) (ohmic losses were subtracted for clarity reasons).

Decreasing the oxygen concentration does not reveal a significant increase in the initial surface contributions. However, at pO_2 of 0.11 and 0.05 bar, another contribution appears at low frequencies (lower than 10 Hz). The impedance spectra were fitted to the equivalent circuit $R_p = R_{MF} + R_{HF} + R_{LF}$, Table 4. 2. The results for R_p and each contribution resistance are shown in Figure 4. 5 for the pO_2 range 0.21-0.05 bar at 850 °C.

Table 4. 2. Fitted parameters of the equivalent circuit for CMO/CTO catalytic layer at 850 ºC in different pO_2.

Fit	Units	0.21	0.16	0.11	0.05
R_p	$\Omega\cdot cm^2$	0.35 ± 0.02	0.38 ± 0.02	0.41 ± 0.02	0.47 ± 0.02
R_{HF}	$\Omega\cdot cm^2$	0.181 ± 0.008	0.177± 0.008	0.208 ± 0.008	0.228 ± 0.007
Ceq_{HF}	$F\cdot cm^{-2}$	$4.86\cdot10^{-5}$	$4.81\cdot10^{-5}$	$5.14\cdot10^{-5}$	$5.34\cdot10^{-5}$
ω_{HF}	Hz	$1.81\cdot10^{4}$	$1.87\cdot10^{4}$	$1.49\cdot10^{4}$	$1.31\cdot10^{4}$
R_{MF}	$\Omega\cdot cm^2$	0.172 ± 0.009	0.200 ± 0.008	0.18 ± 0.01	0.202 ± 0.009
Ceq_{MF}	$F\cdot cm^{-2}$	$7.33\cdot10^{-4}$	$7.11\cdot10^{-4}$	$1.10\cdot10^{-3}$	$1.33\cdot10^{-3}$
ω_{MF}	Hz	$1.26\cdot10^{3}$	$1.12\cdot10^{3}$	$8.08\cdot10^{2}$	$5.90\cdot10^{2}$
R_{LF}	$\Omega\cdot cm^2$			0.019 ± 0.003	0.042 ± 0.004
Ceq_{LF}	$F\cdot cm^{-2}$			0.76	0.48
ω_{LF}	Hz			11.13	7.85

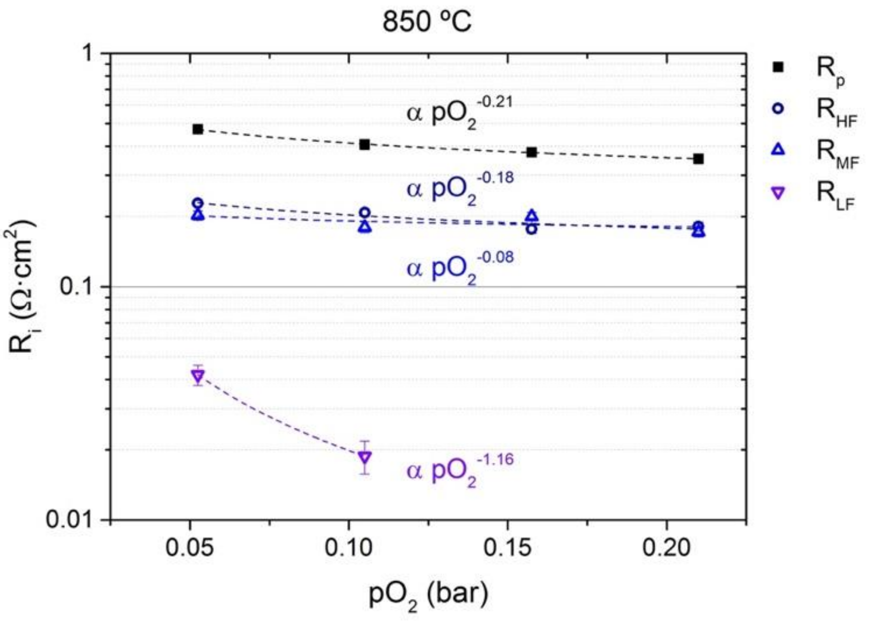

Figure 4. 5. Polarization resistance (R_p) and different fitted resistances (R_{HF}, R_{MF}, and R_{LF}) measured 850 ºC at different pO_2 (from 0.21 to 0.05 bar) for symmetrical cells with CMO/CTO electrodes.

Here, the resistance at low frequencies (R_{LF}) can be associated with the oxygen gas diffusion and adsorption (exponential factor 1.16, close to 1 as in Eq. 2) [16]. The R_{MF} contribution at mid-frequencies and R_{HF} contribution at high frequencies are very similar. Both can be associated with oxygen-ion adsorption through both phases (exponential factor 0.08 for R_{MF} and 0.18 for R_{HF}, near 1/8 as in Eq. 6) [18,19].

Figure 4. 6 collects the Nyquist and Bode diagrams for the CMO/CTO porous catalytic layer from 850 to 750 °C in air, at 5%O_2/95% Ar and 5% of O_2/95% CO_2. It can be observed that the lower the temperature, the higher the polarization resistance (R_p), following a monotonical Arrhenius behavior. At 850 ºC, the R_p for the three environments is very similar, but at 700 ºC, the polarization resistance for CO_2 environments differs from the others.

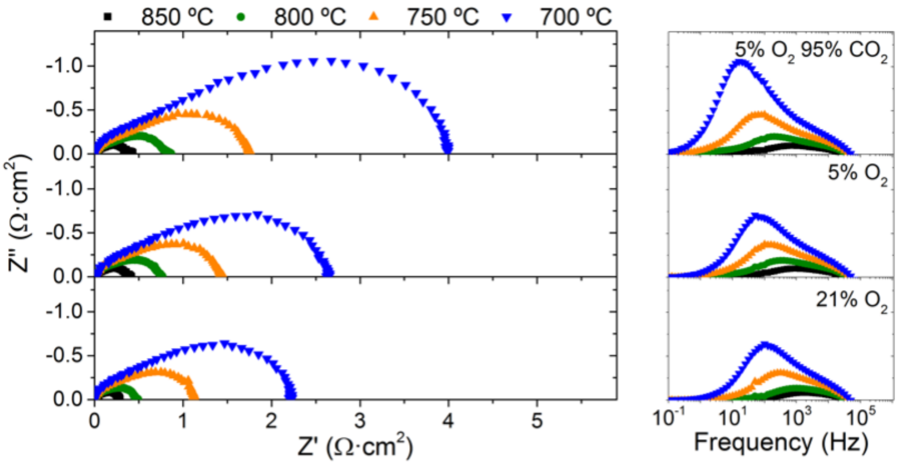

Figure 4. 6. Polarization resistance and different fitted resistances associated with the HF, MF, and LF contributions of the electrode 40CMO/60CTO at different temperatures and different environments: air, at 5% of O_2 in Ar and 5% of O_2 and 95% of CO_2.

These EIS data were fitted to the equivalent electrical circuit $R_p = R_{MF} + R_{HF} + R_{LF}$ (Table 4. 3, 4. 4 and 4. 5), as shown in the inset in Figure 4. 7a. It is also interesting to mention how the highest contributions shift to lower frequencies when the temperature decreases, Figure 4. 7b. At 700 °C in CO_2 environments, the low-frequency and mid-frequency contributions are combined, with a maximum frequency of 23 Hz.

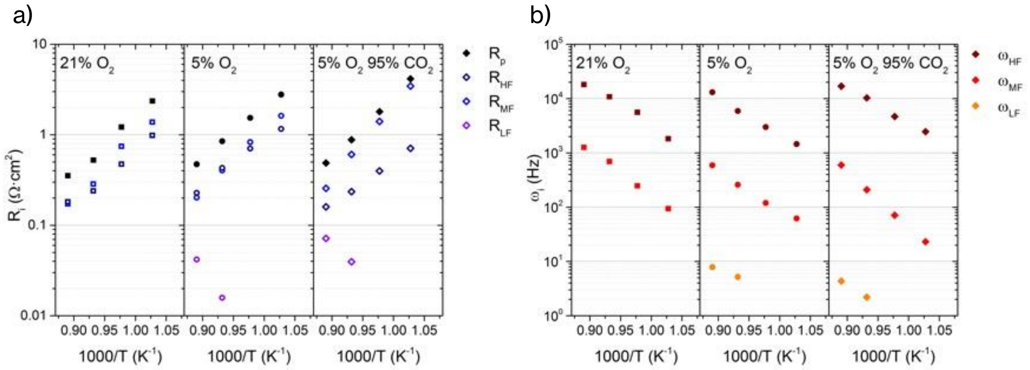

Figure 4. 7. a) Polarization resistance (R_p) and different fitted resistances (R_{HF}, R_{MF}, and R_{LF}); **b)** Different fitted maximum frequency for the different contributions (w_{HF}, w_{MF} and w_{LF}).

Table 4. 3. Fitted parameters of the equivalent circuit for CMO/CTO catalytic layer at different temperatures in air.

Fit	Units	850ºC	800ºC	750ºC	700ºC
R_p	Ω·cm^2	0.35 ± 0.02	0.52 ± 0.03	1.21 ± 0.1	2.36 ± 0.2
R_{HF}	Ω·cm^2	0.181 ± 0.008	0.24± 0.01	0.47 ± 0.06	0.98 ± 0.12
Ceq_{HF}	F·cm^{-2}	4.85·10^{-5}	6.16·10^{-5}	6.04·10^{-5}	8.90·10^{-5}
ω_{HF}	Hz	1.81·10^4	1.08·10^4	5.58·10^3	1.82·10^3
R_{MF}	Ω·cm^2	0.172 ± 0.009	0.28 ± 0.01	0.74 ± 0.05	1.38 ± 0.11
Ceq_{MF}	F·cm^{-2}	7.33·10^{-4}	8.06·10^{-4}	8.67·10^{-4}	1.23·10^{-3}
ω_{MF}	Hz	1.26·10^3	6.94·10^2	2.47·10^2	9.36·10

Table 4. 4. Fitted parameters of the equivalent circuit for CMO/CTO catalytic layer at different temperatures in 5% of O_2.

Fit	Units	850ºC	800ºC	750ºC	700ºC
R_p	$\Omega\cdot cm^2$	0.47 ± 0.02	0.85 ± 0.12	1.53 ± 0.14	2.78 ± 0.36
R_{HF}	$\Omega\cdot cm^2$	0.228 ± 0.006	0.43± 0.06	0.70 ± 0.08	1.16 ± 0.19
Ceq_{HF}	$F\cdot cm^{-2}$	$5.34\cdot10^{-5}$	$6.39\cdot10^{-5}$	$7.56\cdot10^{-5}$	$9.45\cdot10^{-5}$
ω_{HF}	Hz	$1.31\cdot10^{4}$	$5.89\cdot10^{3}$	$2.99\cdot10^{3}$	$1.45\cdot10^{3}$
R_{MF}	$\Omega\cdot cm^2$	0.202 ± 0.009	0.40 ± 0.05	0.83 ± 0.07	1.62 ± 0.17
Ceq_{MF}	$F\cdot cm^{-2}$	$1.33\cdot10^{-3}$	$1.53\cdot10^{-3}$	$1.61\cdot10^{-3}$	$1.59\cdot10^{-3}$
ω_{MF}	Hz	$5.90\cdot10^{2}$	$2.59\cdot10^{2}$	$1.19\cdot10^{2}$	$6.19\cdot10$
R_{LF}	$\Omega\cdot cm^2$	0.042 ± 0.004	0.016 ± 0.005		
Ceq_{LF}	$F\cdot cm^{-2}$	0.48	1.94		
ω_{LF}	Hz	7.85	5.19		

Table 4. 5. Fitted parameters of the equivalent circuit for CMO/CTO catalytic layer at different temperatures in 5% of O_2 and 95% CO_2.

Fit	Units	850ºC	800ºC	750ºC	700ºC
R_p	$\Omega\cdot cm^2$	0.49 ± 0.02	0.88 ± 0.03	1.80 ± 0.02	4.15 ± 0.07
R_{HF}	$\Omega\cdot cm^2$	0.160 ± 0.006	0.235± 0.008	0.40 ± 0.01	0.71 ± 0.03
Ceq_{HF}	$F\cdot cm^{-2}$	$5.89\cdot10^{-5}$	$6.60\cdot10^{-5}$	$8.55\cdot10^{-5}$	$9.15\cdot10^{-5}$
ω_{HF}	Hz	$1.69\cdot10^{4}$	$1.03\cdot10^{4}$	$4.67\cdot10^{3}$	$2.45\cdot10^{3}$
R_{MF}	$\Omega\cdot cm^2$	0.26 ± 0.01	0.61 ± 0.01	1.40 ± 0.01	3.44 ± 0.04
Ceq_{MF}	$F\cdot cm^{-2}$	$2.00\cdot10^{-3}$	$1.60\cdot10^{-3}$	$1.25\cdot10^{-3}$	$1.05\cdot10^{-3}$
ω_{MF}	Hz	$5.94\cdot10^{2}$	$2.09\cdot10^{2}$	$7.09\cdot10$	$2.31\cdot10$
R_{LF}	$\Omega\cdot cm^2$	0.071 ± 0.006	0.040 ± 0.007		
Ceq_{LF}	$F\cdot cm^{-2}$	0.51	1.83		
ω_{LF}	Hz	4.35	2.20		

Here, for the dual-phase catalytic layer in air, the R_p increases from 0.35 $\Omega\cdot cm^2$ at 850 ºC to 2.36 $\Omega\cdot cm^2$ at 750 ºC. This performance is similar at 5% of O_2 in Ar, obtaining 0.47 $\Omega\cdot cm^2$ at 850 ºC and 2.78 $\Omega\cdot cm^2$ at 750 ºC. On the contrary, when the environment changes to 5% O_2 in CO_2, the polarization resistance is similar at the other environments at 850 ºC, but it increases one order of magnitude at 750 ºC, 0.49 $\Omega\cdot cm^{2,}$ and 4.15 $\Omega\cdot cm^{2,}$ respectively. In this study, both principal contributions (R_{HF} and R_{MF}) are in the same range for the atmospheres without CO_2. In contrast, in 5% of O_2 in $CO_{2,}$ both contributions were highly differentiated, with the $\mathrm{R_{MF}}$ higher than the $\mathrm{R_{HF}}$. Mid frequencies are related to surface reactions and adsorption processes. In this case, the presence of CO_2 could interfere with the oxygen adsorption, increasing the resistance for these processes [16]. The activation energies (E_a) for the polarization resistances with both principal contributions are compared in Table 4. 6. The E_a for R_p for the CO_2-free environments had a similar value to the E_a for the resistances at high and mid frequencies, indicating that both contributions had the same relevance. In addition, the E_a for R_p in CO_2 was closer to E_a for the R_{MF}, indicating that in CO_2 environments, the surface exchange reactions were limited by the adsorption processes. These results suggest that the material could potentially be used as an oxygen electrode in solid-oxide cells (SOC) in CO_2-rich environments to electrochemically supply oxygen in oxycombustion processes.

Table 4. 6. The activation energy (E_a) for the global and the different contributions and the polarization resistance at 850°C.

	E_a (R_p)	E_a (R_{HF})	E_a (R_{MF})	R_p (850 °C)
	eV	**eV**	**eV**	**$\Omega \cdot cm^2$**
21% O_2	1.23	1.08	1.36	0.353
5% O_2	1.11	1.01	1.31	0.472
5% O_2 95% CO_2	1.34	0.93	1.63	0.488

4.5. Oxygen permeation studies

The dual-phase membrane consisting of 46%$_{vol.}$ CMO, and 54 %$_{vol.}$ CTO sintered at 1200 °C exhibited a remarkable increase in total conductivity compared to NFO/CTO. In order to enhance the permeation properties, a porous catalytic layer of the same material, CMO/CTO, was added on both sides of the dual-phase membrane. Two *bulk* membranes with a thickness of ~650 μm and catalytic layers with a thickness of ~30 μm and an active surface of 64 mm^2 were employed here.

The oxygen permeation experiments were performed in air at the feed side and Ar at the sweep side. The flows for those chambers were 100 $mL \cdot min^{-1}$ of air in the feed chamber and 150 mL·min^{-1} for the sweep chamber, analyzing the oxygen permeation from 850 ºC to 700 ºC. Furthermore, it was measured with pure oxygen at the feed side, equivalent to pressurized air conditions (air feeding at 5 bar). O_2 permeation results for both conditions are represented in Figure 4. 8 and Table 4. 7.

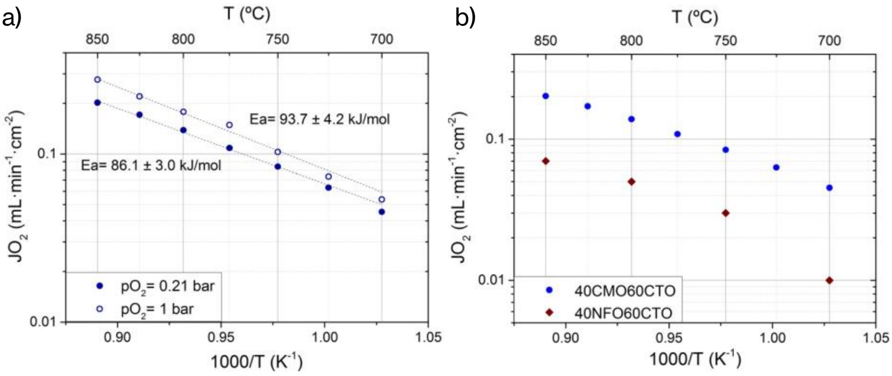

Figure 4. 8. a) Oxygen permeation of a 680 µm-thick CMO/CTO dual-phase membrane under air and pure O_2 environment; **b)** Oxygen permeation of CMO/CTO and NFO/CTO dual-phase membranes under air at different temperatures[6].

Table 4. 7. Oxygen permeation values for CMO/CTO dual-phase membrane under air and pure O_2 environment.

Temperature (°C)	JO_2 (mL·min^{-1}·cm^{-2})	
	oxygen	Air
850	0.2771 ± 0.0006	0.2020 ± 0.0009
825	0.220 ± 0.001	0.1712 ± 0.0006
800	0.1780 ± 0.0006	0.139 ± 0.001
775	0.149 ± 0.002	0.1086 ± 0.0006
750	0.103 ± 0.002	0.0842 ± 0.0006
725	0.073 ± 0.001	0.0631 ± 0.0005
700	0.054 ± 0.002	0.0453 ± 0.0004

Figure 4. 8a shows the oxygen permeation flux under air and pure oxygen for the CMO/CTO membrane. At 850 ºC, the CMO/CTO membrane permeates 0.21 mL·min^{-1}·cm^{-2}, and, when fed with pure oxygen, the permeation reached a value of

0.28 mL·min^{-1}·cm^{-2} at 850 ºC. This permeation is higher than the achieved for the same ratio composition for NFO/CTO membrane (Figure 4. 8b) that produced 0.07 mL·min^{-1}·cm^{-2} at 850 ºC elsewhere [6]. Furthermore, the performance is similar to literature reports by Yi et al. [20] using a dual-phase membrane consisting of CMO and CGO, with values of 0.17 mL·min^{-1}·cm^{-2} at 850 ºC. The activation energies for both feeds were very similar, 86.1 kJ·mol^{-1} and 93.7 kJ·mol^{-1} for air/Ar and O_2/Ar, respectively. These activation energy values are lower than those achieved for the NFO/CTO membrane in air/Ar in the range 800-700 ºC, which was more than 110 kJ·mol^{-1} for all compositions [6], suggesting that gas exchanged is improved in the CMO/CTO membranes.

In addition, with the oxygen permeation values, it is possible to calculate the ambipolar conductivity of these dual-phase membranes, Eq. 4. 7.

$$\sigma_{amb} = -\frac{J_{O_2} 4^2 F^2 L}{RT} \ln\left(\frac{P'_{O_2}}{P''_{O_2}}\right) \qquad \text{Eq. 4. 7}$$

Where σ_{amb} is the ambipolar conductivity, L is the thickness of the membrane, J_{O2} is the oxygen permeation for the dual-phase membrane, T is the temperature of operation, and P'_{O2} and P''_{O2} are the oxygen partial pressure in the sweep and the feed side, respectively. With this data and the total conductivity of the dual-phase material and the electronic conductivity of the electronic phase, it is possible to calculate the ionic conductivity of the CTO, Eq. 4. 8.

$$\sigma_{amb} = \frac{\sigma_{ion}\sigma_{el}}{\sigma_{ion}+\sigma_{el}} = \frac{\sigma_{ion}\sigma_{el}}{\sigma_{tot}} \qquad \text{Eq. 4. 8}$$

Where σ_{tot} is the total conductivity and σ_{el} is the total conductivity for the electronic phase. Table 4. 8 depicts the ambipolar conductivity and the ionic conductivity values determined using Eq. 4. 7 and 4. 8, respectively, for the NFO/CTO and the CMO/CTO membranes at 800 ºC under air/Ar atmospheres.

Table 4. 8. Oxygen permeation and conductivities for dual-phase materials at 800 ºC under Air/Ar atmospheres.

	J_{O2} (mL·min^{-1}·cm^{-2})	σ_{tot} (S·cm^{-1})	σ_{amb} (S·cm^{-1})	σ_{ion} (S·cm^{-1})
40NFO/60CTO	0.05	0.07	0.11	0.03
40CMO/60CTO	0.14	6.31	0.29	0.03

For both studies, the ionic conductivity calculated was 0.030 S·cm^{-1}, similar to the total conductivity values of CTO at these conditions (0.034 S·cm^{-1}), confirming that the fluorite phase is the only responsible for ionic conductivity in the membrane. One of the main advantages of dual-phase membranes is their stability in acidic gas environments, such as in the presence of CO_2 or SO_2. Two different experiments were made to evaluate the performance of these membranes under these atmospheres. Figure 4. 9a shows the oxygen permeation in different concentrations of CO_2 (0-100%) in the sweep side, and Figure 4. 9b shows the oxygen permeation and stability test for 150 h in Ar, 30% CO_2 in Ar and 30% CO_2 and 250 ppm of SO_2 in Ar. In Figure 4. 9a, the total flows of the feed side and sweep side are 100 mL·min^{-1} of air in the feed chamber and 150 mL·min^{-1} of the mixture (CO_2 + Ar) in the sweep chamber at 850 ºC.

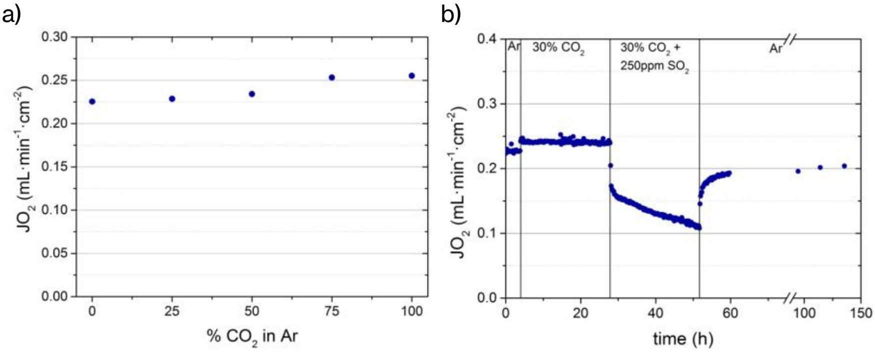

Figure 4. 9. Oxygen permeation (Stability studies) of a 679 µm-thick CMO/CTO membrane with 100 mL·min^{-1} of air at the feed side and 150 mL·min^{-1} of the different mixes at the sweep side at 850 ºC: **a)** different concentrations of CO_2 (0-100%) and **b)** 24 h of 30% CO_2 and 24 h of 30% CO_2 and 225 ppm SO_2 environments.

Here, the oxygen permeation increased with increasing CO_2 concentrations on the sweep side, from 0.22 to 0.25 mL·min^{-1}·cm^{-2}, at 850 ºC. This behavior was also described for NFO/CTO dual-phase membranes[6] and ascribed to the better sweep and thermal-transfer properties of CO_2 with respect to Ar [21]. The maximum oxygen permeation was achieved for 100% CO_2 in the sweep side. This is a sign of the absence of any undesired effect or reaction between the CO_2 and both crystalline phases. This enhancement in the oxygen permeation under CO_2 at 850 ºC is also shown in the experiment depicted in Figure 4. 9b. However, in the presence of SO_2, the permeation of O_2 decreased progressively for 24 h, evidencing that SO_2 poisoned the membrane, blocking the active sites. Significantly, when CO_2 and SO_2 were removed from the stream, the O_2 permeation increased again until 0.20 mL·min^{-1}·cm^{-2}. However, the initial oxygen permeation level achieved at the stability test of 0.22 mL·min^{-1}·cm^{-2} was not recovered, indicative of non-reversible membrane evolution on the SO_2 stream.

When comparing with NFO/CTO membrane [6], the oxygen permeation for the CMO/CTO membrane shows around two times higher values than for the NFO/CTO membrane at 850ºC in air/argon, viz. 0.22 mL·min^{-1}·cm^{-2} and 0.11 mL·min^{-1}·cm$^{-2,}$ respectively. This oxygen permeation increase was maintained under a CO_2 environment, 0.24 mL·min^{-1}·cm^{-2} and 0.13 mL·min^{-1}·cm^{-2} for CMO/CTO and NFO/CFO membranes, respectively. However, under SO_2 environments, the loss of permeation capacity was more accentuated for the CMO/CTO membrane than for the NFO/CTO membrane. This suggests membrane degradation in the presence of $SO_{2,}$ which will be analyzed in the next section.

In this study, the CMO/CTO dual-phase membrane permeation in air at 850 ºC was 0.21 mL·min^{-1}·cm^{-2}. This permeation value is very close to the standard values in dual-phase membranes at these temperatures with this thickness (around 600 μm) (Table 4. 9)[4]. Furthermore, under CO_2 environments, this CMO/CTO exhibits the highest permeation flux with 0.25 mL·min^{-1}·cm^{-2} with pure CO_2 in the sweep chamber. In addition, the oxygen permeation of this membrane in such environments is very stable over time. These results illustrate that CMO/CTO composites are promising candidates for OTMs in oxycombustion processes operating in high-CO_2 environments, especially if compared with state-of-the-art materials [4], see Table 4. 9.

Table 4. 9. Oxygen permeation results from dual-phase MIEC membranes at 850 ºC with inert gas (He and Ar) and CO_2. All the membranes have a thickness (*L*) between 500-700 μm. Extracted from[4].

Materials	***L*** **(μm)**	***JO₂*** **(mL·min⁻¹·cm⁻²)**	***T*** **(ºC)**	**Atm.** $\frac{pO_2^{feed}}{pO_2^{sweep}}$	**Ref.**
$Ce_{0.9}Gd_{0.1}O_{2-\delta}$ - $Ba_{0.5}Sr_{0.5}Co_{0.8}Fe_{0.2}O_{3-\delta}$	500	0.8	875	Air/He	22
	500	0.2	875	Air/CO_2	
$Ce_{0.8}Nd_{0.2}O_{2-\delta}$ - $Nd_{0.5}Sr_{0.5}Fe_{0.8}Al_{0.2}O_{3-\delta}$	600	0.25	850	Air/He	23
	600	0.1	850	Air/CO_2	
$Ce_{0.9}Pr_{0.1}O_{2-\delta}$ - $Pr_{0.6}Sr_{0.4}Fe_{0.99}Bi_{0.01}O_{3-\delta}$	600	0.15	850	Air/He	24
	600	0.05	850	Air/CO_2	
$Ce_{0.8}Tb_{0.2}O_{2-\delta}$ -$NiFe_2O_4$ + Pr_6O_{11}	680	0.13	850	Air/Ar	3
	680	0.13	850	Air/CO_2	
$Ce_{0.8}Tb_{0.2}O_{2-\delta}$ - Co_2MnO_4	679	0.22	850	Air/Ar	This study
	679	0.25	850	Air/CO_2	

Therefore, the CMO/CTO dual-phase material has a good oxygen permeation rate and is stable in CO_2 environments but low concentrations of SO_2 will poison the membrane. The second part of the oxygen permeation study was focused under reducing atmospheres in the sweep chamber (10%CH_4 in Ar). Figure 4. 10 shows the results for this experiment, where flows for sweep side and feed side are 150 and 100 mL·min^{-1} respectively,

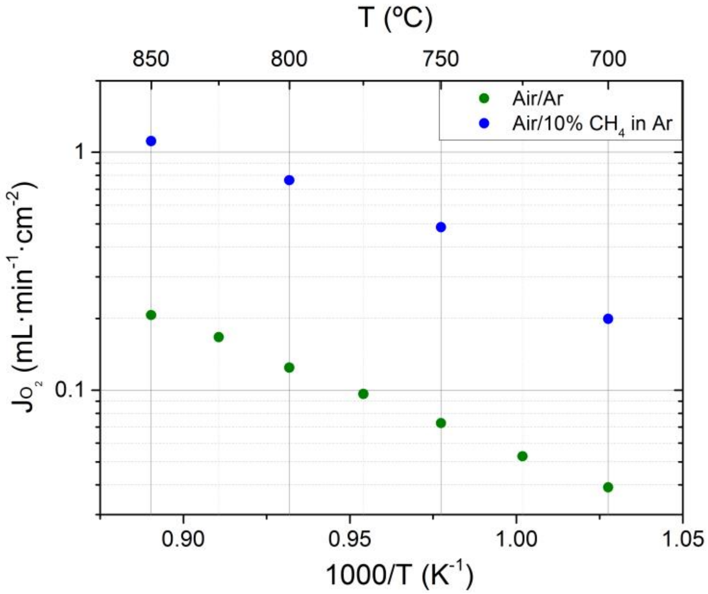

Figure 4. 10. Oxygen permeation studies for reducing atmospheres at the sweep side (10% of methane in argon). Membrane thickness 684 μm.

As can be seen in Figure 4.10a, the oxygen permeation increases almost one order of magnitude in reducing atmospheres compared with argon sweeping, Figure 4. 10a. This is mainly due to the sweep side with 10% CH_4 in argon has a pO_2 in the order of 10^{-15} bar. This pO_2 is much lower than pure argon $pO_2 >> 10^{-5}$ bar. At 850 ºC in 10% methane the oxygen permeations achieve 1.11 mL·min^{-1}·cm^{-2}, which is five times higher than in argon, 0.21 mL·min^{-1}·cm^{-2}. This increase in the oxygen permeation not only could come from the increase in the partial pressure gradient. Some reduction of the CMO could be happening, increasing its electronic conductivity and thus improving the oxygen permeation.

4.6. Post mortem characterization

After the oxygen permeation studies, both membranes were characterized by XRD comparing the ICSD patterns for both phases and the fresh membrane, represented in Figure 4. 11.

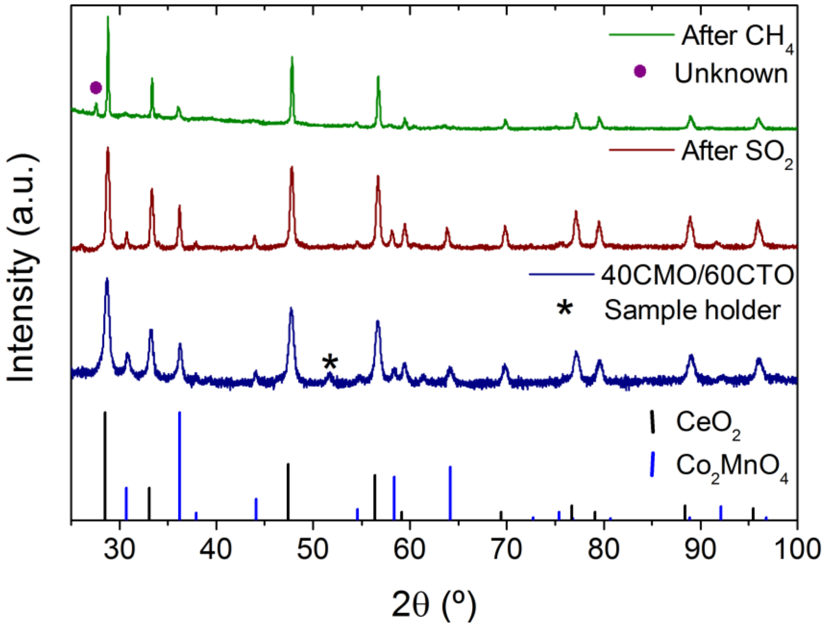

Figure 4. 11. XRD for CMO/CTO before (bottom) and after the stability test performed with SO_2 (top).

Here, the membrane was compared before the permeation test and after exposure to SO_2 during the oxygen permeation test. From the XRD patterns, neither structural changes nor the presence of secondary phases or impurities could be ascertained. As seen in Figure 4. 9b, the oxygen flux of the CMO/CTO membrane dropped progressively with time on the SO_2 (250 ppm) stream. Even so, when the SO_2 is removed, the permeation flux increases again but does not recover the initial flux (Figure 4. 9). In order to assess possible structural degradations, the side of the membrane exposed to the SO_2 environment was analyzed by SEM (Figure 4. 11).

For the CMO/CTO membrane operated under low pO_2 atmospheres (10% CH_4 in Ar), the X-ray diffractogram shown a degradation over the CMO phase and it was observed a new peak in the XRD pattern that it could not be identify. In these experiments, the oxygen permeation under these conditions in the sweep chamber was translated to very high oxygen permeation rates (more than 1 $mL \cdot min^{-1} \cdot cm^{-2}$). After these environments, the membrane did not appear to be permanently affected by the presence of these atmospheres. This membrane was also analyzed by SEM to identify the impurity observed in the XRD pattern.

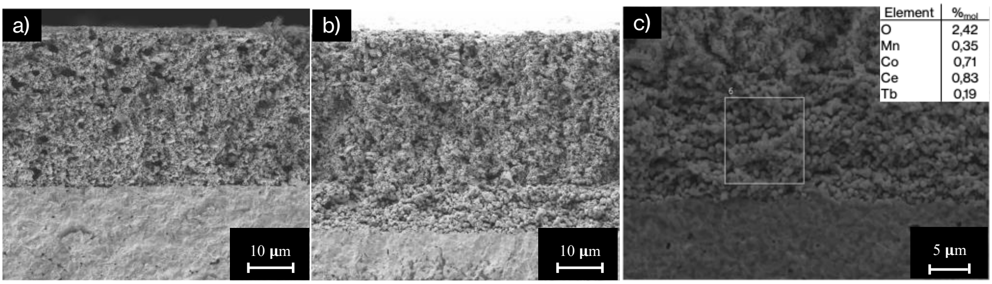

Element	$\%_{mol}$
O	2,42
Mn	0,35
Co	0,71
Ce	0,83
Tb	0,19

Figure 4. 12. Cross-section image from SEM of the CMO/CTO membrane after CO_2 and SO_2 stability test: **a)** catalytic layer from the feed side (air); **b)** catalytic layer from the sweep side (CO_2 and SO_2); **c)** EDS SEM analysis for part of the degraded area after being exposed to SO_2 environments.

Figure 4. 12 shows SEM cross-section images of both sides of the membrane after the SO_2 treatment, revealing microstructural evolution. As expected, the catalytic layer and the membrane on the feed side (air) were in good condition, Figure 4. 12a, with a thickness of around 30-25 µm. However, microstructural changes can be inferred on the sweep side, Figure 4. 12b. The catalytic layer seems unaltered, but a new porous layer appeared in the top part of the membrane, with a thickness of almost 10 µm. This porosity was seen before by Garcia-Fayos et al. on the NFO/CTO membrane after exposure to SO_2 [6]. One possible explanation for this

morphological change is the reaction between the SO_2 and the doped ceria. Several studies have revealed the CeO_2 in the presence of SO_2 and O_2 forms of $Ce_2(SO_4)_3$ [25,26]. This poisoning increases with the oxygen content, which could explain the constant decrease of oxygen permeation in the presence of SO_2 and O_2. The $Ce_2(SO_4)_3$ formed could block the active sites (oxygen vacancies), decreasing the permeation with the increase of $Ce_2(SO_4)_3$ into the doped ceria. The porosity on the membrane will be formed in the transition between $Ce_2(SO_4)_3$ and CeO_2 after the exposition to SO_2. However, $Ce_2(SO_4)_3$ could not be detected with the XRD equipment used for this study. The degraded zone was also analyzed with EDS, and sulfur could not be detected, Figure 4. 12c. Thus, although the formation of cerium sulfate seems the most probable reason for the membrane degradation, we could not corroborate its presence with the physicochemical characterization performed here.

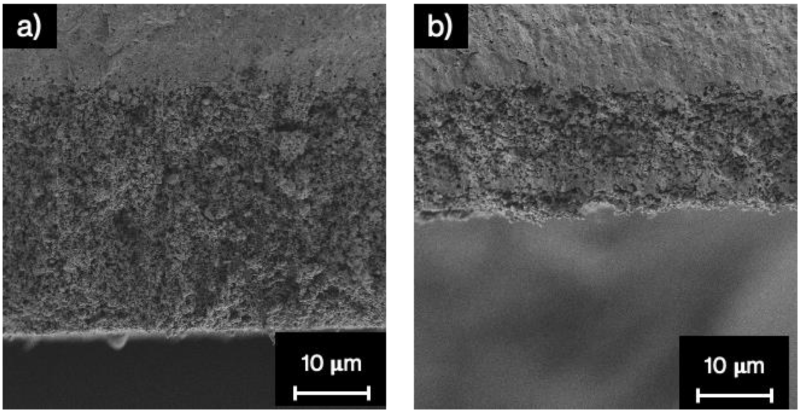

Figure 4. 13. Cross-section image from SEM of the CMO/CTO membrane after oxygen permeation test under CH_4: a) catalytic layer from the feed side (air); b) catalytic layer from the sweep side (10% methane in argon).

The CMO/CTO membrane exposed under CH_4 environments was also analyzed by scan electron microscopy (SEM), Figure 4. 13. As in the other membrane, the catalytic layer and the membrane on the feed side were in good condition, Figure 4. 13a. The catalytic layer on the air side also has a thickness around 30-25 µm as it was expected. However, the side under methane conditions was different, Figure 4. 13b. As can be noticed, more than 10 μm of thickness on the catalytic layer was lost. The CMO spinel could be reduced under methane environments and then sintered, decreasing the porosity and the thickness of the catalytic layer.

4.7. Conclusions.

The use of Co_2MnO_4 spinel as the electronic phase in composite membranes was assessed. Here, we proved that the higher electronic conductivity of CMO with respect to the well-studied spinel ($NiFe_2O_4$, NFO) enables to boost the oxygen transport in these dual-phase membranes. Namely, the increase of the total conductivity for the dual-phase membrane (CMO/CTO) leads to higher oxygen-permeation flux values with respect to NFO/CTO membranes, e.g., 0.22 $mL \cdot min^{-1} \cdot cm^{-2}$ and 0.11 $mL \cdot min^{-1} \cdot cm^{-2}$ at 850 ºC under air/Ar, respectively. Furthermore, the CMO/CTO membrane exhibits the highest permeation in CO_2 environments compared to literature and excellent stability during prolonged time, 0.24 $mL \cdot min^{-1} \cdot cm^{-2}$ and 0.13 $mL \cdot min^{-1} \cdot cm^{-2}$ for CMO/CTO and NFO/CFO membranes, respectively. This oxygen permeation is the highest for this membrane (> 600 μm-thick) obtained in CO_2 environments[4]. The SO_2-driven membrane poisoning was more evident than in previous studies for similar dual-phase membranes due to its increase in oxygen permeation compared to that study [6]. In addition, similar surface-morphology evolution on the membrane was detected, but any presence of sulfur elements was inferred in the post-mortem characterization. This study illustrates that CMO/CTO composites could be a promising candidate for OTMs or oxygen electrodes in CO_2-capture-enabling oxycombustion processes.

The permeation for the CMO/CTO membrane under methane environments was significantly high, producing up to 1.11 $mL \cdot min^{-1} \cdot cm^{-2}$ of O_2. Despite the stability test showing the membrane was stable in such environments, post-mortem SEM images confirmed a degradation on the catalytic layer.

4.8. Bibliography.

1. Solís, C. *et al.* Mixed Ionic–Electronic Conduction in NiFe 2 O 4 –Ce 0.8 Gd 0.2 O 2− δ Nanocomposite Thin Films for Oxygen Separation. *ChemSusChem* **11**, 2818–2827 (2018).

2. Balaguer, M., García-Fayos, J., Solís, C. & Serra, J. M. Fast Oxygen Separation Through SO 2 - and CO 2 -Stable Dual-Phase Membrane Based on NiFe 2 O 4 –Ce 0.8 Tb 0.2 O 2-δ. *Chemistry of Materials* **25**, 4986–4993 (2013).

3. García-Fayos, J., Ruhl, R., Navarrete, L., Bouwmeester, H. J. M. & Serra, J. M. Enhancing oxygen permeation through Fe2NiO4-Ce0.8Tb0.2O2-δ composite membranes using porous layers activated with Pr6O11 nanoparticles. *J Mater Chem A Mater* **6**, 1201–1209 (2018).

4. Kiebach, R. *et al.* A review on dual-phase oxygen transport membranes: from fundamentals to commercial deployment. *J Mater Chem A Mater* **10**, 2152–2195 (2022).

5. Petric, A. & Ling, H. Electrical conductivity and thermal expansion of spinels at elevated temperatures. *Journal of the American Ceramic Society* **90**, 1515–1520 (2007).

6. Garcia-Fayos, J., Balaguer, M. & Serra, J. M. Dual-Phase Oxygen Transport Membranes for Stable Operation in Environments Containing Carbon Dioxide and Sulfur Dioxide. *ChemSusChem* **8**, 4242–4249 (2015).

7. Balaguer, M., Solís, C. & Serra, J. M. Structural-transport properties relationships on Ce 1- xLn xO 2-δ system (Ln = Gd, La, Tb, Pr, Eu, Er, Yb, Nd) and effect of cobalt addition. *Journal of Physical Chemistry C* **116**, 7975–7982 (2012).

8. Hua, B. *et al.* The Electrical Property of MnCo2O4 and its Application for SUS 430 Metallic Interconnect. *Chinese Science Bulletin* **55**, 3831–3837 (2010).

9. Bredikhin, S. I. *et al.* Protective coatings based on Mn-Co spinel for current collectors of solid oxide fuel cells. *Russian Journal of Electrochemistry* **45**, 520–526 (2009).

10. Ran, K. *et al.* The in situ generated emerging phase inside dual phase oxygen transport membranes. *Acta Mater* **234**, 118034 (2022).

11. Joo, J. H. *et al.* Dramatically enhanced oxygen fluxes in fluorite-rich dual-phase membrane by surface modification. *Chemistry of Materials* **26**, 4387–4394 (2014).

12. Šutka, A. & Gross, K. A. Spinel ferrite oxide semiconductor gas sensors. *Sens Actuators B Chem* **222**, 95–105 (2016).

13. Solís, C., Somacescu, S., Palafox, E., Balaguer, M. & Serra, J. M. Particular Transport Properties of $NiFe_2O_4$ Thin Films at High Temperatures. *The Journal of Physical Chemistry C* **118**, 24266–24273 (2014).

14. Zaouali, A. *et al.* High electrical conductivity at room temperature of MnCo2O4 cobaltite spinel prepared by sol–gel method. *Journal of Materials Science: Materials in Electronics* **32**, 1221–1232 (2021).

15. Sunarso, J. *et al.* Mixed ionic-electronic conducting (MIEC) ceramic-based membranes for oxygen separation. *Journal of Membrane Science* vol. 320 13–41 Preprint at https://doi.org/10.1016/j.memsci.2008.03.074 (2008).

16. Laqdiem, M., Garcia-Fayos, J., Almar, L., Balaguer, M. & Serra, J. M. The role of ionic-electronic ratio in dual-phase catalytic layers for oxygen transport permeation membranes. *J Memb Sci* 121578 (2023) doi:10.1016/j.memsci.2023.121578.

17. Li, P. *et al.* Enhanced electrochemical redox kinetics of La0.6Sr0.4Co0.2Fe0.8O3 in reversible solid oxide cells. *Electrochim Acta* **446**, (2023).

18. Almar, L., Szász, J., Weber, A. & Ivers-Tiffée, E. Oxygen Transport Kinetics of Mixed Ionic-Electronic Conductors by Coupling Focused Ion Beam Tomography and Electrochemical Impedance Spectroscopy. *J Electrochem Soc* **164**, F289–F297 (2017).

19. Almar, L. *et al.* Improved Phase Stability and CO2 Poisoning Robustness of Y-Doped Ba0.5Sr0.5Co0.8Fe0.2O3-δ SOFC Cathodes at Intermediate Temperatures. *ACS Appl Energy Mater* **1**, 1316–1327 (2018).

20. Yi, E.-J., Yoon, M.-Y., Moon, J.-W. & Hwang, H.-J. Fabrication of a MnCo2O4/gadolinia-doped Ceria (GDC) Dual-phase Composite Membrane for Oxygen Separation. *Journal of the Korean Ceramic Society* **47**, 199–204 (2010).

21. Catalán-Martínez, D., Santafé-Moros, A., Gozálvez-Zafrilla, J. M., García-Fayos, J. & Serra, J. M. Characterization of oxygen transport phenomena on BSCF membranes assisted by fluid dynamic simulations including surface exchange. *Chemical Engineering Journal* **387**, 124069 (2020).

22. Xue, J., Liao, Q., Wei, Y., Li, Z. & Wang, H. A CO2-tolerance oxygen permeable 60Ce0.9Gd0.1O2-δ-40Ba0.5Sr0.5Co0.8Fe0.2O3-δ dual phase membrane. *J Memb Sci* **443**, 124–130 (2013).

23. Partovi, K., Bittner, M. & Caro, J. Novel CO2-tolerant Al-containing membranes for high-temperature oxygen separation. *J Mater Chem A Mater* **3**, 24008–24015 (2015).

24. Zhang, C. *et al.* Effects of bi substitution on the cobalt-free 60wt.%ce0.9pr0.1o2−δ-40wt.%pr0.6sr0.4fe1−xbixo3−δ oxygen transport membranes. *Processes* **9**, (2021).

25. Rodriguez, J. A. *et al. Interaction of SO 2 with CeO 2 and Cu/CeO 2 catalysts: photoemission, XANES and TPD studies*. *Catalysis Letters* vol. 62 (1999).

26. Smirnov, M. Y. *et al.* Interaction of Al 2O 3 and CeO 2 Surfaces with so 2 and so 2 + O 2 studied by X-ray photoelectron spectroscopy. *Journal of Physical Chemistry B* **109**, 11712–11719 (2005).

5.

LOWERING OPERATION TEMPERATURE IN OXYGEN TRANSPORT MEMBRANE REACTORS (OTMR) BY MEMBRANE ELECTRIFICATION

5. Lowering operation temperature in oxygen transport membrane reactors (OTMR) by membrane electrification

5.1. Catalytic membrane reactors based on oxygen transport membranes.

The decarbonization of the industry has become an important strategy to transition to a safe climatic future [1,2]. Developing highly efficient and sustainable new chemical production routes is essential to decrease the carbon footprint of actual processes. Oxidative and selective reactions using pure oxygen, like CO_2-capture-enabling oxy-combustion or oxidative dehydrogenation of paraffins, have been extensively studied [3–7]. In this matter, oxygen production will take an important role, and it is essential to develop new technologies that are more efficient and flexible to achieve these new challenges [3,8–11].

In this matter, Oxygen transport membranes (OTMs) emerge as an alternative technology to produce pure oxygen, allowing it to be integrated into current industrial processes presenting residual heat streams [12,13]. For OTMs materials, $Ba_{0.5}Sr_{0.5}Co_{0.8}Fe_{0.2}O_{3-\delta}$ (BSCF)-based membranes have been studied as catalytic membrane reactors for several relevant reactions to produce hydrocarbon fuels and chemicals [6,14–18], such as oxygen coupling of methane (OCM), partial oxidation of methane (POM), water splitting, oxidative dehydrogenation of ethane (ODHE), etc. ODHE technology has gained industrial interest, driven by the increasing global ethylene demand (precursor of polyethylene, ethylene oxide, and ethylbenzene), with expectations of ethylene production reaching almost 200 megatons by 2026[19].

Currently, worldwide ethylene production comes from other sources like methane, naphtha, liquefied petroleum gas, etc. In fact, the steam cracking of naphtha represents more than 40% of the ethylene production [20]. From ethane feedstock, the main ethylene production route is the thermal cracking of ethane, achieving yields close to 60 and 70% [5]. Even so, thermal cracking has several issues regarding the deactivation through coke formation and the necessity of high operation temperatures (800-900 °C) [19]. Nevertheless, new technologies like protonic ceramic cells are being studied for the thermal cracking of ethane, displacing the equilibrium at lower temperatures [21–23]. Another approach is oxidative dehydrogenation of ethane (ODHE), which could be an alternative to this process, Eq. 5. 1. In the ODHE process, the coke formation is reduced thanks to the presence of oxygen, and it can be realized in a broad temperature range (300-900 °C) [6,7,19,24–27]. These advantages make this technology a more efficient and sustainable process with potential for industrial deployment. However, several secondary reactions can occur in the presence of oxygen and higher temperatures, decreasing the ethylene yield in the global process, Eq. 5. 2 to Eq. 5. 6 [28].

$$C_2H_6 + 0.5O_2 \rightleftarrows C_2H_4 + H_2O \qquad \Delta H^0 = -105.50\ kJ/mol \qquad \text{Eq. 5. 1}$$

$$C_2H_4 + 2O_2 \rightarrow 2CO + 2H_2O \qquad \Delta H^0 = -757.21\ kJ/mol \qquad \text{Eq. 5. 2}$$

$$C_2H_6 \rightleftarrows C_2H_4 + H_2 \qquad \Delta H^0 = 136.33\ kJ/mol \qquad \text{Eq. 5. 3}$$

$$C_2H_4 + 2H_2O \rightleftarrows 2CO + 4H_2 \qquad \Delta H^0 = 210.07\ kJ/mol \qquad \text{Eq. 5. 4}$$

$$CO + H_2O \rightleftarrows CO_2 + H_2 \qquad \Delta H^0 = -41.16\ kJ/mol \qquad \text{Eq. 5. 5}$$

$$CO + 0.5O_2 \rightarrow CO_2 \qquad \Delta H^0 = -282.98\ kJ/mol \qquad \text{Eq. 5. 6}$$

When oxygen is supplied to the ethane dehydrogenation reaction, controlling the O_2/C_2H_6 ratio is essential to avoid a secondary reaction [6,19]. For fixed bed reactors, the oxygen is co-fed with the ethane, leading to several secondary reactions, reducing the ethylene selectivity (Figure 5. 1a) while the inlet O_2/C_2H_6 ratio is maintained out of flammability/explosion limits. Several chemical-looping technologies have been developed to reduce the inlet O_2/C_2H_6 ratio, where the redox catalyst in situ releases the oxygen (Figure 5. 1b) [19,24,29]. Here, a promising alternative to control de O_2/C_2H_6 is an integrated membrane reactor based on Mixed Ionic and Electronic Conductors (MIEC) to control oxygen injection along the reaction chamber (Figure 5. 1c) [6,30–32]. In both CMRs based on OTM and chemical looping reactor, the addition of oxygen is highly distributed, achieving low ratios of O_2/C_2H_6. OTMs are made of ceramic MIEC materials, and the oxygen permeation increases exponentially with temperature, reaching optimal permeation values at high temperatures, around 800 °C and 900 °C [6,31,32]. As mentioned before, ODHE reaction improves the selectivity of ethylene at low temperatures, so decreasing the reactor temperature in CMRs could be the key to enhancing ethylene's selectivity for OTM as catalytic membrane reactors in ODHE reaction.

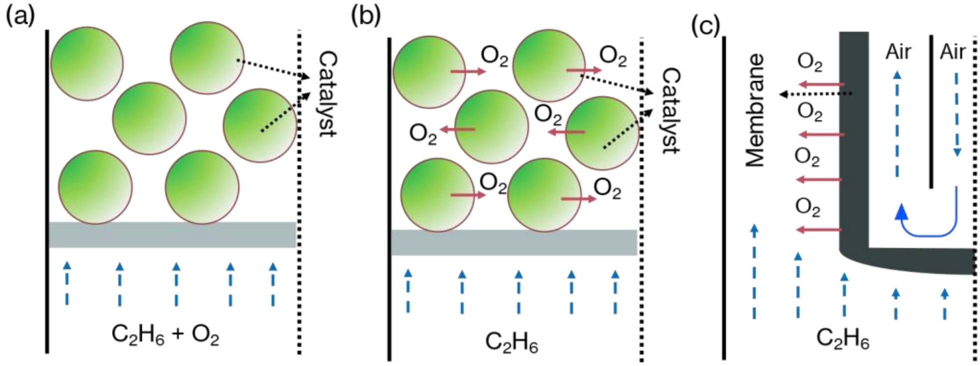

Figure 5. 1. Oxidative dehydrogenation of ethane reactors by using different modes of O_2 addition: a) Co-feeding of oxygen and C_2H_6 in a fixed bed reactor; b) Feeding oxygen through the reduction of the catalyst in a chemical looping reactor; c) Feeding oxygen through an OTM in a catalytic membrane reactor.

This study focuses on the electrification of OTMs to heat the membrane surface locally and thus maintaining an intermediate temperature in the reactor chamber. As mentioned before, the main property of OTMs is their mixed ionic and electronic conductivity [4,33]. BSCF (MIEC material selected for this study) shows a total conductivity of 30 $S\cdot cm^{-1}$ in air at 650 °C [34–36]. Applying a voltage difference on a BSCF sample leads to the appearance of an electric current that dissipates energy in the form of heat, commonly known as the Joule effect. This increase in the membrane temperature gives rise to an increased oxygen permeation while maintaining the reactor chamber at lower temperatures. Here, the surface-membrane temperature was controlled (up to 900 °C) by applying different voltages, regulating the oxygen permeation flux, while the reactor chamber was preserved at a lower temperature, e.g., 650 °C. Further, the study shows that the new operation regime enabled by the developed electrified-BSCF membrane reactor ameliorates the catalytic ODHE performance, reaching higher ethylene yield than the non-electrified CMR.

5.2. Electrified OTM concept, device and calculations.

The scheme for the Joule effect OTM device is shown in Figure 5. 2. Here, Figure 5. 2a represents the scheme of the *electrified*-BSCF catalytic membrane reactor (e-CMR). In order to apply voltage to the capillary membrane, gold wires were connected at the ends of the catalytic layer. To control the membrane temperature (T_M) accurately, a thermocouple was attached to its surface, as indicated in Figure 5. 2b. In contrast, an additional thermocouple is located in the middle of the reactor chamber (T_R), as shown in Figure 5. 2a. For the non-electrified membrane, the oxygen permeation depends only on the reactor temperature (Figure 5. 2c). In the case of the electrified membrane, the application of voltage will produce local heating of the membrane, and the oxygen permeation will increase. With this technique, a maximum temperature of 900 °C on the membrane surface is obtained, whereas the reactor chamber is maintained at 650 °C (Figure 5. 2d).

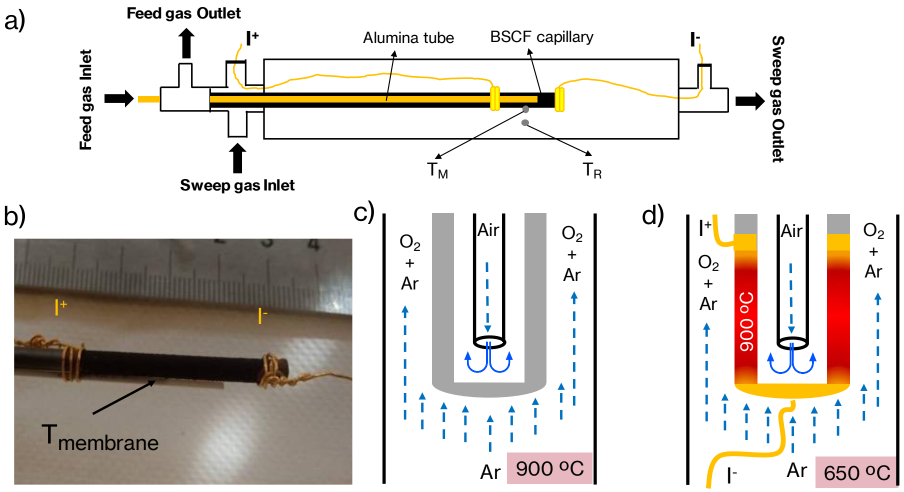

Figure 5. 2. **a)** BSCF catalytic membrane reactor electrified device; **b)** current gold wires connections and the temperature measurement of the membrane; **c)** Scheme of the non-electrified BSCF capillary membrane; **d)** Scheme of the Joule effect through the BSCF capillary membrane.

For the oxygen permeation studies, the gas flow rate for both chambers, sweep (Ar) and feed (synthetic air), was 150 mL·min^{-1}. In the case of the ODHE reaction study, 400 mL·min^{-1} of a mixture of 10% ethane in Ar and 150 mL·min^{-1} of synthetic air were fed to the sweep and feed chamber, respectively. All the tests, permeation, and reaction were conducted at atmospheric pressure. In order to electrify, i.e., locally heat, the BSCF membrane, different electric voltages were applied for 60 min for both oxygen permeation and ODHE reaction experiments. Inlet gas streams were individually mass-flow controlled. The temperature was measured by two K-type thermocouples attached, one close to the membrane (T_M) and the other in the sweep chamber (T_R). Voltage was applied to the membranes by using a Keysight E36200 Series power supply. The Micro-GC was calibrated with a gas mixture of 11 compounds (Linde): 2% CH_4, 9% H_2, 9% CO, 1% CO_2, 1% C_2H_4, 2% C_2H_6, 1% C_3H_8, 1% C_3H_6, 1% C_3H_4, 1% C_4H_6 in N_2. To calculate the conversion and the different selectivities obtained, the carbon balance was calculated:

$$2n_{C_2H_{6,in}} = 2\left(n_{C_2H_{6,out}} + n_{C_2H_4}\right) + n_{CO_2} + n_{CO} + 3\left(n_{C_3H_8} + n_{C_3H_6} + n_{C_3H_4}\right) + 4n_{C_{4+}} + n_{Coke}$$

Eq. 5. 7

Where n_{Ci} is the molar rate (mol·min^{-1}) for each compound obtained at the outlet of the CMR. The initial ethane was measured bypassing the catalytic membrane reactor, and coke formation was obtained from the carbon balance (Eq. 5. 7). Ethane conversion (X_{C2H6}), product selectivity (S_{Ci}), and ethylene yield (Y_{C2H4}) was calculated by using the Eq. 5. 8, 5. 9 and 5. 10.

$$X_{C_2H_6} = \left(1 - \frac{2n_{C_2H_{6,out}}}{2n_{C_2H_{6,in}}}\right) \cdot 100$$ Eq. 5. 8

$$S_{C_i} = \left(\frac{i \cdot n_{C_i}}{2\left(n_{C_2H_{6,in}} - n_{C_2H_{6,out}}\right)}\right) \cdot 100$$ Eq. 5. 9

$$Y_{C_2H_4} = X_{C_2H_6} \cdot S_{C_2H_4}/100$$ Eq. 5. 10

The oxygen permeation under ODHE reaction was calculated by using the hydrogen (Eq. 5. 11) and the oxygen balances (Eq. 5. 12). Water formation can be obtained from the hydrogen balance that, in addition, allows to get the oxygen balance and subsequently, to calculate the oxygen permeation during the ODHE reaction.

Hydrogen balance:

$$6n_{C_2H_{6,in}} = 6n_{C_2H_{6,out}} + 4n_{C_2H_4} + 8n_{C_3H_8} + 6n_{C_3H_6} + 4n_{C_3H_4} + 4n_{CH_4} + 6n_{C_4H_6} + 2n_{H_2} + 2n_{H_2O}$$ Eq. 5. 11

Oxygen balance:

$$2n_{O_{2,perm}} = 2n_{O_{2,out}} + 2n_{CO_2} + n_{CO} + n_{H_2O}$$ Eq. 5. 12

Thermodynamic simulations for ODHE were performed using the software package HSC Chemistry 6.1 from Outotec Research Oy. To obtain the equilibrium composition of the reactions, minimization of Gibbs free energy was employed.

5.3. BSCF capillary membranes characterization.

The XRD analysis of BSCF capillary membranes (Figure 5. 3a) shows a single cubic perovskite phase; no secondary phases are detectable [37,38]. The microstructure of the catalytic layers was studied by SEM analysis of the cross-section. The BSCF catalytic layer has a thickness of around 20-30 µm and presents an adequate porosity, as shown in Figure 5. 3b. The CTO catalytic layer presents a lower thickness, about 10-15 µm, and a lower particle size than the BSCF catalytic layer (Figure 5. 3c).

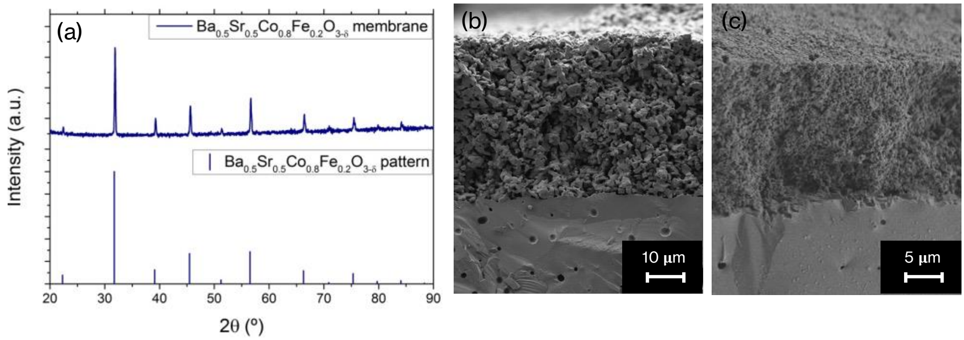

Figure 5. 3. a) XRD pattern for the commercial BSCF capillary membrane, BSCF pattern from ICSD- I257399; Cross-section SEM image of the BSCF membrane coated **b)** with BSCF and **c)** with CTO catalytic layers.

5.4. Oxygen permeation studies

First, the influence of the measurement configuration, sweep inside or outside the BSCF-activated capillary membrane, on the O_2 permeation flux was evaluated, Figure 5. 4. At temperatures above 750 °C, lightly lower oxygen flows are obtained when the sweep is fed inside of the capillary, achieving 3.6 $mL \cdot min^{-1} \cdot cm^{-2}$ at 900

°C whereas 3.9 mL·min^{-1}·cm^{-2} is reached when the sweep side is fed in the outer chamber. These oxygen permeation values are similar to other BSCF tubular membranes [39,40]. This behavior could be ascribed to the absence of a catalytic layer inside the membrane, as the surface exchange reactions on the sweep side are more affected than on the feed side [41,42]. At lower temperatures, the surface exchange reactions are less limited, and both configurations present similar values [41,42].

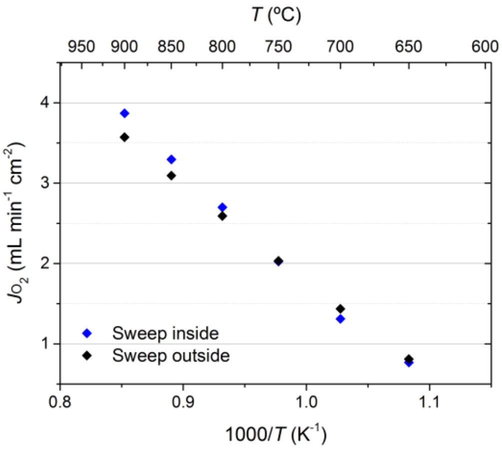

Figure 5. 4. Oxygen permeation through the surface-activated BSCF capillary membrane as a function of temperature for two different configurations: sweep fed inside (blue points) and outside (black points).

The electrification of the system has been introduced using voltage pulses of 1 hour (30 minutes at low voltage, from 1 V to 5 V). After these peaks, the voltage was turned off in order to evaluate possible degradation. The results in Figure 5. 5a do not show degradation as a consequence of the electrification reaching the exact value of the oxygen permeation than before applying any potential. Further, the oxygen permeation and the temperature of the membrane increase gradually with the applied potential. Stable measurements could be observed when the potential is applied (both permeation and temperature). Figure 5. 5b compares the oxygen fluxes obtained in the conventional permeation test with the electrified measurement as a function of the reactor temperature. As voltage is applied to the membrane, it heats up, and the O_2 fluxes obtained are consistent with those obtained for the non-electrified permeation. Then, by applying 9 V (resulting in 33 W), the temperature in the membrane increases from 650 °C to 897 °C, reaching a flux of 3.7 $mL \cdot min^{-1} \cdot cm^{-2}$. The same protocol was followed by changing the configuration, i.e., the sweep is fed in the inner chamber. In this configuration, the O_2 flux values (Figure 5. 5c) are lower than the corresponding non-electrified process for the same membrane temperature, reaching 3.2 $mL \cdot min^{-1} \cdot cm^{-2}$. All the results for both configurations are represented in Table 5. 1. Also, the power supply in both electrified configurations is compared in Figure 5. 5d, giving rise to the same temperatures for both configurations. From this, it can be inferred that the gas configuration only affects the oxygen permeation values due to the position of the catalytic layer [42].

Table 5. 1. Membrane temperature and oxygen permeation for a BSCF-coated capillary membrane electrified at different voltages.

	Current applied									
Voltage (V)	0	1	2	3	4	5	6	7	8	9
Sweep outside configuration										
I (A)	-	0.41	0.81	1.21	1.62	2.04	2.48	2.93	3.17	3.66
Power (W)	-	0.41	1.62	3.62	6.48	10.2	14.9	20.5	25.3	32.9
T_{mem} (°C)	650	656	670	694	722	756	793	831	850	897
J_{O_2} ($mL \cdot min^{-1} \cdot cm^{-2}$)	0.74	0.79	0.93	1.19	1.56	2.02	2.54	3.02	3.32	3.74
Sweep inside configuration										
I (A)	-	0.29	0.59	0.93	1.30	1.74	2.18	2.69	3.18	3.68
Power (W)	-	0.29	1.18	2.80	5.20	8.60	13.1	18.8	25.4	33.1
T_{mem} (°C)	650	654	664	682	706	740	776	817	858	898
J_{O_2} ($mL \cdot min^{-1} \cdot cm^{-2}$)	0.81	0.88	0.98	1.22	1.53	1.81	2.24	2.64	2.95	3.20

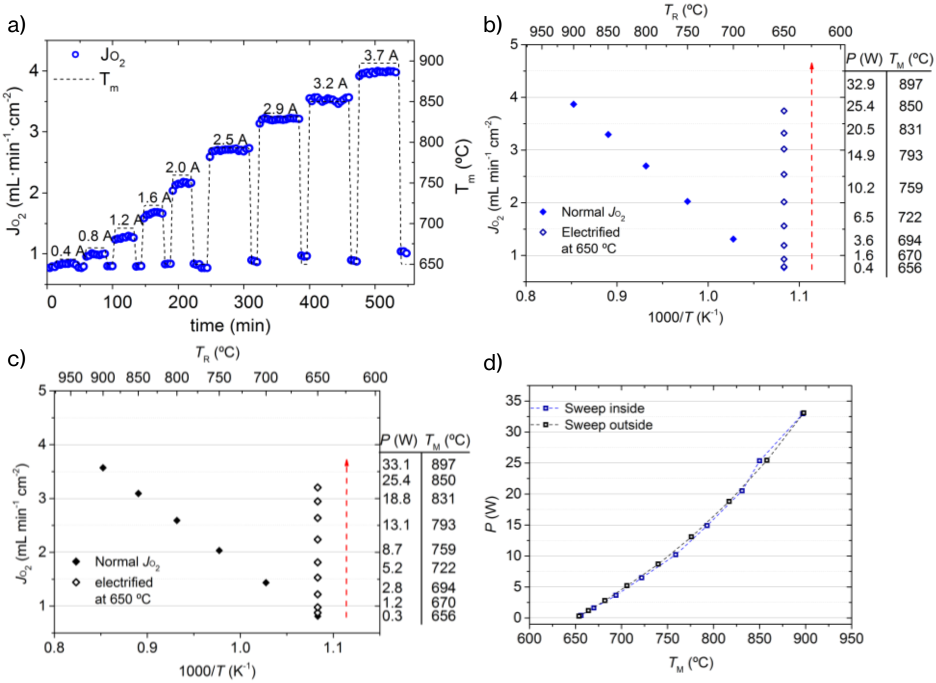

Figure 5. 5. Configuration sweep outside: a) Oxygen permeation and membrane temperature for different power applied at 650 °C; **b)** Oxygen permeation for an electrified and non-electrified BSCF membrane at different temperatures; **Sweep inside configuration: c)** Oxygen permeation for an electrified and non-electrified BSCF membrane at different temperatures; **d)** Power supply on the membrane and the membrane temperature reached for both configurations.

So far, the feasible voltage-driven control of the membrane -surface temperature – and associated O_2 flux- was demonstrated in the *electrified mode*. This BSCF electrified membrane reached 900 °C while the outer reaction chamber remained at 650 °C. In the following, the long-term stability of these electrified membranes under working conditions is assessed.

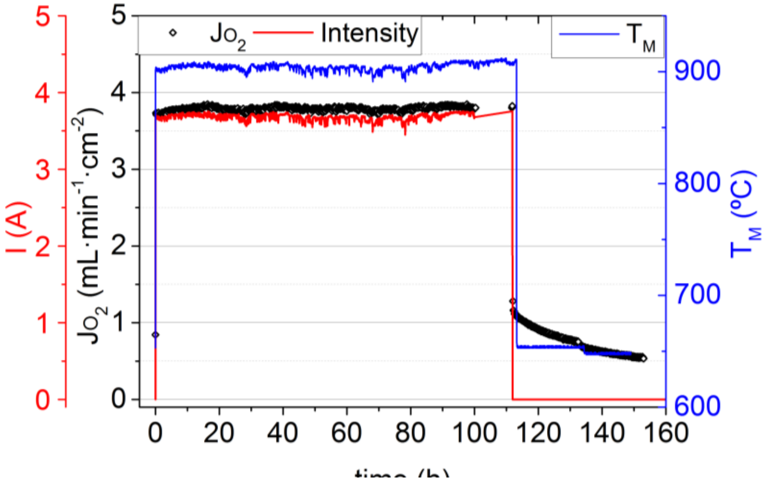

Figure 5. 6. Oxygen permeation stability test in electrification mode for 110 h.

Evaluating the membrane robustness under *electrified mode* is especially relevant since the temperature gradient between the membrane surface and the reactor chamber could cause thermo-mechanical stress and eventually break the membrane[43]. The stability of the electrified membrane was studied by applying 9 V (3.7 A) for 110 h (Figure 5. 6). During the stability test, the temperature and current remained stable, resulting in a constant oxygen flux of 3.8 $mL \cdot min^{-1} \cdot cm^{-2}$ at 906 °C. After 110 h of operation, the application of voltage was stopped, leading to a decrease in both the voltage-induced membrane temperature and permeation flux. Namely, in the first measurement when the electric current was switched off, the oxygen flux was initially 1.2 $mL \cdot min^{-1} \cdot cm^{-2}$, which, interestingly, is higher than the one reached in the previous experiments at the same temperature, around 0.76 $mL \cdot min^{-1} \cdot cm^{-2}$ (Table 5. 1). From that point onwards, the oxygen permeation equilibrated until reaching a steady value of 0.55 $mL \cdot min^{-1} \cdot cm^{-2}$ after 40 h without voltage application. This effect can be related to the hexagonal phase formation in the BSCF structure [37,44,45]. The BSCF has two principal crystal perovskite structures, hexagonal (Space group $P6_3/mmc$) and cubic (P m-3m) structures [44,45]. The BSCF with cubic structure presents superior transport properties than the hexagonal structure. At 850-900 °C, the cubic structure is formed, but when the temperature decreases, i.e., when the electrical voltage is switched off, the hexagonal phase starts to grow [45]. Therefore, the oxygen flux drop is principally caused by the progressive formation of this hexagonal phase [45]. However, B-site doping with Y and Nb in BSCF can mitigate the formation of the hexagonal phase [46,47].

Despite the stable O_2 separation of the electrified BSCF-coated membrane when applying 3.7 A for 110 h, BSCF is not stable under CO_2 or reducing atmospheres such as CH_4. Therefore, applying protective layers under CO_2 environments, such as $Ce_{0.8}Gd_{0.2}O_{2-\delta}$ (CGO), to BSCF membranes can effectively mitigate the BSCF decomposition, as reported by C. Solis et al. [48]. In this work, a porous coating of $Ce_{0.8}Tb_{0.2}O_{2-\delta}$ (CTO) was selected to minimize the membrane degradation and increase the surface catalytic activity. This layer can also act as a catalytic layer due to the interesting electrochemical properties that the CTO possesses [49,50]. Then, the electrification of a BSCF capillary membrane functionalized with CTO was studied, and the main results are shown in Figure 5. 7 and Table 5. 2.

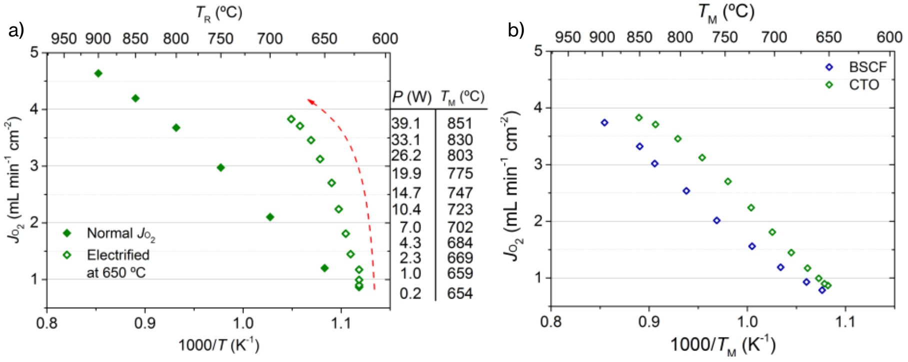

Figure 5. 7. a) Oxygen permeation for an electrified and non-electrified BSCF membrane with CTO layer as a function of the reactor temperature; **b)** Comparison of the oxygen permeation obtained with BSCF and CTO-coated capillary membranes as a function of the membrane voltage-induced temperature when voltage is applied (sweep is fed in the outer chamber in both membranes).

Table 5. 2. Membrane temperature and oxygen permeation for a CTO-coated capillary membrane electrified at different voltages.

	Current applied											
Voltage (V)	0	1	2	3	4	5	6	7	8	9	10	10.8
Sweep outside configuration												
I (A)	-	0.24	0.49	0.76	1.07	1.39	1.74	2.10	2.49	2.91	3.31	3.62
Power (W)	-	0.24	0.98	2.29	4.27	6.95	10.4	14.7	19.9	26.2	33.1	39.1
T_{mem} (°C)	651	654	659	669	684	702	723	747	775	803	830	851
J_{O_2} (mL·min^{-1}·cm^{-2})	0.87	0.90	1.00	1.17	1.45	1.81	2.24	2.70	3.12	3.46	3.71	3.83

Figure 5. 7a plots the oxygen permeation flux obtained with the membrane coated with CTO as a function of the reactor temperature for electrified and non-electrified modes. When the membrane is electrified, the voltage-induced membrane temperature increases and, subsequently, the oxygen flux. In this case, the maximum reached temperature in the membrane surface was 851 °C, and the corresponding oxygen flux was 3.8 mL·min^{-1}·cm^{-2}, lower than the obtained at 850 °C with the non-electrified membrane. CTO-coated membrane presents higher O_2 transport than BSCF-coated membrane when electrified, as observed in Figure 5. 7b, where the oxygen flux is plotted as a function of the voltage-induced temperature. Notably, the reached heating power for the CTO-coated membrane is higher than for the BSCF-coated membrane (Figure 5. 8), suggesting that higher local temperatures might be achieved in the BSCF bulk and the CTO catalytic porous layer presents better thermal insulation properties due to textural properties and the associated infrared radiation emissivity [51,52].

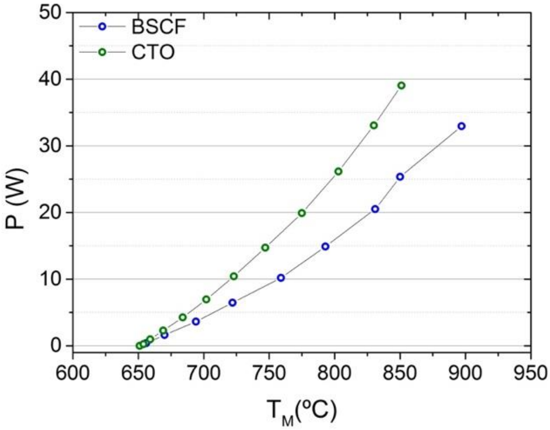

Figure 5. 8. Comparison of the power supply and the membrane temperature reached for BSCF and CTO-coated capillary membranes.

5.5. Oxidative dehydrogenation of ethane in BSCF catalytic membrane reactor

As mentioned above, the oxidative dehydrogenation of ethane (ODHE) is a relevant chemical process for ethylene production that has gained considerable attention in the last few years [19,27]. Considering the thermodynamic equilibrium, the O_2/C_2H_6 ratio and the reaction temperature are crucial to boosting the ethylene selectivity and the ethane conversion. Figure 5. 9a shows the ethane conversion and ethylene selectivity at the thermodynamic equilibrium for different temperatures and O_2/C_2H_6 ratios. These thermodynamic calculations confirm that increasing the temperatures and lowering the O_2/C_2H_6 ratios increases ethylene production. Figure 5. 9b displays the free Gibbs energy as a function of the temperature for the different possible reactions in the ODHE reactor. Partial oxidation of ethylene has the most negative energy value, indicating that at high oxygen concentration, the partial oxidation contribution will become very relevant. Also, the oxidation of CO is in the same order as the ODHE reaction, and steam reforming of ethylene also takes importance at high temperatures (>800 °C). To maximize ethylene yield, the O_2/C_2H_6 ratio has to be as low as possible, similar to pyrolysis conditions, limiting conventional catalytic ODHE technologies that use O_2 as a reactant to some extent. In this line, OTMs emerge as a potential technology to improve the ODHE process[6,30–32].

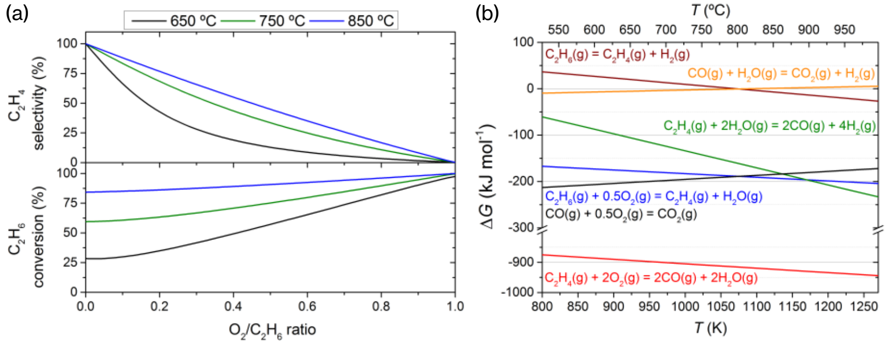

Figure 5. 9. a) Ethane conversion and ethylene selectivity at the equilibrium at different O_2/C_2H_6 ratios at 650 °C, 750 °C, and 850 °C; **b)** Gibbs free energy at different temperatures for the main reactions that can occur in the presence of O_2 and C_2H_6.

ODHE reaction was performed using two different membranes and four different experiments were carried out: BSCF-coated membrane heated at 650 °C ($BSCF_{650°C}$) and 850 °C ($BSCF_{850°C}$) and electrified BSCF- and CTO-coated membranes reaching a temperature of ~850 °C on the membrane surface while maintaining a temperature in the reactor chamber of 650 °C ($BSCF_{elect}$ and CTO_{elect}). Table 5. 3 shows the conditions for these four experiments and the oxygen permeation when ethane is fed into the reaction chamber. Here, it was also calculated the O_2/C_2H_6 total ratio and the initial ratio $\left(\frac{O_2}{C_2H_{6(in)}}\right)$, using the oxygen flux permeated and the 10% of the J_{O2} as the initial point of contact. The ethane feeding increases the oxygen-diffusion driving force between both chambers (lower pO_2 than Ar), increasing the oxygen flux. The O_2 permeation results and the explanation of the behavior under the different conditions are given in Figure 5. 10).

Table 5. 3. Oxygen permeation, reactor temperature, membrane temperature, and power supply for the different conditions in the ODHE test. $\frac{O_2}{C_2H_6} = \frac{J_{O2}\cdot Area}{F_{C2H6}}$; $\frac{O_2}{C_2H_{6(in)}} = \frac{J_{O2}\cdot 0.01}{F_{C2H6}}$

Experiment	T_R (°C)	T_M (°C)	Power supplied (W)	J_{O2} ($mL\cdot min^{-1}\cdot cm^{-2}$)	$\frac{O_2}{C_2H_6}$	$\frac{O_2}{C_2H_{6(in)}}$
$BSCF_{650°C}$	643	653	-	0.93 ± 0.08	0.07	$2.4\cdot10^{-3}$
$BSCF_{elect}$	670	854	22.3	8.40 ± 0.06	0.65	$2.2\cdot10^{-2}$
$BSCF_{850°C}$	856	877	-	10.6 ± 0.2	0.83	$2.8\cdot10^{-2}$
CTO_{elect}	674	871	35.9	10.9 ± 0.1	0.88	$2.7\cdot10^{-2}$

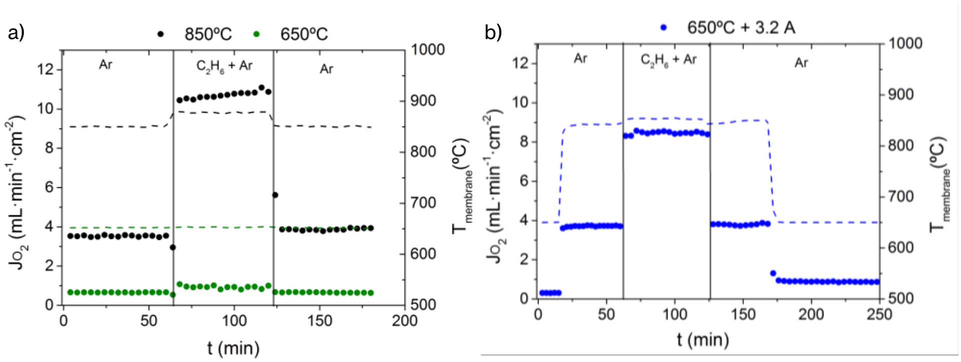

Figure 5. 10. Oxygen permeation and membrane temperature under ODHE reaction tests for the BSCF coated membrane: **a)** non-electrified membrane at 650 ºC and 850 ºC and **b)** electrified membrane.

The results for the ODHE reaction with the different evaluated membranes, electrified and non-electrified, are shown in Figure 5. 11. Figure 5. 11a plots the variation of the selectivity to ethylene as a function of the ethane conversion. In contrast, Figure 5. 11b shows the selectivities for all the reaction products generated during the catalytic test for the four performed experiments. The highest ethylene selectivity is obtained for $BSCF_{650°C,}$ whereas the obtained conversion is the lowest, corresponding to low O_2/C_2H_6 ratios and low reaction temperature (see Figure 5. 9b and Table 5. 3). On the opposite, $BSCF_{850°C}$ presents the highest ethane conversion and the lowest ethylene selectivity as predicted by the thermodynamic calculations at high reaction temperature and high O_2/C_2H_6 ratio (whereas an important selectivity to secondary products such as CO, CO_2, and CH_4 is observed). However, the ethylene yield obtained for both membranes did not reach more than 10%. Regarding the performance of the electrified experiments with both membranes, higher ethylene yields are obtained, reaching values of 30% and 40% for CTO_{elect} and $BSCF_{elect}$, respectively. In the case of the electrified membranes, the production of CO_2, CO, and CH_4 is relevant in contrast with the corresponding selectivities observed at the $BSCF_{650°C}$, in which the ethylene selectivity is ~100%. This difference in the selectivity is in line with the higher average O_2/C_2H_6 ratio (one order of magnitude higher) in the electrified membranes, while the nominal temperature in the outer reactor chamber remains similar for the three experiments. The superior catalytic performance of the electrified membrane reactors could be related to the combination of (1) the distributed oxygen dosing along the reaction coordinates and (2) the temperature gradient between the bulk gas stream (~670 °C) and the catalytic membrane coating (850 °C), acting as ODHE catalyst and oxygen-delivery surface.

The O_2/C_2H_6 obtained in the electrified experiments is very similar to the $BSCF_{850°C}$, and the difference in the performance can not only be explained by the temperature difference. As oxygen permeation is distributed along the active membrane length, the O_2/C_2H_6 ratio progressively increases. Thus, to obtain a more accurate O_2/C_2H_6 ratio in the ODHE reaction, two different ratios were calculated: (1) at the reactor inlet, taking into account the C_2H_6 fed in the reaction chamber ($O_2/C_2H_{6(in)}$) and (2) at the reactor outlet considering the C_2H_6 concentration ($O_2/C_2H_{6(out)}$) obtained in the GC analysis.

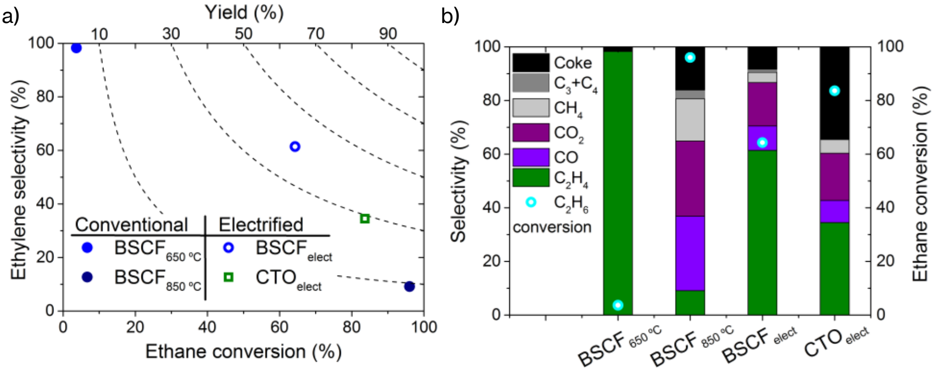

Figure 5. 11. a) Ethylene selectivity as a function of ethane conversion for BSCF without electrification at different temperatures, 650 °C and 850 °C (BSCF$_{650°C}$ and BSFC$_{850°C}$), and BSCF electrified at 850 °C (membrane temperature) with different catalytic layers, BSCF$_{elect}$ and CTO$_{elect}$; **b)** Product selectivities and ethane conversion for the different conditions: BSCF$_{650°C}$, BSCF$_{elect}$, BSFC$_{850°C}$ and CTO$_{elect}$.

Figure 5. 12a plots both O_2/C_2H_6 ratios in the inlet and outlet of the reactor. In the outlet of the reactor, the obtained ratio for BSCF$_{850°C}$ is almost one order of magnitude higher than for the electrified membranes, which can explain the better performance of the latter. Figure 5. 12b compares other ratios of interest in ODHE reaction for the different conditions, $H_2/C_2H_{6,reac}$ and $H_2O/C_2H_{6,reac}$. Both ratios indicate the extent of the partial oxidation of the ethylene, the thermal cracking of ethane, and steam reforming. In the case of BSCF$_{650°C}$, the $H_2O/C_2H_{6\ reac}$ ratio is higher than 1, indicating that ODHE is not the main reaction taking place. Also, the presence of H_2 indicates that partial oxidation and water gas shift are produced. BSCF$_{850°C}$ reaches the highest $H_2/C_2H_{6,reac}$ indicating that thermal cracking is produced. In the case of the electrified membranes, the BSCF$_{elect}$ shows an $H_2O/C_2H_{6,reac}$ ratio closer to 1, indicating that ODHE is the main reaction. Here, the presence of H_2, CO, and CO_2 suggests that other reactions, such as partial oxidation and water gas shift, occur. On the other hand, the CTO$_{elect}$ presents the highest $H_2O/C_2H_{6,reac,}$ and O_2/C_2H_{6out} ratios suggesting an essential contribution to the partial oxidation reaction.

In summary, Figure 5. 12c plots C_2H_6 conversion and C_2H_4 selectivity as a function of the O_2/C_2H_6 ratio in the outlet. C_2H_6 conversion increases with the O_2/C_2H_6 ratio and the reactor temperature, whereas the opposite trend is observed for C_2H_4 selectivity in line with Figure 5. 11a. The electrified membrane reactor enables it to reach conditions, i.e., temperature and O_2/C_2H_6 ratio, maximizing C_2H_4 yields.

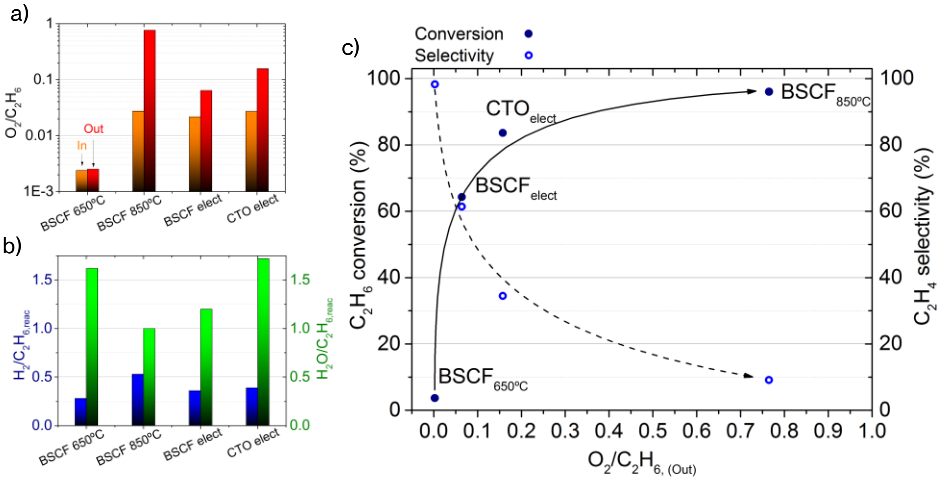

Figure 5. 12. a) O_2/C_2H_6 ratio at the beginning and the end of the membrane for the different conditions in ODHE reaction; **b)** $H_2/C_2H_{6,\text{ reac}}$ and $H_2O/C_2H_{6,\text{ reac}}$ for the different conditions in ODHE reaction; **c)** C_2H_6 conversion and C_2H_4 selectivity at different O_2/C_2H_6 at the end of the membrane for the different conditions.

5.6. Post-mortem characterization.

Finally, the structural and microstructural stability of the different membranes was characterized after the oxygen permeation and the ODHE reaction tests. It should be mentioned that the BSCF membrane with the CTO catalytic layer broke at the end of the experiment. On the other hand, the BSCF membrane with the BSCF catalytic layer was in perfect condition, Figure 5. 13. The main difference between both membranes was the power supplied to achieve 850 °C on the membrane surface. Namely, 22.3 W is for the BSFC-coated membrane, and 35.9 W is for the CTO-coated membrane with a CTO catalytic layer.

Figure 5. 13. Camera image for the catalytic membrane reactors after ODHE test: **a)** BSCF catalytic layer; **b)** CTO catalytic layer.

XRD measurements of the spent catalytic layer and the bulk membranes were performed separately by scratching the catalytic layer and measuring it and, then, grinding part of the membrane after removing the catalytic layer. In the case of the BSCF membrane with a BSCF catalytic layer, no secondary phases and/or impurities are detected in Figure 5. 14a. For the CTO-coated membrane, the presence of a minor secondary phase was detected, which might be attributed to the BSCF hexagonal phase according to the literature (Figure 5. 14b) [53,54]. Some minor quantities of CTO remain in the BSCF membrane after scratching the catalytic layer, as shown in Figure 5. 14b.

The microstructure of the membranes was studied by SEM. Some particle sintering and agglomeration of the catalytic layer are observed in the BSCF-coated membrane (Figure 5. 15a-b). In addition, within the occluded pores (Figure 5. 15c-d), some filamentous morphology may correspond to the BSCF hexagonal phase that appears at temperatures below 900 °C [55,56]. The formation of this secondary phase is related to the lowering of the oxygen permeation at 650 °C after electrification in the oxygen permeation stability test.

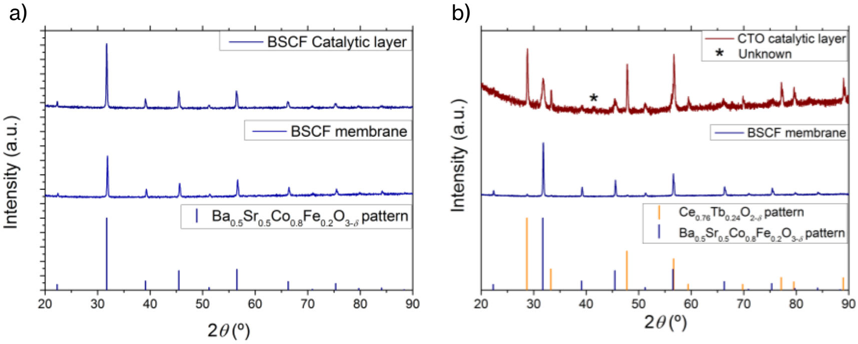

Figure 5. 14. XRD patterns after permeation and ODHE reaction tests: **a)** BSCF catalytic layer and membrane; **b)** CTO catalytic layer and BSCF membrane. ICSD codes: 193171 (CTO) and I257399 (BSCF).

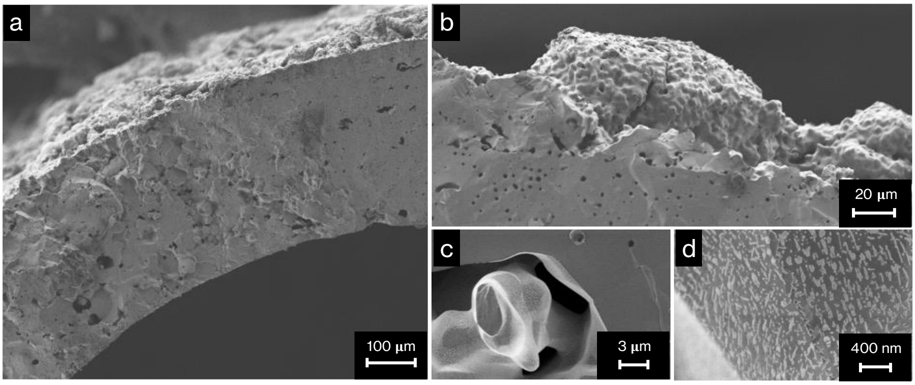

Figure 5. 15. Cross-section SEM image for the BSCF capillary membrane after electrification and ODHE reaction; **a)** Membrane and catalytic layer; **b)** BSCF catalytic layer; **c)** occluded pore inside the bulk of the BSCF membrane; and **d)** magnification of the occluded pore surface.

In the case of the CTO-coated membrane, densification and detachment of the catalytic layer are observed (Figure 5. 16a-b) and could explain the lower permeation obtained under electrified conditions. The observed delamination could also be attributed to the different thermal expansion coefficient (TEC) of the catalytic CTO layer and the BSCF membrane, 11.4 and $16\text{-}20 \cdot 10^{-6}$ K^{-1}, respectively [57,58]. The electrification for this membrane likely led to higher temperatures in the BSFC bulk, leading to more extensive sintering in the catalytic layers. Also, in this case, this secondary phase was present within the occluded porosity and throughout the membrane bulk (Figure 5. 16c-d). This secondary phase is similar to the CoO phase, indicating that the membrane temperature was locally close to 1000 °C[55,56]. These impurities could be formed when the membrane collapsed during the ODHE reactions, Figure 5. 13b. Two different phases can be observed in the CTO layer using secondary and Inlens detectors (Figure 5. 16e-f) related to the high-temperature cobalt diffusion into the CTO catalytic layer also observed by XRD.

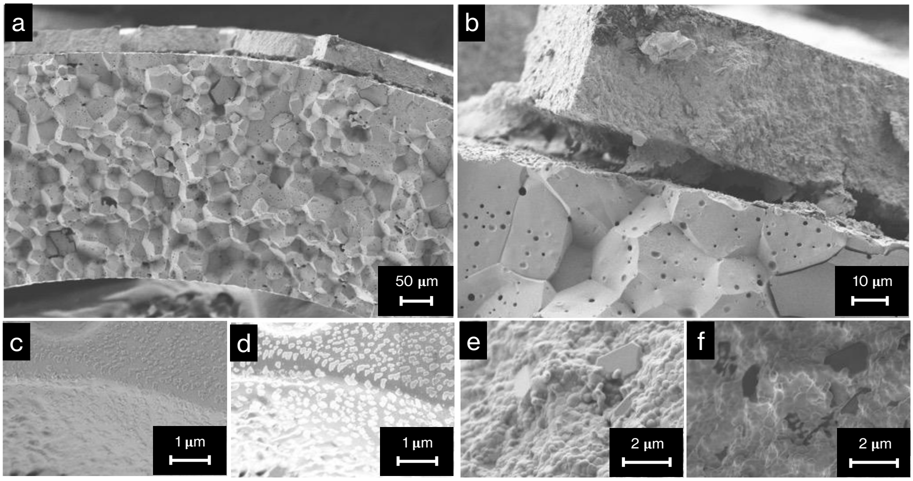

Figure 5. 16. Cross-section SEM image for the CTO capillary membrane after electrification and ODHE reaction; **a)** Membrane and catalytic layer; **b)** CTO catalytic layer; **c)** BSCF membrane bulk with SE2 detector; **d)** BSCF membrane bulk with InLens detector **e)** CTO catalytic layer with SE2 detector; **f)** CTO catalytic layer with InLens detector.

5.7. Conclusions.

The electrification of a $Ba_{0.5}Sr_{0.5}Co_{0.8}Fe_{0.2}O_{3-\delta}$-based oxygen-transport membrane enabled the in-situ heating via the Joule effect. This method facilitates (1) the membrane temperature control independent of the temperature of the surrounding bulk gas stream and (2) the control of the oxygen flux through the membrane. For a capillary membrane coated with a porous BSCF catalytic layer, 900 °C was achieved on the membrane surface while the outer reactor chamber remained at 650 °C by applying a current along the capillary and reaching an electric power of 33 W. Moreover, the membrane under electrified mode showed very stable oxygen permeation flux for >100 h.

The electrification effect was studied on a membrane coated with $Ce_{0.8}Tb_{0.2}O_{2-\delta}$ (CTO), acting as a protective barrier and catalytic layer. In this case, the protective layer also affects the thermal regime reached, reaching a lower temperature on the membrane surface, i.e., 850 °C instead of 900 °C, for the same current applied (3.7 A). This membrane was more affected by the diffusion limitations during the permeation test, obtaining a different oxygen permeation when the sweep gas was increased from 150 $NmL\cdot min^{-1}$ to 400 $mL\cdot min^{-1}$, rising from 3.7 $mL\cdot min^{-1}\cdot cm^{-2}$ to 5.2 $mL\cdot min^{-1}\cdot cm^{-2}$, respectively. This effect was explained by the sintering of the catalytic layer, decrementing the surface-exchange reaction rate.

The electrified membrane reactors show superior ODHE catalytic performance. The ethylene yield was 4-fold improved through the BSCF-membrane electrification, i.e., from 10% to ~40% o. In electrified conditions, the selectivity to secondary reactions is significantly reduced compared to ODHE at 850 °C -conventional heating-. Differentiated O_2/C_2H_6 ratios during the ODHE reaction could be reached via electrification, reaching balanced O_2/C_2H_6 ratios to mitigate partial oxidation reactions, preserving the ethylene selectivity. The electrified membrane reactors effectively combine (1) the distributed oxygen dosing along the reaction coordinates and (2) the temperature gradient between the bulk gas stream (~670 °C) and the catalytic membrane coating (850 °C), acting as ODHE catalyst and oxygen-delivery surface. Electrified oxygen transport membranes hold great potential for ODHE reactors due to the adjustable thermal regime and the control of the O_2/C_2H_6 ratios. This reactor concept can be applied to membrane processes, opening new avenues for electrification of the chemical industry.

5.8. References.

1. Kim, Y. H., Min, S. K., Gillett, N. P., Notz, D. & Malinina, E. Observationally-constrained projections of an ice-free Arctic even under a low emission scenario. *Nat Commun* **14**, (2023).

2. Harmsen, M. *et al.* Uncertainty in non-CO2 greenhouse gas mitigation contributes to ambiguity in global climate policy feasibility. *Nat Commun* **14**, (2023).

3. Chen, L., Yong, S. Z. & Ghoniem, A. F. Oxy-fuel combustion of pulverized coal: Characterization, fundamentals, stabilization and CFD modeling. *Progress in Energy and Combustion Science* vol. 38 156–214 Preprint at https://doi.org/10.1016/j.pecs.2011.09.003 (2012).

4. Arratibel Plazaola, A. *et al.* Mixed Ionic-Electronic Conducting Membranes (MIEC) for Their Application in Membrane Reactors: A Review. *Processes* **7**, 128 (2019).

5. Dai, Y. *et al.* Recent progress in heterogeneous metal and metal oxide catalysts for direct dehydrogenation of ethane and propane. *Chemical Society Reviews* vol. 50 5590–5630 Preprint at https://doi.org/10.1039/d0cs01260b (2021).

6. Schucker, R. C. *et al.* Oxidative Dehydrogenation of Ethane to Ethylene in an Oxygen-Ion-Transport-Membrane Reactor: A Proposed Design for Process Intensification. *Ind Eng Chem Res* **58**, 7989–7997 (2019).

7. Choudhary, V. R., Mulla, S. A. R. & Rane, V. H. Oxidative coupling of methane and oxidative dehydrogenation of ethane over strontium-promoted rare earth oxide catalysts. *Journal of Chemical Technology and Biotechnology* **71**, 167–172 (1998).

8. Nauels, N., Herzog, S., Modigell, M. & Broeckmann, C. Membrane module for pilot scale oxygen production. *J Memb Sci* **574**, 252–261 (2019).

9. Wu, F., Argyle, M. D., Dellenback, P. A. & Fan, M. Progress in O2 separation for oxy-fuel combustion–A promising way for cost-effective CO2 capture: A review. *Progress in Energy and Combustion Science* vol. 67 188–205 Preprint at https://doi.org/10.1016/j.pecs.2018.01.004 (2018).

10. Himma, N. F., Wardani, A. K., Prasetya, N., Aryanti, P. T. P. & Wenten, I. G. Recent progress and challenges in membrane-based O2/N2 separation. *Reviews in Chemical Engineering* **35**, 591–625 (2019).

11. Allam, R. J. Improved oxygen production technologies. *Energy Procedia* **1**, 461–470 (2009).

12. Giuffrida, A., Chiesa, P., Drago, F. & Mastropasqua, L. Integration of oxygen transport membranes in glass melting furnaces. in *Energy Procedia* vol. 148 599–606 (Elsevier Ltd, 2018).

13. Bose, A. C. *Inorganic Membranes for Energy and Environmental Applications*. *Inorganic Membranes for Energy and Environmental Applications* (Springer New York, 2009). doi:10.1007/978-0-387-34526-0.

14. Wang, H., Cong, Y. & Yang, W. Investigation on the partial oxidation of methane to syngas in a tubular Ba0.5Sr0.5Co0.8Fe0.2O3-δ membrane reactor. in *Catalysis Today* vol. 82 157–166 (2003).

15. Wang, H., Cong, Y. & Yang, W. Oxidative coupling of methane in Ba0.5Sr0.5Co 0.8Fe0.2O3-δ tubular membrane reactors. in *Catalysis Today* vol. 104 160–167 (2005).

16. Garcia-Fayos, J., Lobera, M. P., Balaguer, M. & Serra, J. M. Catalyst screening for oxidative coupling of methane integrated in membrane reactors. *Front Mater* **5**, (2018).

17. Beall, C. E. *et al.* Influence of carbon on the dynamic changes in Co oxidation state of Ba0.5Sr0.5Co0.8Fe0.2O3-δ perovskite catalyst during the oxygen reduction and evolution reactions. *EcoMat* (2023) doi:10.1002/eom2.12353.

18. Cao, Z. *et al.* Simultaneous overcome of the equilibrium limitations in BSCF oxygen-permeable membrane reactors: Water splitting and methane coupling. in *Catalysis Today* vol. 193 2–7 (2012).

19. Fairuzov, D., Gerzeliev, I., Maximov, A. & Naranov, E. Catalytic dehydrogenation of ethane: A mini review of recent advances and perspective of chemical looping technology. *Catalysts* vol. 11 Preprint at https://doi.org/10.3390/catal11070833 (2021).

20. Gao, Y. *et al.* Recent Advances in Intensified Ethylene Production—A Review. *ACS Catal* **9**, 8592–8621 (2019).

21. Lei, S. *et al.* Simultaneous generation of electricity, ethylene and decomposition of nitrous oxide via protonic ceramic fuel cell membrane reactor. *Journal of Energy Chemistry* **77**, 359–368 (2023).

22. Fan, Y. *et al.* Emerging anode materials architectured with NiCoFe ternary alloy nanoparticles for ethane-fueled protonic ceramic fuel cells. *J Power Sources* **515**, (2021).

23. Wu, W., Hu, H. & Ding, D. Low-temperature ethylene production for indirect electrification in chemical production. *Cell Reports Physical Science* vol. 2 Preprint at https://doi.org/10.1016/j.xcrp.2021.100405 (2021).

24. Luongo, G. *et al.* Highly Selective Oxidative Dehydrogenation of Ethane to Ethylene via Chemical Looping with Oxygen Uncoupling through Structural Engineering of the Oxygen Carrier. *Adv Energy Mater* **12**, (2022).

25. Yusuf, S., Neal, L. M. & Li, F. Effect of Promoters on Manganese-Containing Mixed Metal Oxides for Oxidative Dehydrogenation of Ethane via a Cyclic Redox Scheme. *ACS Catal* **7**, 5163–5173 (2017).

26. Hurtado Cotillo, M. *et al.* Catalysts based on Ni-Fe oxides supported on γ-Al2O3 for the oxidative dehydrogenation of ethane. *Catalysis Today* vol. 356 312–321 Preprint at https://doi.org/10.1016/j.cattod.2019.05.044 (2020).

27. Najari, S. *et al.* Oxidative dehydrogenation of ethane: Catalytic and mechanistic aspects and future trends. *Chemical Society Reviews* vol. 50 4564–4605 Preprint at https://doi.org/10.1039/d0cs01518k (2021).

28. Stansch, Z., Mleczko, L. & Baerns, M. *Comprehensive Kinetics of Oxidative Coupling of Methane over the La 2 O 3 /CaO Catalyst*. https://pubs.acs.org/sharingguidelines (1997).

29. Gao, Y., Haeri, F., He, F. & Li, F. Alkali Metal-Promoted LaxSr2-xFeO4-δ Redox Catalysts for Chemical Looping Oxidative Dehydrogenation of Ethane. *ACS Catal* **8**, 1757–1766 (2018).

30. Lobera, M. P. *et al.* Optimization of ODHE membrane reactor based on mixed ionic electronic conductor using soft computing techniques. *Chem Eng Sci* **66**, 6308–6317 (2011).

31. Lobera, M. P., Balaguer, M., Garcia-Fayos, J. & Serra, J. M. Rare Earth-doped Ceria Catalysts for ODHE Reaction in a Catalytic Modified MIEC Membrane Reactor. *ChemCatChem* **4**, 2102–2111 (2012).

32. Lobera, M. P., Escolástico, S. & Serra, J. M. High ethylene production through oxidative dehydrogenation of ethane membrane reactors based on fast oxygen-ion conductors. *ChemCatChem* **3**, 1503–1508 (2011).

33. Sahini, M. G., Mwankemwa, B. S. & Kanas, N. BaxSr1-xCoyFe1-yO3-δ (BSCF) mixed ionic-electronic conducting (MIEC) materials for oxygen separation membrane and SOFC applications: Insights into processing, stability, and functional properties. *Ceramics International* vol. 48 2948–2964 Preprint at https://doi.org/10.1016/j.ceramint.2021.10.189 (2022).

34. Chen, D. & Shao, Z. Surface exchange and bulk diffusion properties of Ba0.5Sr 0.5Co0.8Fe0.2O3-δ mixed conductor. *Int J Hydrogen Energy* **36**, 6948–6956 (2011).

35. Araki, W., Takemura, Y., Arai, Y. & Malzbender, J. Electrical Conductivity of Ba 0.5 Sr 0.5 Co 0.8 Fe 0.2 O 3−δ under Uniaxial Compression at Elevated Temperatures . *J Electrochem Soc* **161**, F3001–F3004 (2014).

36. Zhao, H., Shen, W., Zhu, Z., Li, X. & Wang, Z. Preparation and properties of BaxSr1-xCoyFe1-yO3-δ cathode material for intermediate temperature solid oxide fuel cells. *J Power Sources* **182**, 503–509 (2008).

37. Wang, F., Nakamura, T., Yashiro, K., Mizusaki, J. & Amezawa, K. The crystal structure, oxygen nonstoichiometry and chemical stability of Ba0.5Sr0.5Co0.8Fe0.2O 3-δ (BSCF). *Physical Chemistry Chemical Physics* **16**, 7307–7314 (2014).

38. Müller, P. *et al.* Decomposition pathway of cubic Ba 0.5Sr 0.5Co 0.8Fe 0.2O 3 - δ between 700 °c and 1000 °c analyzed by electron microscopic techniques. *Solid State Ion* **206**, 57–66 (2012).

39. Haworth, P., Smart, S., Glasscock, J. & Diniz da Costa, J. C. High performance yttrium-doped BSCF hollow fibre membranes. *Sep Purif Technol* **94**, 16–22 (2012).

40. Liu, S. & Gavalas, G. R. Oxygen selective ceramic hollow fiber membranes. *J Memb Sci* **246**, 103–108 (2005).

41. Joo, J. H. *et al.* Substantial Oxygen Flux in Dual-Phase Membrane of Ceria and Pure Electronic Conductor by Tailoring the Surface. *ACS Appl Mater Interfaces* **7**, 14699–14707 (2015).

42. Catalán-Martínez, D., Santafé-Moros, A., Gozálvez-Zafrilla, J. M., García-Fayos, J. & Serra, J. M. Characterization of oxygen transport phenomena on BSCF membranes assisted by fluid dynamic simulations including surface exchange. *Chemical Engineering Journal* **387**, (2020).

43. Herzog, S., Liu, C., Nauels, N., Kaletsch, A. & Broeckmann, C. Failure Mechanisms of Ba0.5Sr0.5Co0.8Fe0.2O3−δ Membranes after Pilot Module Operation. *Membranes (Basel)* **12**, (2022).

44. Mueller, D. N. *et al.* A kinetic study of the decomposition of the cubic perovskite-type oxide BaxSr1-xCo0.8Fe0.2O 3-δ (BSCF) (x = 0.1 and 0.5). *Physical Chemistry Chemical Physics* **12**, 10320–10328 (2010).

45. Niedrig, C. *et al.* Thermal stability of the cubic phase in Ba0.5Sr 0.5Co0.8Fe0.2O3 - δ (BSCF)1. *Solid State Ion* **197**, 25–31 (2011).

46. Meffert, M. *et al.* The effect of B-site Y substitution on cubic phase stabilization in (Ba0.5Sr0.5)(Co0.8Fe0.2)O3−δ. *Journal of the American Ceramic Society* **102**, 4929–4942 (2019).

47. Weber, V. *et al.* Influence of B-site doping with Ti and Nb on microstructure and phase constitution of (Ba0.5Sr0.5)(Co0.8Fe0.2)O3−δ. *J Mater Sci* **55**, 947–966 (2020).

48. Solís, C., Balaguer, M., Garcia-Fayos, J., Palafox, E. & Serra, J. M. Progress in Ce0.8Gd0.2O2-: δprotective layers for improving the CO2stability of Ba0.5Sr0.5Co0.8Fe0.2O3-δO2-transport membranes. *Sustain Energy Fuels* **4**, 3747–3752 (2020).

49. Laqdiem, M., Garcia-Fayos, J., Almar, L., Balaguer, M. & Serra, J. M. The role of ionic-electronic ratio in dual-phase catalytic layers for oxygen transport permeation membranes. *J Memb Sci* 121578 (2023) doi:10.1016/j.memsci.2023.121578.

50. Balaguer, M., Solís, C. & Serra, J. M. Study of the transport properties of the mixed ionic electronic conductor Ce1-xTbxO2-δ + Co (x = 0.1, 0.2) and evaluation as oxygen-transport membrane. *Chemistry of Materials* **23**, 2333–2343 (2011).

51. Wang, L., Xu, G., Liu, C., Hou, H. & Tan, S. Surface-modified CeO2 coating with excellent thermal shock resistance performance and low infrared emissivity at high-temperature. *Surf Coat Technol* **357**, 559–566 (2019).

52. Zhao, X. *et al.* The effects of Ca2+ and Y3+ ions co-doping on reducing infrared emissivity of ceria at high temperature. *Infrared Phys Technol* **92**, 454–458 (2018).

53. Švarcová, S., Wiik, K., Tolchard, J., Bouwmeester, H. J. M. & Grande, T. Structural instability of cubic perovskite BaxSr1 - xCo1 - yFeyO3 - δ. *Solid State Ion* **178**, 1787–1791 (2008).

54. Niedrig, C. Electrochemical Performance and Stability of Ba 0.5 Sr 0.5 Co 0.8 Fe 0.2 O 3-δ for Oxygen Transport Membranes. (Institut für Angewandte Materialien - Werkstoffe der Elektrotechnik (IAM-WET), 2015). doi:10.5445/KSP/1000049670.

55. Müller, P. *et al.* Secondary phase formation in Ba0.5Sr0.5Co 0.8Fe0.2O3-d studied by electron microscopy. *Chemistry of Materials* **25**, 564–573 (2013).

56. Gerthsen, D. *et al.* The Effect of Dopants on the Stabilization of the Cubic BSCF Phase in O 2 - and CO 2 -Containing Atmospheres. *ECS Trans* **77**, 35–39 (2017).

57. Shuk, P., Greenblatt, M. & Croft, M. Hydrothermal Synthesis and Properties of Mixed Conducting $Ce_{1-x}Tb_{x}O_{2-\delta}$ Solid Solutions. *Chemistry of Materials* **11**, 473–479 (1999).

58. Brisotto, M. *et al.* High temperature stability of Ba0.5Sr0.5Co0.8Fe0.2O3-δ and La0.6Sr0.4Co1-yFeyO3-δ oxygen separation perovskite membranes. *J Eur Ceram Soc* **36**, 1679–1690 (2016).

6.

EFFECT OF CONDUCTIVITY IN CHEMICAL LOOPING METHANE REFORMING USING DOPED CERIA AS AN OXYGEN-CARRIER CATALYST

6. Effect of conductivity in chemical looping methane reforming using doped ceria as an oxygen-carrier catalyst

6.1. Chemical looping methane reforming

As was mentioned in the introduction, thermochemical looping processes used the high temperatures (1400 – 1000 ºC) reached in concentrated solar power plants to drive redox reactions of metal oxides that enable the production of syngas via H_2O and CO_2 splitting [2]. An alternative to this redox scheme relies on using a reducing gas (methane or biogas) in the first step, which greatly decreases the operating temperature [4].

Ceria is considered the state-of-the-art material in solar-driven thermochemical syngas production based on its high stability over prolonged and repeated cycling and fast CO_2 and H_2O splitting kinetics, with more than a decade of research and development [11,12]. In terms of material development, several attempts have been made to increase the oxygen-carrying capacity of ceria, lower the operation temperature, and improve the POM kinetics. For this purpose, four main strategies have been pursued: a) metal cation-doping in the bulk [19,23], b) surface functionalization with a metallic nanoparticle catalyst [15,24], c) incorporation of an additional bulk oxide to form dual-phase composites [24,25], and d) engineering of porous ceramic structures (additive manufacturing) [26,27]. In some cases, some of these approaches have been combined together [28,29]. The incorporation of metallic nanoparticles such as Ru [30], Rh [23], or Ni [28] has enabled faster POM kinetics due to the metal's high catalytic activity towards POM. However, Warren et al. recently demonstrated that the POM kinetics of pure ceria can be boosted by initiating the reaction over oxygen-deficient ceria [31]. This strategy also had a remarkable impact on the syngas selectivity, which approached values close to 93% [31]. The rationale behind this enhanced activity relies on the surface vacancy-mediated nature of the POM reaction mechanism[32]. Based on this fact, the formation of oxygen deficiency via metal cation doping could also exhibit similar effects in terms of improved POM performance, which eventually may increase the overall solar-to-fuel process efficiency. Based on the aforementioned trend, the majority of literature on metal-cation doping has focused on tetravalent cation doping (e.g., Zr or Hf) [19,33]. Tetravalent dopants promote the formation of intrinsic vacancies that allow for a higher oxygen-carrying capacity, which can increase the total yield of fuel produced during the CO_2/H_2O splitting step [33]. On the other hand, trivalent dopants introduce extrinsic oxygen vacancies in the bulk that enhance oxygen diffusion, improving the CO_2 splitting reaction rates [33]. Lanthanide-doped cerias have been widely studied in the Solid-State Ionics community [34]. Trivalent acceptor dopants (e.g., Gd-doped ceria) have been employed in Solid-Oxide Cell devices due to their high ionic conductivity [34]. Extensive data can be found in literature correlating the nature of the trivalent dopant with physicochemical properties, such as the total conductivity, in which a volcano-plot trend was observed with the dopant ionic radii [35–37].

However, few works connect these fundamental insights with redox exchange activity in other relevant processes, such as solar-thermochemical fuel production, chemical looping, or other thermo-catalytic processes at high temperatures [37–40]. For this purpose, herein we investigate the impact of lanthanide cations incorporation in ceria and its impact on CLR. The objective was to study the influence of the dopant ionic radium on the CO_2 splitting kinetics. The rationale behind the work is to alter the CeO_2 structure to improve the conductivity, which might, in turn, increase the ionic diffusion and, eventually, the CO_2 splitting kinetics. Our results indicate a correlation between the total conductivity and dopant ionic radius on the CO_2 splitting kinetics. Our work aims to shed light on the dopant`s role in the CLR process and can be used to rationally design more efficient redox materials by controlling the defect concentration and oxygen-ion conduction, hence enabling more efficient fuel production.

6.2. Sample preparation

The redox materials, $Ce_{0.9}Ln_{0.1}O_{2-\delta}$ (Ln: Y, La, Nd, Gd, and Er), were synthesized by modifying the Pechini method. The precursors used were: $Ce(NO_3)_3 \cdot 6H_2O$ 99% (Sigma Aldrich), $Y(NO_3)_3 \cdot 6H_2O$ 99.9% (ABCR), $La(NO_3)_3 \cdot 6H_2O$ 99.9% (Sigma Aldrich), $Nd(NO_3)_3 \cdot 6H_2O$ 99.9% (Sigma Aldrich), $Gd(NO_3)_3 \cdot 6H_2O$ 99.9% (Sigma Aldrich) and $Er(NO_3)_3 \cdot 5H_2O$ 99.9% (Sigma Aldrich). The materials were finally calcined to 1000 °C for 5 h, using a heating and cooling rate of 2 °C/min. Commercial CeO_2 (Sigma Aldrich) was used as a benchmark in this study.

6.3. Structural properties of lanthanide-doped ceria

The synthesized materials were characterized by XRD, represented in Figure 6. 1a. The lattice constant as a function of the radius of the dopant (Figure 6. 1b). All the samples exhibit the diffraction peaks similar to the CeO_2 cubic fluorite phase (Fm3m). No impurities or secondary phases were detected, confirming a pure phase for all the samples analyzed (Figure 6. 1a).

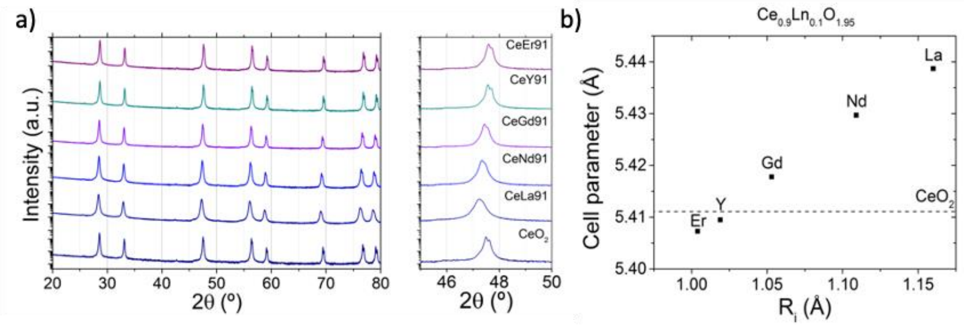

Figure 6. 1. a) X ray diffractograms of commercial CeO_2 and as-synthesized $Ce_{0.9}Ln_{0.1}O_{2-\delta}$ powders; **b**) Cell parameter, *a*, of the trivalent doped ceria samples versus ionic radium of the dopant.

The cubic lattice parameter, *a*, of each sample was calculated via Rietveld refinement (represented in Figure 6. 2). As expected, the displacement in the diffraction peaks is related to the ionic radius (Ri) of the lanthanide dopant, indicative of a solid solution (Figure 6. 1b). A lattice shrinkage was observed when doping with Er and Y (5.4073 and 5.4095 Å, respectively), whereas an expansion of the fluorite crystal lattice was obtained with Nd- and La-doping (5.4297 and 5.4387 Å, respectively). Gd-doped ceria presented a slight displacement (5.4178 Å), with a cell parameter closer to the undoped ceria (5.4111 Å). The CeY91 cell parameter value is in the same range as CeO_2, while CeGd91 shows a slight lattice expansion. It will be shown later that the cell size can have profound implications for the redox properties of these materials.

Furthermore, the specific surface area was determined via the BET method (N_2 adsorption-desorption) for the samples treated at the same temperature (25 °C), and the results are shown in Table 6. 1. BET values increase when the lattice constant increases. The samples doped with larger cations exhibit lower sinterability, which may be related to lower cation mobility during the sintering process [41,42]. Specifically, high surface areas were observed for CeLa91 and CeNd91, being 4 times larger than the other materials in this study.

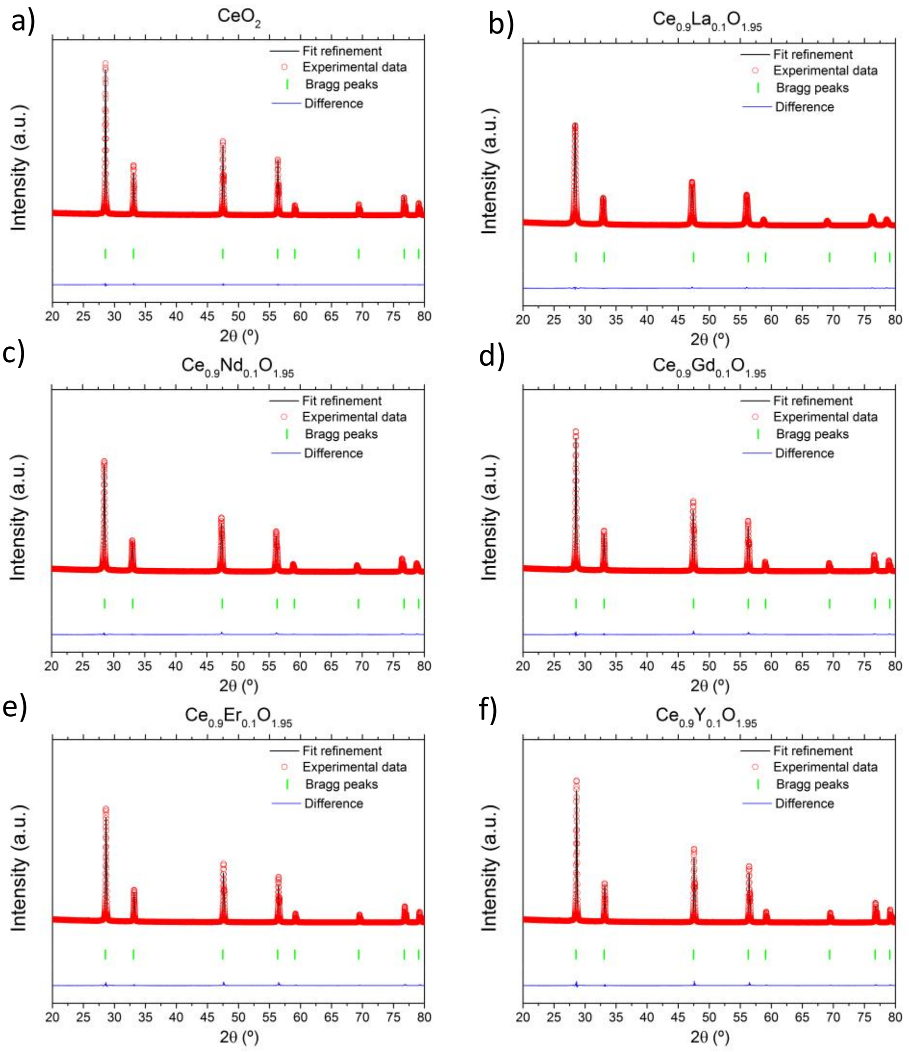

Figure 6. 2. Rietveld refinement for commercial CeO_2 (**a**) and **CeLn91** synthetized by Pechini method at 1000 ºC for 5 h. Ln: La (**b**), Nd (**c**), Gd (**d**), Er (**e**) and Y (**f**).

Table 6. 1. Summary of ceria-based materials synthesized and sintered at 1000 °C for 5 h.

	Formula	**Dopant radius (Å)**	***a*** **(Å)**		**S_{BET} ($m^2 \cdot g^{-1}$)**
CeEr91	$Ce_{0.9}Er_{0.1}O_{1.95}$	1.004	5.40734	± 0.00005	2.77
CeY91	$Ce_{0.9}Y_{0.1}O_{1.95}$	1.019	5.40953	± 0.00004	2.04
CeO2	CeO_2	-	5.41109	± 0.00003	2.82
CeGd91	$Ce_{0.9}Gd_{0.1}O_{1.95}$	1.053	5.41784	± 0.00004	3.00
CeNd91	$Ce_{0.9}Nd_{0.1}O_{1.95}$	1.109	5.42968	± 0.00006	13.34
CeLa91	$Ce_{0.9}La_{0.1}O_{1.95}$	1.160	5.43869	± 0.00006	13.84

6.4. Chemical looping reforming experiments

The chemical looping reforming tests were carried out in a fixed-bed reactor (Figure 2. 10). For each test, 250 mg of sample were pressed in a pellet, crushed and sieved between 200-400 μm. Each chemical looping reforming test consisted of three cycles of reduction and oxidation with methane and CO_2, respectively, for the doped and undoped samples, maintaining the same temperature (Figure 6. 3a). First, the material was heated up to 900 °C in Argon using a heating rate of 5 °C/min. The total flow rate was 100 $mL \cdot min^{-1}$. The reduction step was performed under a 5% CH_4-Ar (Praxair) atmosphere, whereas the oxidation was carried out under 5%CO2-Ar atmosphere, obtained by mixing pure Ar with a calibrated mixture of 15% CO_2 in Ar (Praxair). Each step had a duration of 5 min, with purging steps of 2 min using pure Ar in between. The redox cycle was repeated three times at each temperature, from 900 °C to 750 °C, with decreasing steps of 50 °C (Figure 6. 3b).

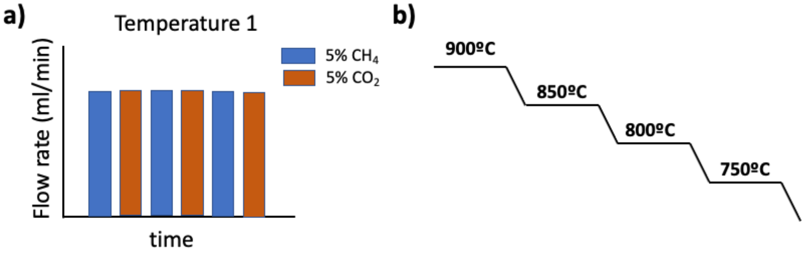

Figure 6. 3. a) Schematic of the gas flow compositions used in each of the chemical looping cycles for each temperature; **b)** Schematic of the temperature program used for the chemical looping reforming test.

To analyze the product gas composition, a Thermostar mass spectrometer (Pfeiffer Vacuum) was used. Prior to the CRL test, the mass spectrometer was calibrated to quantify the fuel produced. The calibration was done with a gas mixture of 1% H_2, 1% CO, 1% CH_4, and 1% CO_2 balanced in Ar (Linde). The mass-to-charge ratio of m/z=28 required correction because of the CO_2 contribution. Thus, a factor for the m/z=28 mass in CO_2 was extracted from the CO and CO_2 signal in the experiments (see Eq. 3). The calibration was further confirmed by feeding calibrated gas mixtures, e.g., 15% CO_2 and Ar (two-point calibration was used). When all signals were stable, the correction factor, *f*, was obtained for m/z=28 related to the CO_2 contribution as shown in Eq. 6. 3:

$$f = \frac{M_{28}}{M_{44}} \qquad \text{Eq. 6. 3}$$

Here, M_{28} is the signal for the mass-to-charge ratio 28, and M_{44} is the signal for the mass-to-charge ratio 44. Once *f* has been estimated, the CO signal can be corrected as follows:

$$M_{CO} = M_{28} - f \cdot M_{44} \qquad \text{Eq. 6. 4}$$

Where M_{CO} is the mass to charge ratio of CO. For the other mass to charge ratios we used: m/z = 2 (M_2) for the H_2, m/z = 15 (M_{15}) for the CH_4 and m/z = 44 (M_{44}) for the CO_2.

CO selectivity (S_{CO}) in the reduction step was calculated according to the following equation:

$$S_{CO} = \frac{[CO]}{[CO]+[CO_2]} \qquad \text{Eq. 6. 5}$$

where, [CO] and [CO_2] are the production of CO and CO_2, respectively, during the 5 min reduction step in CH_4. The products productions ([CO], [H_2] and [CO_2]) in each step was calculated with the integration of the product curve by each step time (5 min).

The gas production in both steps was normalized with the amount of redox catalyst, i.e. CO production in the splitting of CO_2:

$$CO\ production = \frac{[CO]}{m_{catalyst}} \left({}^{ml}/_{g}\right) \qquad \text{Eq. 6. 6}$$

Where, [CO] was the total production of CO and $m_{catalyst}$ is the quantity of catalyst in the reactor. The same calculations were done in the reduction step for the products in that step: [H_2], [CO], and [CO_2].

For these tests, each oxide was subjected to three redox cycles at four different temperatures (900 °C, 850 °C, 800 °C and 750 °C). The objective was to understand both the effects of metal cation doping and operating temperature on the syngas production and CO_2 splitting. For example, Figure 6. 4 shows a test of three consecutive redox cycles conducted at 900 °C for CeNd91. The gas production rate is normalized with the oxide sample mass to compare all the different redox materials. Upon methane injection, the material produced syngas via methane partial oxidation, while CO_2 resulted from the overoxidation (full combustion) of methane reacting with surface oxygen species.[6] After purging the reactor with Ar, a sharp peak of CO is produced upon CO_2 injection in the reactor, confirming the ability of these materials to split CO_2 [1]. The reaction profile (Figure 6. 4) is reproducible along the three redox cycles conducted with minor differences in the gas peak production values for the POM reaction, whereas CO_2 splitting was remarkably stable.

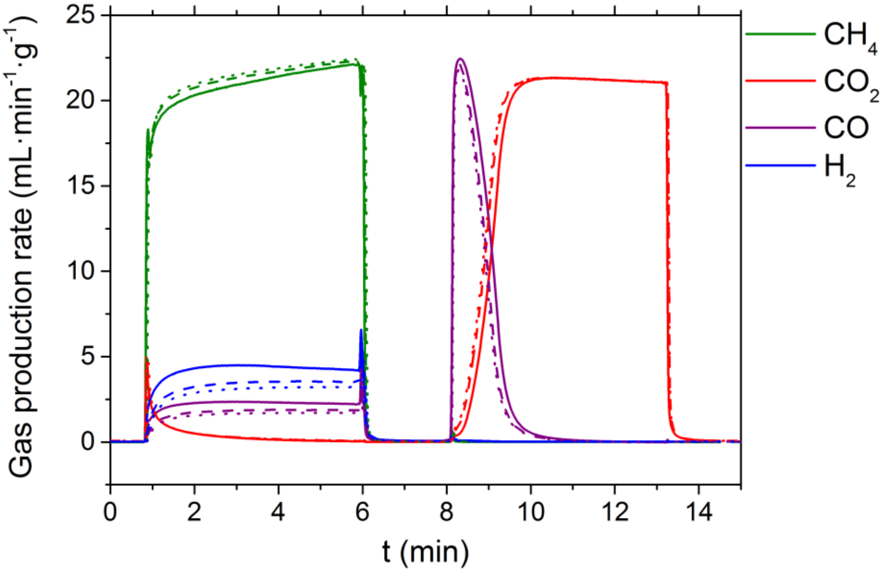

Figure 6. 4. Methane partial oxidation and CO_2splitting cycles for CeNd91 at 900°C. Each chemical looping test consists of three redox cycles.

In Figure 6. 5 and Figure 6. 6, each temperature step is zoomed out, illustrating the gas production rates during the reduction step (Figure 6. 5) and during the oxidation step (Figure 6. 6). In the reduction step, methane reacts with surface oxygen species emerging from the CeLn91 bulk, leading to the partial reduction of certain Ce^{4+} cations with the concomitant formation of oxygen vacancies. Besides the POM reaction (Eq. 1. 7), two more possible side reactions can take place in the reduction step:

$$\frac{1}{\delta}CH_4 + Ce_{0.9}Ln_{0.1}O_{1.95} \rightarrow \frac{1}{\delta}CO_2 + \frac{2}{\delta}H_2O + Ce_{0.9}Ln_{0.1}O_{1.95-\delta} \qquad \text{Eq. 6. 7}$$

$$CH_4 \rightarrow C(s) + 2H_2 \qquad \text{Eq. 6. 8}$$

The complete combustion of the methane (Eq. 6. 7) implies the reaction of methane with the oxygen species chemisorbed on the ceria surface. This reaction is controlled by the availability of surface oxygen species; thus, a higher surface area will lead to a higher amount of CO_2 coming from complete combustion. [43] Next, POM starts producing syngas (CO + H_2), (Eq. 1. 7). In this selective reaction, the catalytic mechanism involves the solid-state oxygen-ion diffusion through the ceria lattice. [43] This reaction is slower than the complete combustion, where highly reactive chemisorbed oxygen species quickly react with methane in an unselective manner. [43,44] When POM is the predominant reaction, the H_2/CO ratio equals 2. A ratio higher than 2 is indicative of methane decomposition, in which coke and hydrogen (Eq. 8) are produced. Figure 6. 5 shows that, upon CH_4 injection, a sharp CO_2 peak forms, which rapidly decreases (note here that the H_2O signal is not shown since it could not be analyzed quantitatively), followed by the production of syngas.

For the CeNd91, H_2 production rates of 4.4, 1.4, 0.6, and 0.3 $mL\cdot min^{-1}\cdot g^{-1}$ were achieved at 900 °C, 850 °C, 800 °C, and 750 °C, respectively. This illustrates the effect of temperature on the POM kinetics and reduction extent, which decreases by an order of magnitude at 750 °C with respect to its value at 900 °C.

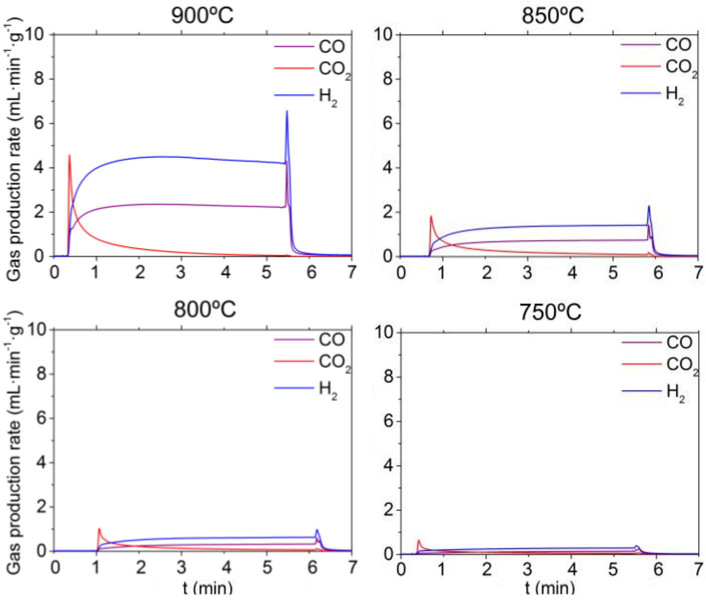

Figure 6. 5. Gas production rate curves for CeNd91 sample during the POM (reduction step) at 900, 850, 800, and 750 °C.

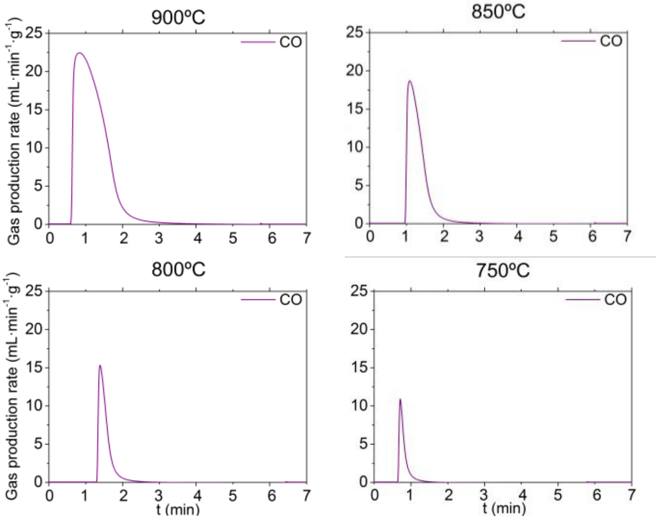

Figure 6. 6. CO production rate curves during the splitting of CO_2 in the oxidation step for CeNd91 sample at 900, 850, 800 and 750°C.

Figure 6. 6 shows the CO production rate ascribed to the splitting of CO_2 at the four different temperatures (900-750 °C) tested. Upon the reoxidation of the catalyst, the CO achieves maximum productivity before the catalyst is fully oxidized (CO peak rate). This CO peak rate is related to the kinetics of the CO_2 splitting reaction, which is controlled by the oxygen-ion diffusion through the ceria lattice. In this case, the peak of CO production is 22.5, 18.7, 15.3, and 10.9 $mL \cdot min^{-1} \cdot g^{-1}$ at 900 °C, 850 °C, 800 °C, and 750 °C, respectively. Like POM, the gas production rates decrease with temperature, which is ascribed to kinetics (via defect diffusion) of the formation of extrinsic oxygen vacancies (i.e., additional oxygen non-stoichiometry, δ in $Ce_{0.9}Ln_{0.1}O_{1.95-\delta}$) participating in the CO_2 deoxygenation reaction to form CO gas. This process is similar for all the samples (see Figure 6. 7 to Figure 6. 12).

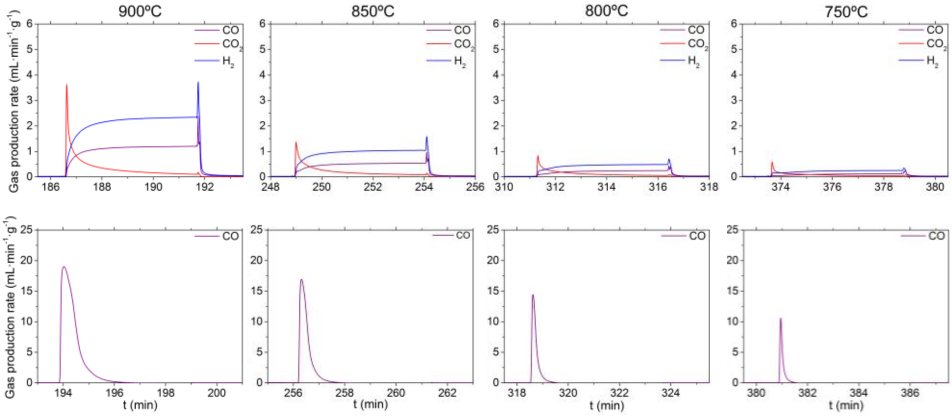

Figure 6. 7. Gas production curves for one chemical looping cycle for the **CeEr91** sample at each temperature. Top: Products for the Reduction step with CH_4 reforming; Bottom: CO production from the oxidation step on the splitting of CO_2.

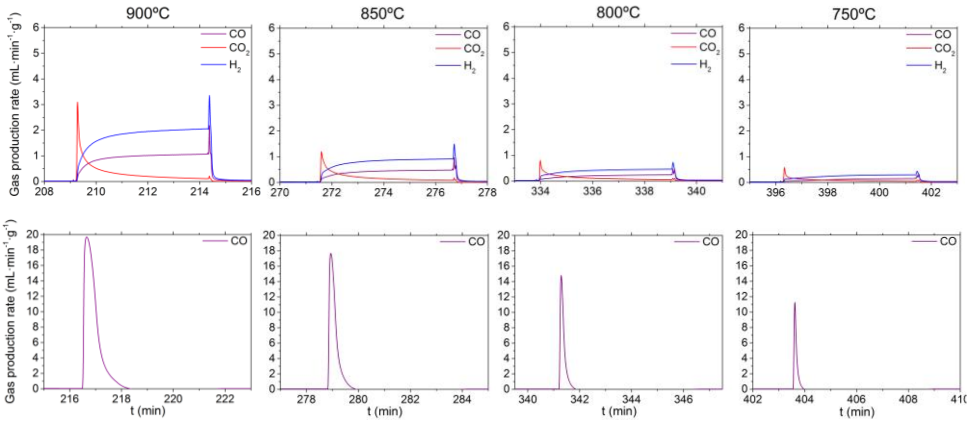

Figure 6. 8. Gas production for one chemical looping cycle for the **CeY91** sample at each temperature. Top: Products for the Reduction step with CH_4 reforming; Bottom: CO production from the oxidation step on the splitting of CO_2.

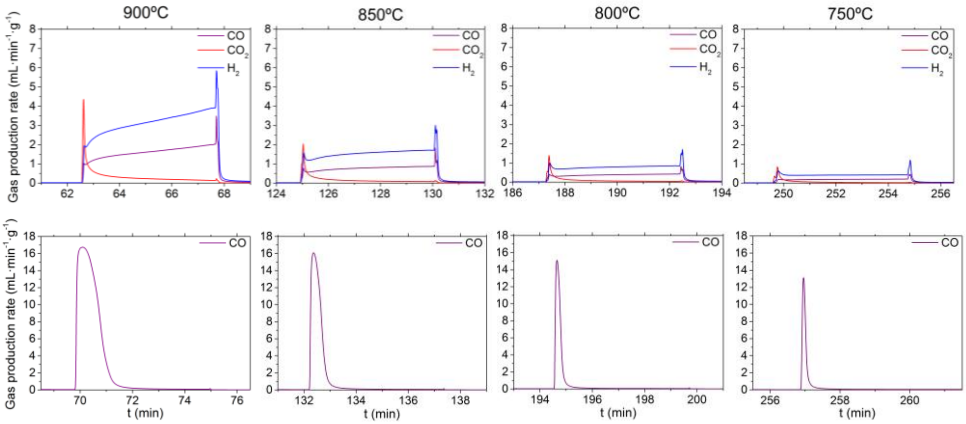

Figure 6. 9. Gas production for one chemical looping cycle for the **CeO_2** sample at each temperature. Top: Products for the Reduction step with CH_4 reforming; Bottom: CO production from the oxidation step on the splitting of CO_2.

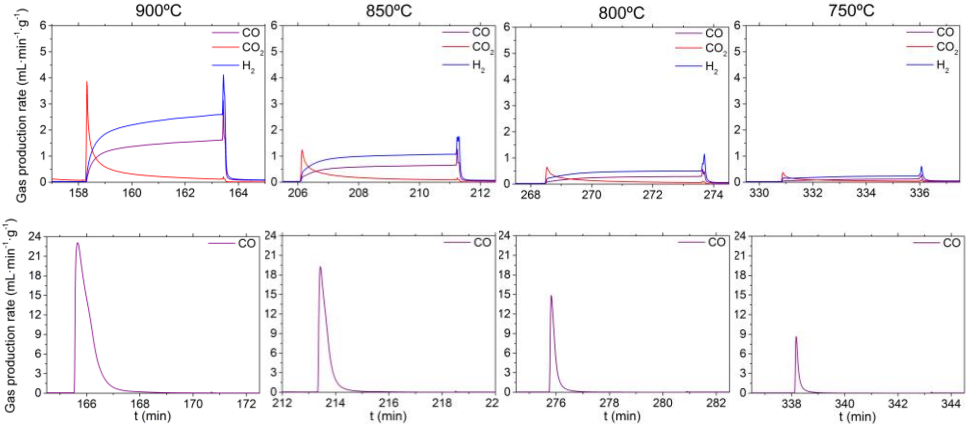

Figure 6. 10. Gas production for one chemical looping cycle for the **CeGd91** sample at each temperature. Top: Products for the Reduction step with CH_4 reforming; Bottom: CO production from the oxidation step on the splitting of CO_2.

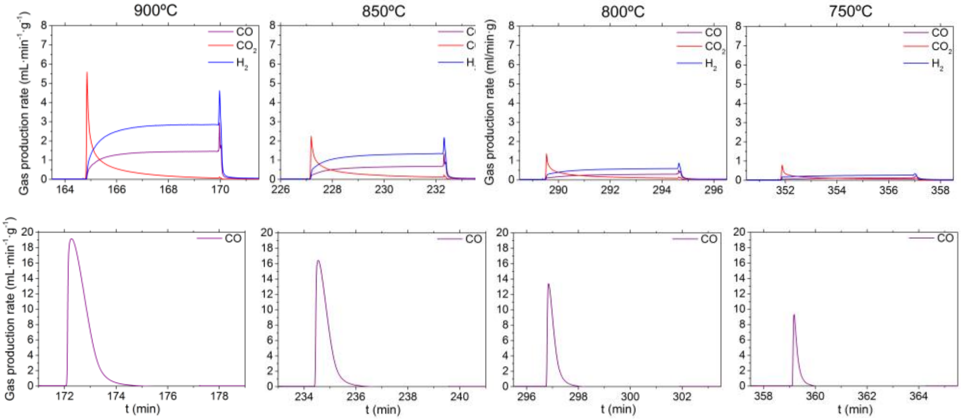

Figure 6. 11. Gas production for one chemical looping cycle for the **CeLa91** sample at each temperature. Top: Products for the Reduction step with CH_4 reforming; Bottom: CO production from the oxidation step on the splitting of CO_2.

6.5. Impact of dopant ionic radius on POM reaction

As depicted in Figure 6. 4, two reactions are taking place during the reduction step: the complete combustion of the methane (Eq. 6. 7) and the partial oxidation of methane (Eq. 1. 7). Considering that the reaction of interest is the partial oxidation of methane, the selectivity toward CO production should be ideally as high as possible, minimizing the undesired CO_2 formation. The production of hydrogen is represented in Figure 6. 12a. The highest H_2 production was reached for the pure ceria, producing: 17.1, 8.5, 4.3 and 2.4 $mL·g^{-1}$ at 900 °C, 850 °C, 800 °C and 750 °C, respectively. It can be observed that at 900°C the highest H_2 production is obtained for CeNd91 and CeLa91, with 16.6 and 13.9 $mL·g^{-1}$, respectively. Moreover, the highest production is related to the material with the highest ionic conductivity, CeNd91.45. The production of CO (Figure 6. 12b) is ca. half the H_2 productions (Figure 6. 12a), and the specific H_2/CO ratio, typically <2, is plotted in Figure 6. 12c.

Figure 6. 12d depicts the calculated CO selectivity (S_{CO}, see Eq. 6. 5) values for all the temperatures and materials tested in this study. Figure 6. 12a shows that the lanthanide-doped ceria samples exhibit lower S_{CO} values than the undoped ceria. The latter shows S_{CO} values of 82.8, 80.5, 76.9 and 72.3% for decreasing temperatures from 900 °C to 750 °C. For the CeLn91 materials, the highest CO selectivity is for CeGd91 and CeNd91, with 79.3 % and 80.1%, respectively, at 900°C respectively. For all the tested materials, $H_2/CO \approx 2$, which confirms that secondary reactions are suppressed.

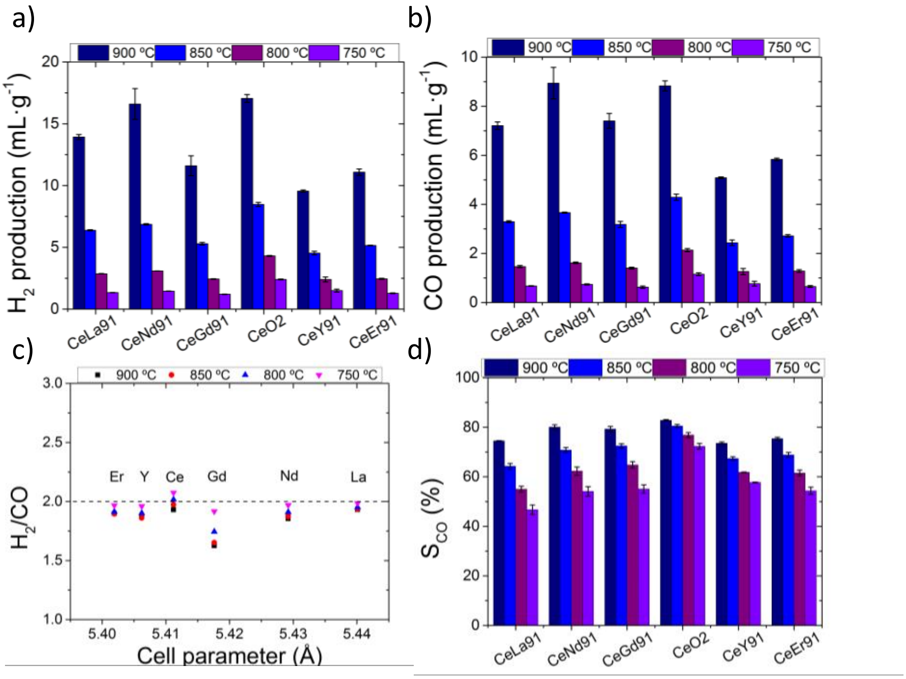

Figure 6. 12. Syngas production during POM reaction for CeLn91 (Ln: La, Nd, Gd, Ce, Y, and Er) at 900 °C, 850 °C, 800 °C, and 750 °C: **a)** H_2 production; **b)** CO production; **c)** CO selectivity; **d)** H_2/CO ratio.

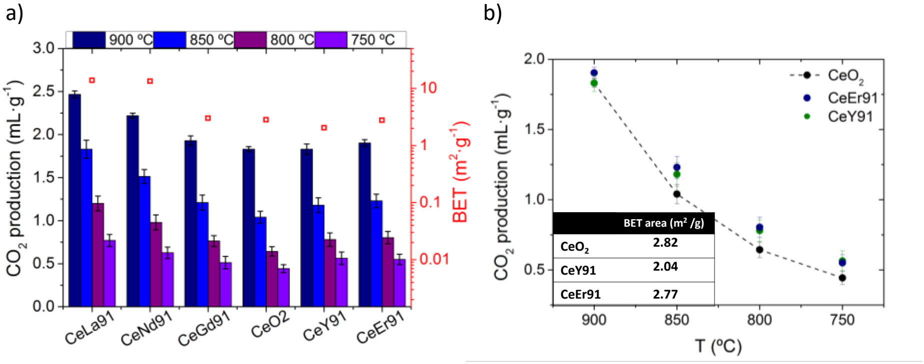

	BET area (m² /g)
CeO_2	2.82
CeY91	2.04
CeEr91	2.77

Figure 6. 13. CO_2 production in POM reaction for CeLn91 (Ln: La, Nd, Gd, Ce, Y, and Er) at 900, 850, 800, and 750°C: **a)** CO_2 and surface area BET; **b)** CO_2 production for CeO_2 and CeLn91 with lower surface area BET.

The lower selectivity of CO observed for CeLn91 compared to CeO_2 is ascribed to an increase in the rate of the complete combustion reaction. Complete combustion in the chemical looping of methane can be directly related to the availability of surface-adsorbed oxygen species on the oxide material [43,44]. These oxygen species are less constrained than that emerging from the bulk, so they react faster, hence promoting overoxidation. The oxygen availability is, in turn, related to two aspects: (i) the specific surface area and (ii) the adsorption properties of the surface, i.e., the surface concentration of adsorption sites for active oxygen species and the adsorption enthalpy. In section 3.1, an increase in the specific surface area for the larger dopant cations was observed (Table 6. 1). Interestingly, we observe that the CeLn91 with a larger ionic radius also exhibits a higher production of CO_2 (Figure 6. 13a), which could be associated with a higher specific surface area [43,46] In general, all the CeLn91 materials tested produced more CO_2 than the undoped ceria. Figure 6. 13b presents the CO_2 production for CeO_2 in comparison with that of CeY91 and CeEr91, the latter exhibiting lower surface area than CeO_2. Both doped ceria samples produce more CO_2 than CeO_2. The intrinsic oxygen vacancies in CeLn91 improve the kinetics of the reaction of complete combustion of methane (Eq. 6. 7) and produce more CO2, and this is ascribed to the role of these vacancies acting as additional sites that facilitate the oxygen adsorption and, thus, boosting the surface concentration of active oxygen species. An increase in the complete combustion reaction directly produced a decrease in the selectivity of CO, Figure 6. 12c.

6.6. Impact of dopant ionic radius on CO_2 splitting reaction

In the previous section, it was observed that for the POM reaction, CeLn91 improves the surface kinetics compared with CeO_2, and the extent to which this step is influenced by the nature of the dopant was studied, since lanthanide doping may influence both bulk and surface reaction steps [37]. In this section, we will pay attention to the effects of lattice properties variations on the CO_2 splitting reaction. Figure 6. 14a shows the CO production by CO_2 splitting for each material in the 750–900 °C temperature range. Opposite to the POM reaction, a linear trend between the CO production and the dopant radius cannot be inferred. Here, the highest CO production is achieved for the CeLn91 with larger doped lanthanides: CeNd91 and CeLa91 equal to 17.0 and 15.7 mL·g^{-1}, respectively, values at 900°C. The lowest production is reached with the non-lanthanide doped ceria, CeY91, with a CO production at 900 °C equal to 10.1 mL·g^{-1}. The CO production in this step is directly proportional to the reduction step, i.e., the capacity of abstracting oxygen from CO_2 is associated with both surface vacancies and intrinsic oxygen vacancies formed in the oxide bulk during the reduction step. Therefore, the specific surface area is a relevant aspect in total reaction productivity.[46]

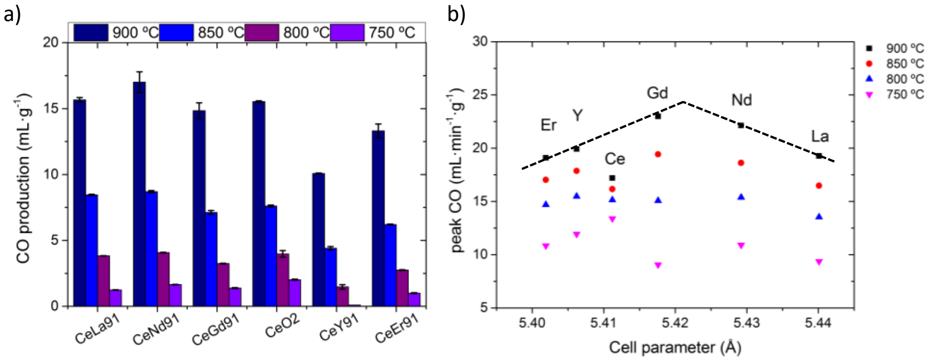

Figure 6. 14. **a)** CO production during CO_2 splitting for CeLn91 (Ln: La, Nd, Gd, Ce, Y, and Er) at 900 °C, 850 °C, 800 °C, and 750 °C; **b)** CO_2 splitting peak rates for **CeLn91** (Ln: La, Nd, Gd, Ce, Y, and Er) at 900, 850, 800 and 750°C versus the cell parameter measured at room temperature.

Even so, the kinetics of the CO_2 splitting reaction were not directly related to the surface area in these materials but to the oxygen-ion diffusion through the ceria lattice. Sediva et al. showed that if the ceria is doped with a tetravalent dopant, the CO production is increased, but the kinetics worsens in the splitting of CO_2 [33]. In the same study, these authors showed that trivalent dopants enabled the improvement of the CO_2 splitting kinetics at the cost of decreasing the CO production with respect to CeO_2 [33]. The CO peak rate results for all the temperatures assayed are represented in Figure 6. 14b. To shed light on this aspect, Figure 6. 14a represents the CO peak (height) rate at 900°C as a function of the cell parameter. A volcano plot trend can be observed, with a maximum for the CeGd91 (23.0 $mL \cdot min^{-1} \cdot g^{-1}$). CeO_2 has the lowest CO peak rate values, indicative of slower kinetics, evidencing the benefits of trivalent dopants in the catalytic promotion of CO_2 splitting kinetics [33].

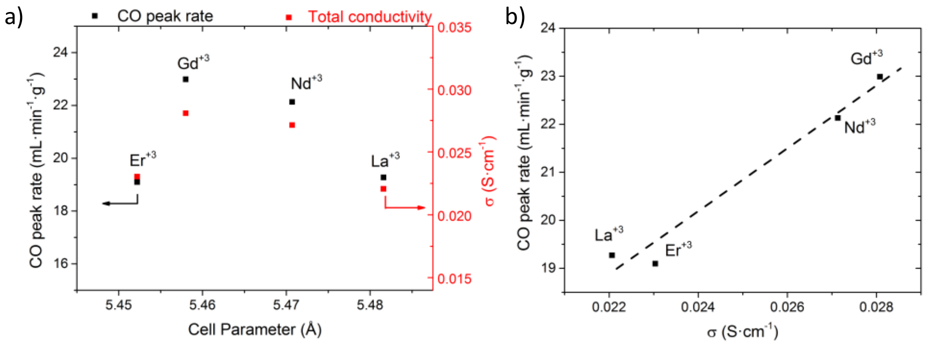

Figure 6. 15. a) CO peak rate for CeLn91 (Ln: La, Nd, Gd, Ce, Y, and Er) from CO_2 splitting at 900 °C and total conductivity at 700°C and oxidizing conditions from ref. [37], cell parameter at room temperature; b) CO peak rate for CeLa91, CeEr91, CeNd91 and CeGd91 versus their total conductivity at 700 °C in air.

Interestingly, similar volcano plot tendencies have been observed with other physicochemical properties for these lanthanide-doped ceria materials. Namely, a correlation between the total conductivity of CeLn91 (Figure 6. 15a) and the size of the dopant and/or the cell parameter, yielding the same maximum for CeGd91 (Figure 6. 15a), was already reported in literature [37,47,48]. It was also reported that when the cell parameter of a doped ceria material is close to the cell parameters of CeO_2, the oxygen-ion conductivity of the material reaches a maximum[49]. This is related to a minimum achieved in the activation energy of oxygen vacancy formation[49]. The CeGd91 has, in this study, a cell parameter of 5.4176 Å (as estimated in this study), whereas it is 5.4112 Å for CeO_2 (Table 6. 1). These values are well aligned, suggesting that CeGd91 exhibits the highest total conductivity and the fastest CO_2 splitting kinetics. Indeed, when plotting the CO peak rate (as a metric for the CO_2 splitting kinetics) versus total conductivity values found in literature, a linear relation was observed (Figure 6. 15b), evidencing for the first time a direct relationship between doped ceria materials ionic conductivity and the CO_2 splitting kinetics, and the role that the dopant ionic radium has on it. Namely, the highest mobility of oxygen anions in CeGd91, evidenced by its faster total conductivity, shows a great benefit in the CO_2 splitting kinetics.

6.7. Characterization after chemical looping test

The powders were characterized after the chemical looping tests in order to analyze the possible degradation or decomposition of the different redox materials. First, the crystal structure was analyzed by X-ray diffraction, as shown in Figure 6. 16.

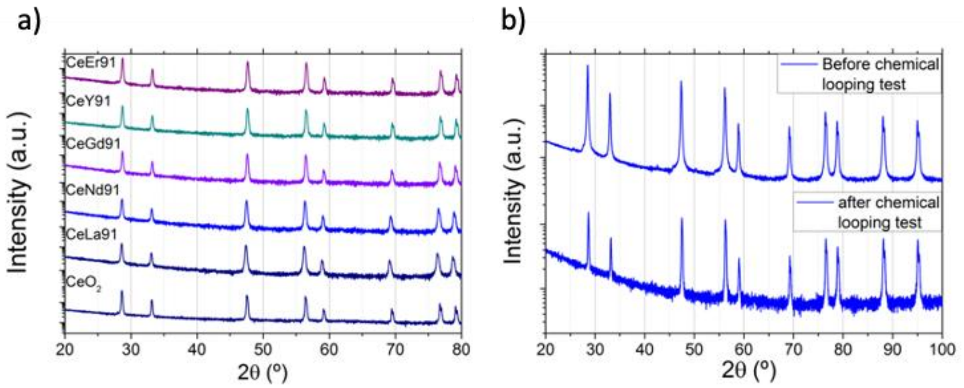

Figure 6. 16. a) X-ray diffraction for the different materials after the chemical looping test; b) Comparison of XRD for CeNd91 catalyst before and after the chemical looping test.

Figure 6. 16a shows the X-ray diffraction patterns for the CeLn91 redox materials after the chemical loops. No secondary phases were detected, indicative of non-degradation in the crystal structure of the redox oxides. CeNd91 was compared

before and after the redox cycles (Figure 6. 16b). The reflections in both XRD patterns have the same position, indicating that the material did not change after the chemical looping steps.

All the materials preserve the initial crystal structure after the chemical looping test, although some morphological changes were inferred for some of them after redox cycling. The morphology of all the samples was analyzed before and after the chemical looping cycles by SEM. Figure 6. 17 and Figure 6. 18 show a comparison of the pure CeO_2 and the trivalent-doped ceria materials with better performance before and after cycling.

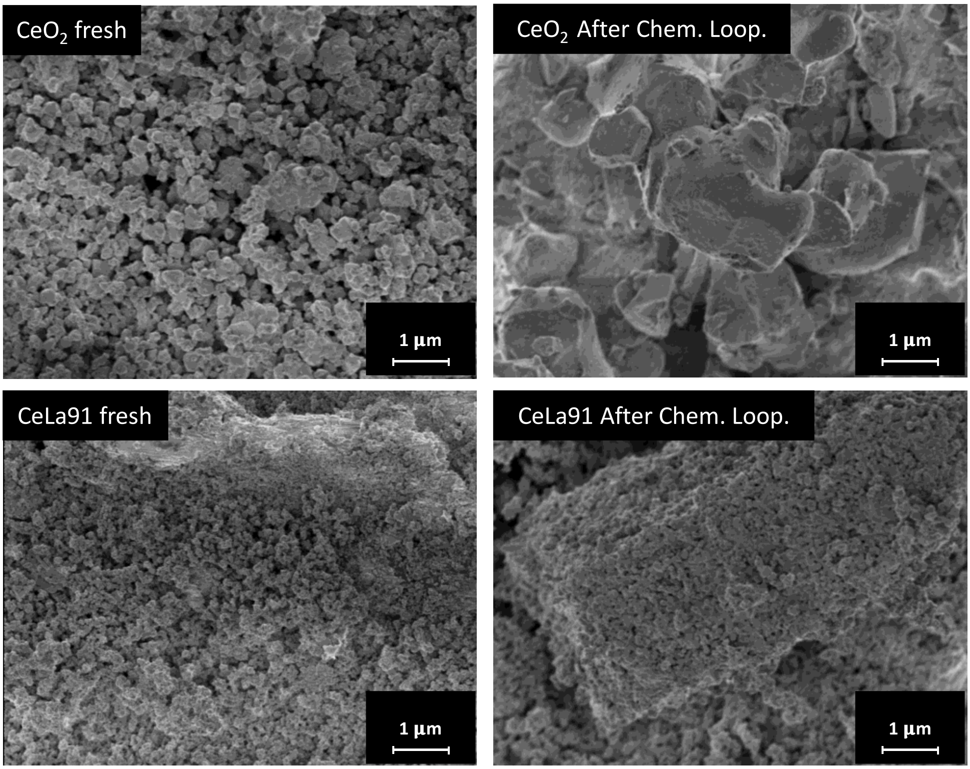

Figure 6. 17. SEM images of CeO_2 and CeLa91 before reaction and after reaction.

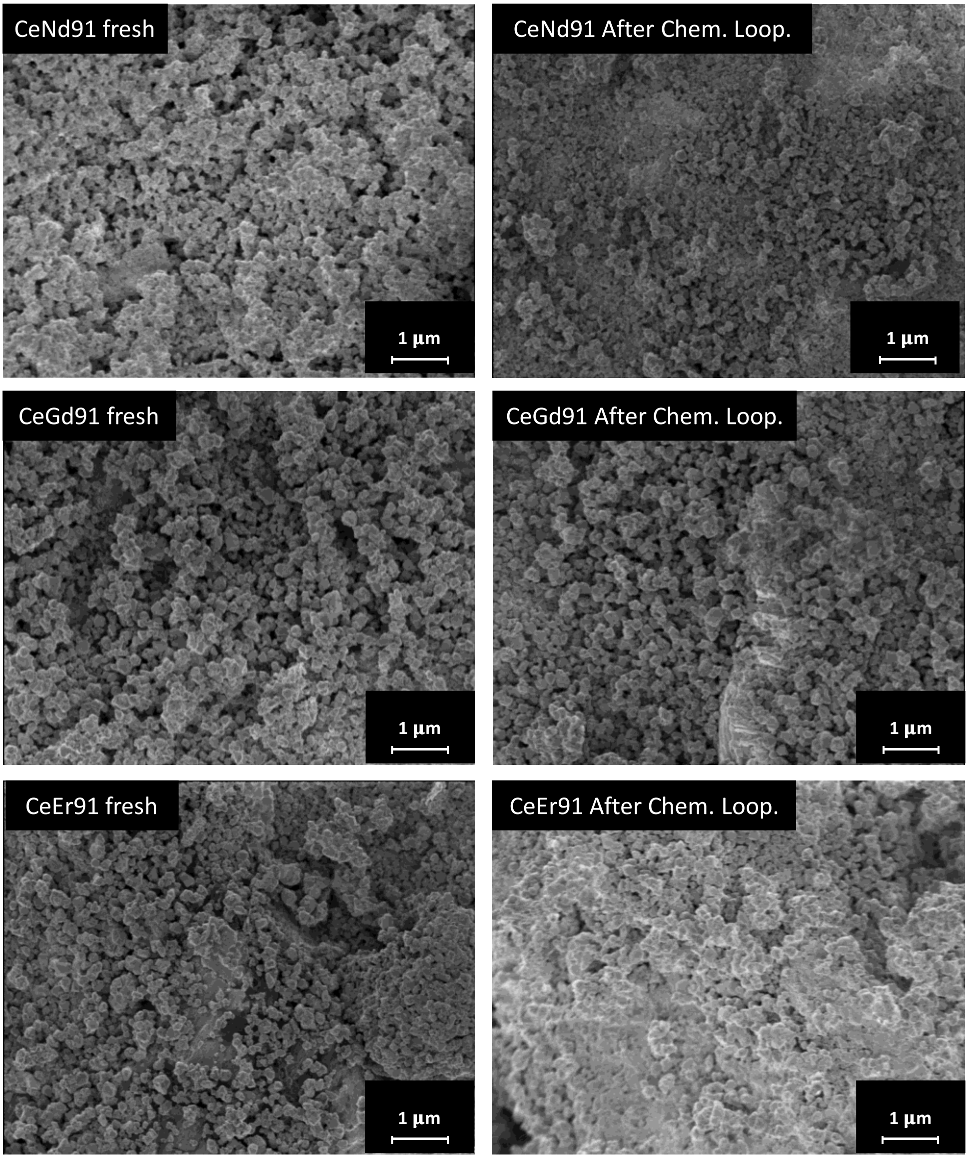

Figure 6. 18. SEM images of CeNd91, CeGd91, and CeEr91 before and after reaction.

For the pure ceria sample, there is a remarkable grain growth after the chemical looping test, Figure 6. 17. This morphological change was reported in previous works in literature, in which ceria showed a high degree of sintering after chemical looping [50,51]. In this case, the CeO_2 sample increased its grain size from 0.1 to 2-3 μm. For all the CeLn91 material, this grain growth is less evident, indicating that lanthanide doping is an efficient strategy to prevent particle sintering. For example, the SEM images for CeGd91 before and after the redox cycles test, Figure 6. 18, show that the grain size for this sample was maintained after the chemical loops. We ascribed this to Gd-doping acting as a sintering inhibitor. Indeed, Z. Tianshu et al. reported that increasing the amount of Gd doping content decreased density and grain size if compared with pure ceria sintered at the same temperature [52]. This behavior is similar for all CeLn91 materials (Figure 6. *17* and Figure 6. 18). This could indicate that the specific surface area values also remain unchanged after the chemical looping tests.

6.8. Conclusions.

In this work, a series of 10% lanthanide-doped ceria materials were synthesized to study the impact of the trivalent dopant on the methane-assisted chemical-looping production of syngas. All materials were synthesized in pure phases, with the cell parameter variation in accordance with the dopant's ionic radius. For the total amount of fuel produced in both the methane partial oxidation and CO_2 splitting reactions, we could not infer a direct trend with the size of the dopants. However, for the CO_2-splitting reaction, a volcano-like shape was observed between the CO peak rate and the lanthanide ionic radius. Interestingly, the same trend was previously observed in literature for the influence of lanthanide dopants in the total conductivity of these materials. A linear relationship was then obtained between the CO_2 splitting kinetics and the total conductivity. This confirms that oxygen-ion diffusion correlates with the CO production rate, suggesting the possibility of tailoring the CO production rate by the right choice of dopants. Namely, Gd-doped ceria was found to be at the top of the volcano plot for both CO_2 splitting rate and total conductivity, ascribed to a lower activation energy for the creation of oxygen vacancies that, in turn, are the active sites for adsorption of oxygen reaction intermediates. In addition, doped-ceria samples preserved the grain size and morphology upon redox cycling.

Overall, the trends found in this work could open the path to designing more efficient doped-ceria materials for chemical looping reforming or other thermochemical processes in which ionic diffusion plays a key role.

6.9. References.

1. Serra, J. M. *et al.* Hydrogen production via microwave-induced water splitting at low temperature. *Nat Energy* **5**, 910–919 (2020).

2. Carrillo, R. J. & Scheffe, J. R. Advances and trends in redox materials for solar thermochemical fuel production. *Solar Energy* **156**, 3–20 (2017).

3. Schäppi, R. *et al.* Drop-in fuels from sunlight and air. *Nature* **601**, 63–68 (2022).

4. Carrillo, A. J., Rupp, J. L. M. & Coronado, J. M. Redox Oxides for Thermochemical Energy Storage. in *Energy Storage and Conversion Materials* (ed. Skinner, S. J.) 136–187 (The Royal Society of Chemistry 2020, 2020). doi:10.1039/9781788011617-00001.

5. Carrillo, A. J., Kim, K. J., Hood, Z. D., Bork, A. H. & Rupp, J. L. M. La 0.6 Sr 0.4 Cr 0.8 Co 0.2 O 3 Perovskite Decorated with Exsolved Co Nanoparticles for Stable CO 2 Splitting and Syngas Production. *ACS Appl Energy Mater* **3**, 4569–4579 (2020).

6. Krenzke, P. T., Fosheim, J. R. & Davidson, J. H. Solar fuels via chemical-looping reforming. *Solar Energy* **156**, 48–72 (2017).

7. Warren, K. J., Carrillo, R. J., Greek, B., Hill, C. M. & Scheffe, J. R. Solar Reactor Demonstration of Efficient and Selective Syngas Production via Chemical-Looping Dry Reforming of Methane over Ceria. *Energy Technology* **8**, (2020).

8. Marxer, D., Furler, P., Takacs, M. & Steinfeld, A. Solar thermochemical splitting of CO 2 into separate streams of CO and O 2 with high selectivity, stability, conversion, and efficiency. *Energy Environ Sci* **10**, 1142–1149 (2017).

9. Patankar, A. S., Wu, X.-Y., Choi, W., Tuller, H. L. & Ghoniem, A. F. A Reactor Train System for Efficient Solar Thermochemical Fuel Production. *J Sol Energy Eng* **144**, (2022).

10. Krenzke, P. T., Fosheim, J. R. & Davidson, J. H. Solar fuels via chemical-looping reforming. *Solar Energy* **156**, 48–72 (2017).

11. Chueh, W. C. & Haile, S. M. A thermochemical study of ceria: exploiting an old material for new modes of energy conversion and CO2 mitigation. *Philos Trans A Math Phys Eng Sci* **368**, 3269–94 (2010).

12. Chueh, W. *et al.* High-flux solar-driven thermochemical dissociation of CO2 and H2O using nonstoichiometric ceria. *Science (1979)* **330**, 1797–1801 (2010).

13. Zhao, Z., Uddi, M., Tsvetkov, N., Yildiz, B. & Ghoniem, A. F. Redox Kinetics and Nonstoichiometry of Ce 0.5 Zr 0.5 O 2−δ for Water Splitting and Hydrogen Production. *The Journal of Physical Chemistry C* **121**, 11055–11068 (2017).

14. Haribal, V. P. *et al.* Modified Ceria for “Low-Temperature” CO 2 Utilization: A Chemical Looping Route to Exploit Industrial Waste Heat. *Adv Energy Mater* **9**, 1901963 (2019).

15. Carrillo, A. J., Navarrete, L., Laqdiem, M., Balaguer, M. & Serra, J. M. Boosting methane partial oxidation on ceria through exsolution of robust Ru nanoparticles. *Mater Adv* **2**, 2924–2934 (2021).

16. Zhao, Z., Uddi, M., Tsvetkov, N., Yildiz, B. & Ghoniem, A. F. Redox Kinetics Study of Fuel Reduced Ceria for Chemical-Looping Water Splitting. *The Journal of Physical Chemistry C* **16289**, acs.jpcc.6b01847 (2016).

17. Zhao, Z., Uddi, M., Tsvetkov, N., Yildiz, B. & Ghoniem, A. F. Enhanced intermediateerature CO2splitting using nonstoichiometric ceria and ceria-zirconia. *Physical Chemistry Chemical Physics* **19**, 25774–25785 (2017).

18. Warren, K. J. & Scheffe, J. R. Kinetic insights into the reduction of ceria facilitated via the partial oxidation of methane. *Mater Today Energy* **9**, 39–48 (2018).

19. Zhao, Z., Uddi, M., Tsvetkov, N., Yildiz, B. & Ghoniem, A. F. Redox Kinetics and Nonstoichiometry of Ce 0.5 Zr 0.5 O 2−δ for Water Splitting and Hydrogen Production. *The Journal of Physical Chemistry C* **121**, 11055–11068 (2017).

20. Welte, M., Warren, K., Scheffe, J. R. & Steinfeld, A. Combined Ceria Reduction and Methane Reforming in a Solar-Driven Particle-Transport Reactor. *Ind Eng Chem Res* **56**, 10300–10308 (2017).

21. Chuayboon, S., Abanades, S. & Rodat, S. High-Purity and Clean Syngas and Hydrogen Production From Two-Step CH4 Reforming and H2O Splitting Through Isothermal Ceria Redox Cycle Using Concentrated Sunlight. *Front Energy Res* **8**, 1–14 (2020).

22. Chuayboon, S., Abanades, S. & Rodat, S. Solar chemical looping reforming of methane combined with isothermal H2O/CO2 splitting using ceria oxygen carrier for syngas production. *Journal of Energy Chemistry* **41**, 60–72 (2020).

23. Haribal, V. P. *et al.* Modified Ceria for "Low-Temperature" CO 2 Utilization: A Chemical Looping Route to Exploit Industrial Waste Heat. *Adv Energy Mater* **9**, 1901963 (2019).

24. Ruan, C. *et al.* Synergy of the catalytic activation on Ni and the CeO 2 -TiO 2 /Ce 2 Ti 2 O 7 stoichiometric redox cycle for dramatically enhanced solar fuel production. *Energy Environ Sci* **12**, 767–779 (2019).

25. Bork, A. H., Carrillo, A. J., Hood, Z. D., Yildiz, B. & Rupp, J. L. M. Oxygen Exchange in Dual-Phase La 0.65 Sr 0.35 MnO 3 –CeO 2 Composites for Solar Thermochemical Fuel Production. *ACS Appl Mater Interfaces* **12**, 32622–32632 (2020).

26. Haeussler, A. & Abanades, S. Additive manufacturing and two-step redox cycling of ordered porous ceria structures for solar-driven thermochemical fuel production. *Chem Eng Sci* **246**, 116999 (2021).

27. Hoes, M., Ackermann, S., Theiler, D., Furler, P. & Steinfeld, A. Additive-Manufactured Ordered Porous Structures Made of Ceria for Concentrating Solar Applications. *Energy Technology* **7**, (2019).

28. Ruan, C. *et al.* Synergy of the catalytic activation on Ni and the CeO 2 –TiO 2 /Ce 2 Ti 2 O 7 stoichiometric redox cycle for dramatically enhanced solar fuel production. *Energy Environ Sci* **12**, 767–779 (2019).

29. Jiang, Q. *et al.* Mixed conductive composites for 'Low-Temperature' thermo-chemical CO 2 splitting and syngas generation. *J Mater Chem A Mater* **8**, 13173–13182 (2020).

30. Carrillo, A. J., Navarrete, L., Laqdiem, M., Balaguer, M. & Serra, J. M. Boosting methane partial oxidation on ceria through exsolution of robust Ru nanoparticles. *Mater Adv* **2**, 2924–2934 (2021).

31. Warren, K. J., Carrillo, R. J., Greek, B., Hill, C. M. & Scheffe, J. R. Solar Reactor Demonstration of Efficient and Selective Syngas Production via Chemical-Looping Dry Reforming of Methane over Ceria. *Energy Technology* **8**, 2000053 (2020).

32. Warren, K. J. & Scheffe, J. R. Role of Surface Oxygen Vacancy Concentration on the Dissociation of Methane over Nonstoichiometric Ceria. *The Journal of Physical Chemistry C* **123**, 13208–13218 (2019).

33. Sediva, E., Carrillo, A. J., Halloran, C. E. & Rupp, J. L. M. Evaluating the Redox Behavior of Doped Ceria for Thermochemical CO 2 Splitting Using Time-Resolved Raman Spectroscopy. *ACS Appl Energy Mater* **4**, 1474–1483 (2021).

34. Schmitt, R. *et al.* A review of defect structure and chemistry in ceria and its solid solutions. *Chemical Society Reviews* vol. 49 554–592 Preprint at https://doi.org/10.1039/c9cs00588a (2020).

35. Balaguer, M., Solís, C. & Serra, J. M. Study of the transport properties of the mixed ionic electronic conductor Ce1-xTbxO2-δ + Co (x = 0.1, 0.2) and evaluation as oxygen-transport membrane. *Chemistry of Materials* **23**, 2333–2343 (2011).

36. Balaguer, M., Solís, C., Roitsch, S. & Serra, J. M. Engineering microstructure and redox properties in the mixed conductor Ce0.9Pr0.1O2-δ + Co 2 mol%. *Dalton Transactions* **43**, 4305–4312 (2014).

37. Balaguer, M., Solís, C. & Serra, J. M. Structural-transport properties relationships on Ce 1- xLn xO 2-δ system (Ln = Gd, La, Tb, Pr, Eu, Er, Yb, Nd) and effect of cobalt addition. *Journal of Physical Chemistry C* **116**, 7975–7982 (2012).

38. Lobera, M. P., Balaguer, M., Garcia-Fayos, J. & Serra, J. M. Rare Earth-doped Ceria Catalysts for ODHE Reaction in a Catalytic Modified MIEC Membrane Reactor. *ChemCatChem* **4**, 2102–2111 (2012).

39. Sediva, E., Carrillo, A. J., Halloran, C. E. & Rupp, J. L. M. Evaluating the Redox Behavior of Doped Ceria for Thermochemical CO $_2$ Splitting Using Time-Resolved Raman Spectroscopy. *ACS Appl Energy Mater* **4**, 1474–1483 (2021).

40. le Gal, A. & Abanades, S. Dopant incorporation in ceria for enhanced water-splitting activity during solar thermochemical hydrogen generation. *Journal of Physical Chemistry C* **116**, 13516–13523 (2012).

41. Čebašek, N., Haugsrud, R. & Norby, T. Determination of inter-diffusion coefficients for the A- and B-site in the A2BO4 + δ (A = La, Nd and B = Ni, Cu) system. *Solid State Ion* **231**, 74–80 (2013).

42. Hong, S. J. & Virkar, A. v. Lattice Parameters and Densities of Rare-Earth Oxide Doped Ceria Electrolytes. *Journal of the American Ceramic Society* **78**, 433–439 (1995).

43. Warren, K. J. & Scheffe, J. R. Role of Surface Oxygen Vacancy Concentration on the Dissociation of Methane over Nonstoichiometric Ceria. *Journal of Physical Chemistry C* **123**, 13208–13218 (2019).

44. Otsuka, K., Wang, Y., Sunada, E. & Yamanaka, I. *Direct Partial Oxidation of Methane to Synthesis Gas by Cerium Oxide*. *JOURNAL OF CATALYSIS* vol. 175 (1998).

45. Omar, S., Wachsman, E. D., Jones, J. L. & Nino, J. C. Crystal structure-ionic conductivity relationships in doped ceria systems. *Journal of the American Ceramic Society* **92**, 2674–2681 (2009).

46. Rao, G. R. & Mishra, B. G. *Structural, redox and catalytic chemistry of ceria based materials*. (2003).

47. Faber, J., Geoffroy, C., Roux, A., Sylvestre, A. & Ab~lard, P. *Applied s A Systematic Investigation of the dc Electrical Conductivity of Rare-Earth Doped Ceria*. *Appl. Phys. A* vol. 49 (1989).

48. Mogensen, M., Sammes, N. M. & Tompsett, G. A. Physical, chemical and electrochemical properties of pure and doped ceria. *Solid State Ion* **129**, 63–94 (2000).

49. Andersson, D. A., Simak, S. I., Skorodumova, N. v, Abrikosov, I. A. & Rje Johansson, B. *Optimization of ionic conductivity in doped ceria*. vol. 103 (2006).

50. Gao, X. *et al.* Efficient ceria nanostructures for enhanced solar fuel production via high-temperature thermochemical redox cycles. *J Mater Chem A Mater* **4**, 9614–9624 (2016).

51. Venstrom, L. J., Petkovich, N., Rudisill, S., Stein, A. & Davidson, J. H. The effects of morphology on the oxidation of ceria by water and carbon dioxide. *Journal of Solar Energy Engineering, Transactions of the ASME* **134**, (2012).

52. Tianshu, Z. Ionic conductivity in the CeO2–Gd2O3 system (0.05≤Gd/Ce≤0.4) prepared by oxalate coprecipitation. *Solid State Ion* **148**, 567–573 (2002).

7.

CONCLUSIONS AND REMARKS

7. Conclusions and remarks

The present thesis focused on studying different approaches to improve the J_{O_2} rates for traditional OTMs and dual-phase membranes stables in CO_2. In addition, the revalorization of CO_2 was studied via chemical looping with lanthanide doped ceria as catalyst. Here are the different conclusions extracted from this Thesis:

Spinel-fluorite in dual-phase membranes

- EIS studies on dual-phase catalytic layers showed a decrease in R_p as the amount of ionic phase in the catalytic layer increases. 20NFO80CTO had 10 times less R_p compared with 80NFO20CTO, obtaining 0.117 $\Omega\cdot cm^2$ and 1.162 $\Omega\cdot cm^2$, respectively.
- In all NFO/CTO-based catalytic layers (excepting 20NFO80CTO), an important contribution appears at HF (103-104 Hz), related to the poor conductivity of the NFO (0.26 $S\cdot cm^{-1}$ at 800 ºC).
- The results obtained in EIS studies correlated with the J_{O_2} obtained for different ratios on the dual-phase catalytic layer in 50NFO50CTO membranes. Here, the membrane with 20NFO80CTO achieves the highest J_{O_2} (0.202 $mL\cdot min^{-1}\cdot cm^{-2}$) and 80NFO20CTO the lowest (0.082 $mL\cdot min^{-1}\cdot cm^{-2}$), with closer values to those obtained when operating without catalytic layer (0.060 $mL\cdot min^{-1}\cdot cm^{-2}$).
- The lowest activation energy in J_{O_2} was obtained for the same composition as the membrane (50NFO50CTO), but the second lowest value corresponded to 20NFO80CTO, 0.78 and 0.84 eV, respectively.
- Substituting NFO for Co_2MnO_4 as an electronic phase in NFO/CTO dual-phase material, the total conductivity was increased more than 10 times,

achieving 0.77 S·cm^{-1} for CMO/CTO and 0.07 S·cm^{-1} for NFO/CTO in air at 800 ºC.

- The increase of the total conductivity for the dual-phase membrane (CMO/CTO) leads to higher oxygen-permeation flux values concerning NFO/CTO membranes with the same dual-phase ratio, 0.22 mL·min^{-1}·cm^{-2} and 0.11 mL·min^{-1}·cm^{-2} at 850 ºC under air/Ar, respectively.
- CMO/CTO was studied under CO_2 atmospheres, achieving the highest J_{O_2} under 100% of CO_2. 0.24 mL·min^{-1}·cm^{-2}. Even so, the membrane was poisoned under 250 ppm SO_2/30%CO_2/70%Ar, decreasing the J_{O_2} until 0.11 mL·min^{-1}·cm^{-2} after 24 h.
- EIS studies on the CMO/CTO catalytic layer showed low interaction with the CO_2 in the R_p at high temperatures (850 ºC), but this interaction increases at lower temperatures.
- Under 10%CH_4/90% Ar, the CMO/CTO membrane achieved high oxygen permeation (1.11 mL·min^{-1}·cm^{-2} at 850 ºC). Even so, a part of the exposed catalytic layer was degraded, which was observed in post-mortem characterization by SEM analysis.

Electrification of BSCF membranes

- $Ba_{0.5}Sr_{0.5}Co_{0.8}Fe_{0.2}O_{3-\delta}$-based oxygen-transport membrane enabled the in-situ heating via the Joule effect. A temperature of 900 ºC on the membrane in a reactor at 650 ºC was achieved by applying 33 W. The increase in the membrane temperature was associated with the corresponding rise in the J_{O_2}.
- The electrified BSCF-coated membrane showed lower J_{O_2} than the non-electrified membrane. This effect is correlated with the loss of the catalytic layer. For this membrane, it was performed a 100 h stability test applying

33W, achieving around 906 ºC membrane temperature and 3.8 mL·min^{-1}·cm^{-2} J_{O_2}.

- CTO-coated membrane showed higher oxygen permeation than BSCF-coated membrane, but a lower membrane temperature was achieved (850 ºC). This effect was related to the catalytic layer's sintering, observed in post-mortem characterization by cross-section SEM images.
- The electrified and non-electrified membrane reactors were studied for ODHE reaction. Here, the electrified membranes showed higher catalytic performance for the ethylene yield than non-electrified membranes. For the BSCF-coated membrane, the C_2H_4 yield increases from 10% (for non-electrified mode) to 40% (for the electrified mode).

$Ce_{0.9}Ln_{0.1}O_{2-\delta}$ a catalyst in chemical looping

- A series of 10% lanthanide-doped ceria (Ce, La, Nd, Gd, Y, Er) materials were synthesized, with the cell parameter variation in accordance with the dopant’s ionic radius.
- During the POM reaction the highest H_2 production is obtained at 900 ºC for CeNd91, with 16.6 NmL·g^{-1}, related with the material with highest ionic conductivity, CeNd91.
- The oxy-combustion was more present for the CeLn91 catalyst than the pure ceria. It was related to the availability of surface-adsorbed oxygen species on the oxide material, higher for CeLn91 than for the pure ceria.
- For the CO_2 splitting reaction, the different CeLn91 (Ln= Ce, La, Nd, Gd, Y, Er) showed a volcano-like shape between the CO peak rate and the lanthanide ionic radius. Interestingly, the same trend was previously observed in literature for the influence of lanthanide dopants in the total conductivity of these materials. Here, a linear relationship was obtained

between the CO_2 splitting kinetics and the total conductivity on $Ce_{0.9}Ln_{0.1}O_{2-\delta}$ materials.

- Gd-doped ceria was found to be at the top of the volcano plot for both CO_2 splitting rate and total conductivity, ascribed to a lower activation energy for the creation of oxygen vacancies that, in turn, are the active sites for adsorption of oxygen reaction intermediates.

The main objectives of this Thesis were to understand and learn about different developing technologies to be considered for a greener and more sustainable future. To secure that future, the reduction of GHG emissions, as well as technologies for the capture and utilisation of CO_2, are fundamental. In this matter, one of the developing technologies to improve CO_2 capture will be the oxy-combustion processes, where the production of pure oxygen is essential. Here, different technologies have been developed in the past decades. For that reason, these studies mainly focused on producing pure oxygen via OTMs, developing dual-phase materials or adding different routes to improve the traditional OTMs. In addition, chemical looping methane reforming was studied for the revalorization of CO_2 streams.

Also, in this thesis, several techniques used in different technologies have been applied and linked to improve the understanding of the other studies. The first example is the case of the EIS technique, which is used to characterize the performance of the electrodes in SOFC or SOEC technologies. Here, it was used to characterize the behavior of the catalytic layers in dual-phase materials. With this technique, it was possible to understand and study the better ratio of the NFO/CTO dual-phase for catalytic layers. Also, it was used to see the interaction with the CO_2 in the CMO/CTO study.

For the traditional BSCF capillary membranes, electric current was used in OTMs, increasing the membrane temperature with the consequent increase in the J_{O_2}. This behaviour was also studied in ODHE reaction, showing a relevant improvement. However, the electrified membranes showed issues with the catalytic layer regarding sinterization or delamination.

Finally, the correlation of studies of total conductivity in doped ceria (commonly used as ionic material in several technologies) with chemical looping reactors as catalysts was achieved. Here, a direct correlation between the total conductivity and the reaction kinetics on the CO_2 splitting was observed. These results have enabled the correlation of redox catalysts with materials investigated in the *Solid State Ionics* community.

8.

FIGURE AND TABLE LIST

8. Figure and table list

8.1. Figures

8.2. Tables

See you Space cowboy!

Cowboy Bebop (1998)